REPORT DOCUMENTATION PAGE

Form Approved
OMB No. 0704-0188

1. AGENCY USE ONLY (Leave blank)	2. REPORT DATE	3. REPORT TYPE AND DATES COVERED
	6/15/96	Final Technical 2/93 - 1/96

4. TITLE AND SUBTITLE

Hydrogen Tolerance of γ - TiAl Microstructures

5. FUNDING NUMBERS

F49620-93-1-0140

6. AUTHOR(S)

Tresa M. Pollock and Anthony W. Thompson

AFOSR-TR-96
0385

7. PERFORMING ORGANIZATION NAME(S) AND ADDRESS(ES)

Carnegie Mellon
5000 Forbes Avenue
Pittsburgh, PA 15213

9. SPONSORING/MONITORING AGENCY NAME(S) AND ADDRESS(ES)

AFOSR/[redacted]
110 Duncan Avenue
Suite B115
Bolling AFB, DC 20332-0001

NA

10. SPONSORING/MONITORING AGENCY REPORT NUMBER

93-1-0140

11. SUPPLEMENTARY NOTES

12a. DISTRIBUTION/AVAILABILITY STATEMENT

Approved for public release;
Distribution unlimited

12b. DISTRIBUTION CODE

19960726 039

13. ABSTRACT *(Maximum 200 words)*

The influence of hydrogen on the microstructure and mechanical properties of gamma titanium aluminide alloys has been studied. Gas phase charging experiments have been conducted over the temperature range of 500°C to 1100°C with hydrogen pressures from 0.1 to 13.8 MPa. Following high pressure charging, two different hydrides have been observed: a newly identified tetragonal hydride and a FCC δ hydride. The new hydride, designated the θ phase, has a composition of approximately Ti_2AlH and is body centered tetragonal with lattice parameters of a = 0.528nm and c = 2.848nm. At lower hydrogen pressures of 0.1MPa, both hydride phases have been observed only in near-surface regions in association with a series of reactions with trace gaseous impurities that result in complex mixtures of oxides and hydrides. Tension tests were conducted on samples that were pre-exposed to air, vacuum and 0.1 MPa hydrogen environments prior to testing. Yield strengths were not significantly influenced by the hydrogen, air or vacuum exposures, but tensile ductility was reduced by both air and hydrogen exposures. Compression experiments following high pressure charging showed a substantial strengthening effect of the hydrides. No tension experiments could be conducted on high pressure charged materials, due to the extreme embrittling effect of these high pressure exposures.

14. SUBJECT TERMS

15. NUMBER OF PAGES 111

16. PRICE CODE

17. SECURITY CLASSIFICATION OF REPORT	18. SECURITY CLASSIFICATION OF THIS PAGE	19. SECURITY CLASSIFICATION OF ABSTRACT	20. LIMITATION OF ABSTRACT
Unclassified	Unclassified	Unclassified	UL

DISCLAIMER NOTICE

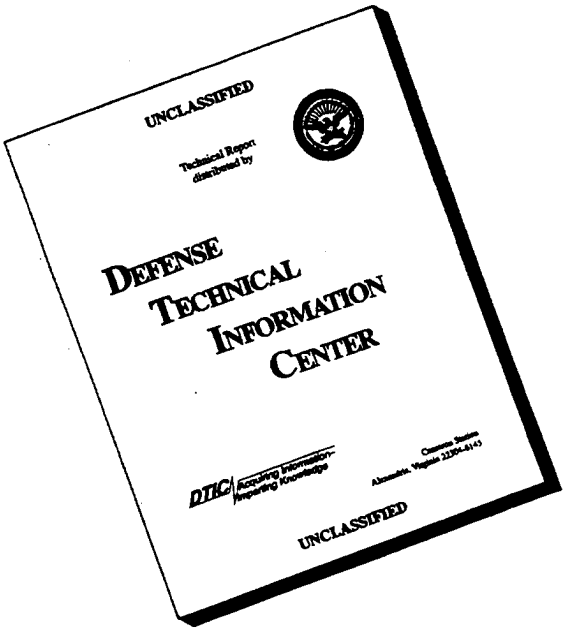

THIS DOCUMENT IS BEST QUALITY AVAILABLE. THE COPY FURNISHED TO DTIC CONTAINED A SIGNIFICANT NUMBER OF PAGES WHICH DO NOT REPRODUCE LEGIBLY.

GENERAL INSTRUCTIONS FOR COMPLETING SF 298

The Report Documentation Page (RDP) is used in announcing and cataloging reports. It is important that this information be consistent with the rest of the report, particularly the cover and title page. Instructions for filling in each block of the form follow. It is important to ***stay within the lines*** to meet ***optical scanning requirements.***

Block 1. Agency Use Only *(Leave blank)*.

Block 2. Report Date. Full publication date including day, month, and year, if available (e.g. 1 Jan 88). Must cite at least the year.

Block 3. Type of Report and Dates Covered. State whether report is interim, final, etc. If applicable, enter inclusive report dates (e.g. 10 Jun 87 - 30 Jun 88).

Block 4. Title and Subtitle. A title is taken from the part of the report that provides the most meaningful and complete information. When a report is prepared in more than one volume, repeat the primary title, add volume number, and include subtitle for the specific volume. On classified documents enter the title classification in parentheses.

Block 5. Funding Numbers. To include contract and grant numbers; may include program element number(s), project number(s), task number(s), and work unit number(s). Use the following labels:

C	- Contract	PR	- Project
G	- Grant	TA	- Task
PE	- Program Element	WU	- Work Unit Accession No.

Block 6. Author(s). Name(s) of person(s) responsible for writing the report, performing the research, or credited with the content of the report. If editor or compiler, this should follow the name(s).

Block 7. Performing Organization Name(s) and Address(es). Self-explanatory.

Block 8. Performing Organization Report Number. Enter the unique alphanumeric report number(s) assigned by the organization performing the report.

Block 9. Sponsoring/Monitoring Agency Name(s) and Address(es). Self-explanatory.

Block 10. Sponsoring/Monitoring Agency Report Number. *(If known)*

Block 11. Supplementary Notes. Enter information not included elsewhere such as: Prepared in cooperation with...; Trans. of...; To be published in.... When a report is revised, include a statement whether the new report supersedes or supplements the older report.

Block 12a. Distribution/Availability Statement. Denotes public availability or limitations. Cite any availability to the public. Enter additional limitations or special markings in all capitals (e.g. NOFORN, REL, ITAR).

DOD	- See DoDD 5230.24, "Distribution Statements on Technical Documents."
DOE	- See authorities.
NASA	- See Handbook NHB 2200.2.
NTIS	- Leave blank.

Block 12b. Distribution Code.

DOD	- Leave blank.
DOE	- Enter DOE distribution categories from the Standard Distribution for Unclassified Scientific and Technical Reports.
NASA	- Leave blank.
NTIS	- Leave blank.

Block 13. Abstract. Include a brief *(Maximum 200 words)* factual summary of the most significant information contained in the report.

Block 14. Subject Terms. Keywords or phrases identifying major subjects in the report.

Block 15. Number of Pages. Enter the total number of pages.

Block 16. Price Code. Enter appropriate price code *(NTIS only)*.

Blocks 17. - 19. Security Classifications. Self-explanatory. Enter U.S. Security Classification in accordance with U.S. Security Regulations (i.e., UNCLASSIFIED). If form contains classified information, stamp classification on the top and bottom of the page.

Block 20. Limitation of Abstract. This block must be completed to assign a limitation to the abstract. Enter either UL (unlimited) or SAR (same as report). An entry in this block is necessary if the abstract is to be limited. If blank, the abstract is assumed to be unlimited.

Table of Contents

1.0 Objectives and Approach

Gamma titanium alumindes have recently received a great deal of attention due to the potential for application in military and commercial aircraft engines. However, one concern that persists with this class of materials is their sensitivity to environmental embrittlement. This research has specifically focused on hydrogen embrittlement of gamma titanium alumindes with the ultimate objective of identifying mechanisms of degradation and microstructures that are resistant to degradation in hydrogen containing environments. Accordingly, the first year of this program focused on defining the range of conditions under which hydrogen charging occurs in a number of alloys, including Ti-48Al-2Cr-2Nb alloy in cast + HIP and isothermally forged forms, and vacuum arc melted Ti-52Al. In the second and third years we studied in detail hydrogen-induced changes in microstructure and the resultant mechanical properties of hydrogen-charged materials.

2.0 Summary of Results

Gas phase charging experiments have been conducted over the temperature range of 500°C to 1100°C with hydrogen pressures from 0.1 to 13.8 MPa. Following high pressure charging, two different hydrides have been observed: a newly identified tetragonal hydride and a FCC δ hydride. The new hydride, designated the θ phase, has a composition of approximately Ti_2AlH and is body centered tetragonal with lattice parameters of a = 0.528nm and c = 2.848nm. This hydride forms primarily at the expense of the α_2 phase, with an orientation relationship between the θ phase and α_2 or γ phases of $(0001)\alpha_2//(111)\gamma//(001)_\theta$, $[11\bar{2}\,0]\alpha_2//[1\bar{1}\,0]\gamma//[100]_\theta$. The δ phase is isomorphous with the hydride formed in pure titanium, with a lattice parameter of 0.445nm. Following charging at hydrogen gas pressures of 7 MPa and 13.8 MPa, both hydride phases have

been observed throughout all materials examined, with the exception of fully lamellar 48-2-2 alloy, where only cubic hydrides have been observed.

In materials charged at a lower pressure of 0.1MPa, both hydride phases have been observed only in near-surface regions in association with a series of reactions with trace gaseous impurities that result in complex mixtures of oxides and hydrides. In the absence of these impurities, all hydrogen remains in solution following charging at 0.1 MPa and no hydrides were observed in any of the compositions examined.

Tension tests were conducted on samples that were pre-exposed to 0.1 MPa (1 atm) hydrogen at 500°C for 72 hrs and on samples that were exposed to air and vacuum, respectively, at 500°C for 72 hrs. The average hydrogen uptake for these pre-charging experiments was 315 wppm, and under these conditions all hydrogen remains in solution. Yield strengths were not significantly influenced by the hydrogen or air exposures at 500°C. However, both the hydrogen and air exposures reduced tensile ductility. Compression experiments on samples subjected to higher pressure hydrogen charging show that the hydrides produce substantial strengthening with only a minor effect on strain rate sensitivity and work hardening rates at room temperature. Although no tension experiments could be conducted on high pressure charged material, the brittleness of post-charged foils suggests that these hydrides have a very detrimental effect on properties.

3.0 Description of Research

Specific details regarding the research program are given in the following sections. Experimental materials and procedures are first outlined, microstructural and mechanical observations are given and this is followed by a discussion of the findings.

3.1 Experimental Materials and Procedures

The bulk of the research to be described here was aimed at one gamma titanium aluminide alloy, Ti-48Al-2Cr-2Nb. Cast slabs, cast and hipped bars and isothermally forged pancakes of Ti-48Al-2Cr-2Nb (subsequently referred to as "48-2-2" for convenience) were obtained from General Electric Aircraft Engines. The Al levels in the cast and forged materials were matched in order to permit direct property comparisons between these two forms of material. The composition, including interstitials, of the cast and wrought materials, respectively, is given in Table I.

To assess the possible effects of chemical composition, a limited number of experiments were also been conducted on three binary alloys, Ti-52Al, Ti-50Al and Ti-49Al, as well as some powders of the 48-2-2 alloy. The Ti-52Al material was produced by vacuum arc melting at DMRL, Hyderabad, India, while the Ti-49Al was cast + extruded by McDonnell Douglas.

The response of two different 48-2-2 microstructures to hydrogen exposure has been investigated. The first is a duplex microstructure established through casting and/or wrought processing and a subsequent heat treatment of 1280°C/3hrs (air cool) + 900°C/4hrs. The second is a fully lamellar microstructure produced by a heat treatment of 1400°C/3hrs (air cool) + 900°C/4hrs. To investigate the behavior of a single phase alloy under the same charging conditions, samples of Ti-52Al were also subjected to a heat treatment of 1280°C/3hrs (air cool) + 900°C/4hrs. The microstructures of the duplex isothermally forged and cast materials are shown in Figures 1(a) and 1(b). The microstructures of the fully lamellar 48-2-2 and the Ti-52Al are shown in Figures 1(c) and 1(d), respectively. The forged 48-2-2 material had a microstructure consisting of equiaxed γ grains and γ - α_2 grains of very finely spaced lamellae, along with some blocky α_2 along

grain boundaries. Due to the evolution of grain structure during solidification, the cast 48-2-2 material exhibited considerable inhomogeneity with regard to lamellae orientation throughout the cast slab. The Ti-52Al material was composed of single phase gamma grains (with grain sizes in the range of 100μm - 300μm) with occasional particles of Al_2O_3 dispersed throughout the structure.

Table I - Chemical Composition of Experimental Materials

Material	Ti (at%)	Al (at%)	Cr (at%)	Nb (at%)	H (wppm)	O (wppm)	N (wppm)
48-2-2 Cast	48.6	47.3	1.9	1.9	24	740	70
48-2-2 Forged	48.7	47.4	1.9	2.0	37	530	40
Ti-52Al	48.4	51.6					30
Ti-50Al	50.1	49.9			18		

For charging of all the experimental materials, blanks measuring approximately 15 x 15 x 2mm were mechanically polished, cleaned with methanol and subjected to gas phase charging. Several different gas-phase charging techniques have been utilized in this effort. A high pressure hydrogen gas atmosphere chamber in the IITRI/MRF hydrogen facility at the NASA-Marshall Space Flight Center was utilized to charge samples at pressures of 7 MPa and 13.8 MPa for 60 hrs at 800°C. Hydrogen containing less than 50 wppm impurities and less than 1 wppm oxygen was utilized. For charging at lower pressures and temperatures up to 900°C, a Sieverts apparatus was utilized. When charging with the Sieverts apparatus, samples were inserted and the charging chamber evacuated to 10^{-7} torr. Samples were subsequently heated in vacuum to the charging temperature with the vacuum pumping system isolated from the main chamber. Upon reaching a stable charging

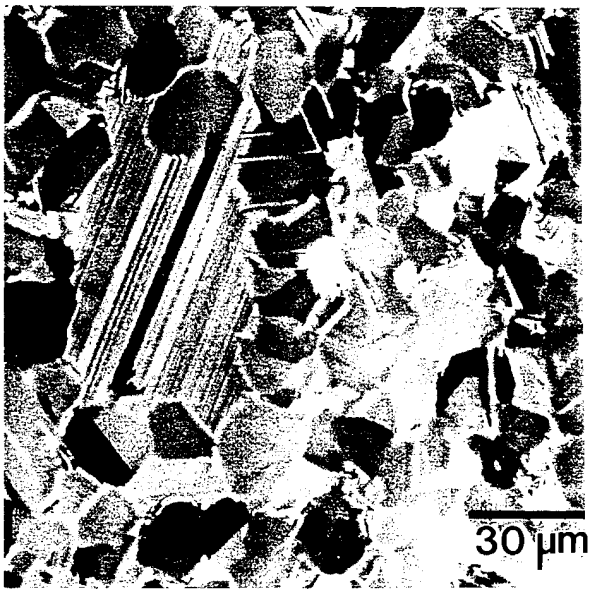

(a)

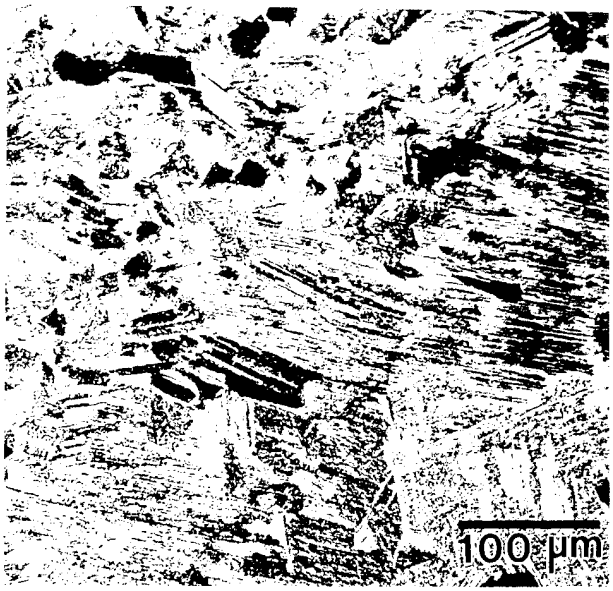

(b)

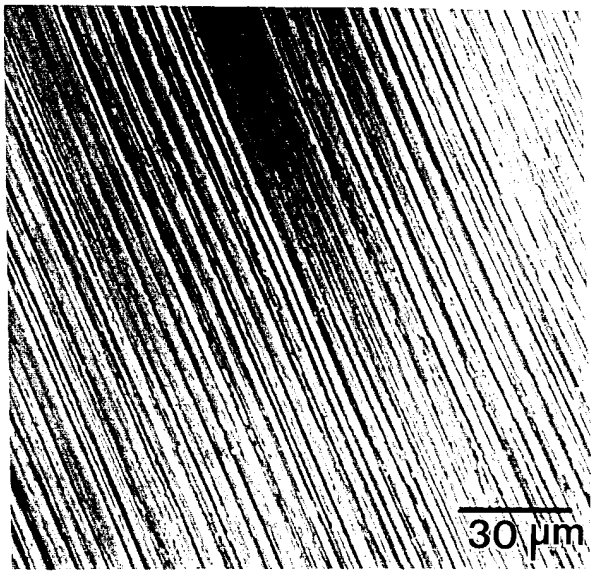

(c)

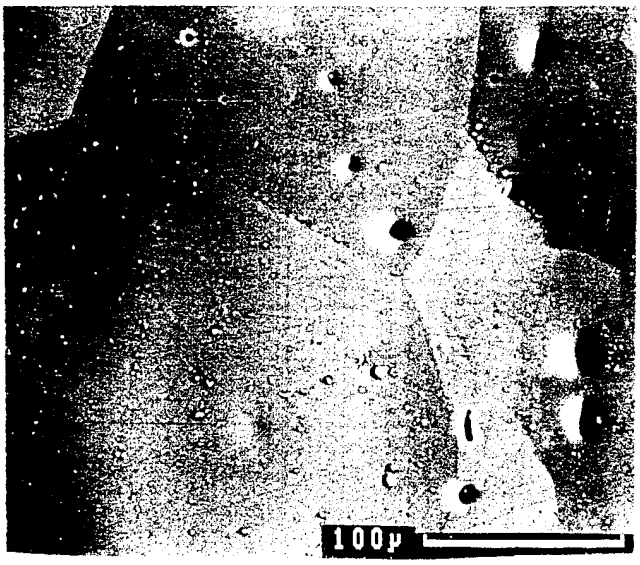

(d)

Figure 1 - Microstructures of precharged materials: Isothermally forged duplex Ti-48Al-2Cr-2Nb (a), cast duplex 48-2-2 (b), fully lamellar 48-2-2 (c) and Ti-52Al (d).

temperature, the main chamber was immediately backfilled with H_2. The hydrogen pressure at exposure temperature was 750 torr (0.1MPa). Pressure drops in the Sieverts apparatus were less than 10 torr over a time period of 24 hours, under conditions where no samples were loaded. After 24 hrs of exposure, the H_2 was removed and the system repeatedly flushed with Ar. Cooling down to room temperature with an Ar atmosphere required about 10 minutes. For charging at temperatures above 900°C, quartz tubes containing the specimens were evacuated to a pressure of 10^{-6} torr, backfilled with H_2 and sealed. The tubes were inserted in the furnace when it reached equilibrium at the desired charging temperature. After 24 hrs they were removed from the furnace and cooled down to room temperature in approximately 5 minutes.

Following charging, hydrogen uptake was measured by standard combustion analysis techniques. Weight gains by individual samples induced by the charging process were also monitored for all charging experiments with a high precision microbalance with a sensitivity of 10 micrograms. Degassing experiments in vacuum were conducted in temperature range of 900 to 1100°C for times of up to 72 hrs.

Hydrogen-charged samples were examined by light microscopy, X-ray diffraction (Cu-K_α radiation), scanning and transmission electron microscopy and Auger spectroscopy. TEM samples, 3 mm in diameter, were sectioned by electric discharge machining, ground to a thickness of 100 μm and dimpled. Subsequently, the hydrogen-exposed material was ion milled and the uncharged material was jet polished in a solution of 150 ml butanol, 30 ml perchloric acid and 350 ml methanol at 22 V and -55°C.

The influence of hydrogen on mechanical behavior was investigated in tension and compression using a screw-driven testing machine. Tension tests were conducted on cylindrical, threaded specimens with gage diameters of 4mm. Tests were conducted in air

with an initial strain rate of $2x10^{-4}$ s^{-1}. In selected compression experiments, strain rate changes between $2x10^{-4}$ s^{-1} and $2x10^{-2}$ s^{-1} were conducted. MoS_2 was used as a lubricant to minimize friction at the specimen/platen interface.

3.2 Material Response to Hydrogen Charging

The results of charging experiments conducted over the temperature range of 500°C to 1150°C are shown in Table II. For charging experiments conducted at lower pressures in the temperature range of 500°C to 1150°C, the highest hydrogen uptake occurred at the lowest temperature of 500°C. Also, following charging at a fixed temperature, the 48-2-2 alloys had a higher hydrogen content, compared to the higher Al binary alloys. The higher hydrogen content of the α_2 containing materials and lower hydrogen uptake at higher temperatures is indicative of the importance of the α_2 phase in the charging process; this will be discussed further in subsequent sections.

Parallel weight gain measurements that utilized the high precision microbalance (on a total of approximately 75 samples) showed a significant degree of variability in the response of these materials to low pressure hydrogen, particularly at higher temperatures. Additionally, in some instances weight gains for individual samples were greater than could be accounted for by hydrogen uptake (compared to analyses shown in Table II), while in other cases weight losses were observed. As will be apparent from subsequent discussions on the microstructure of hydrogen-charged materials, this is related to variations in surface and internal microstructure. A comparison of the present low pressure charging results with others reported in the literature for various TiAl-based compositions, Figure 2, also suggests a significant microstructure-induced variability.

Table II - Results of Hydrogen Charging Experiments on TiAl Alloys

Alloy	Microstructure	Charging Temp. (°C)	Charging Pressure (MPa)	Hydrogen Uptake# (wppm)
48-2-2	Cast Duplex	500	0.1	315
48-2-2	Cast Duplex	850	0.1	50
48-2-2	Cast Duplex	900	0.1	5
48-2-2	Cast Duplex	1100	0.1	40
48-2-2	Powder	500	0.1	300
Ti-49Al	Extruded	500	0.1	170
Ti-49Al	Extruded	850	0.1	15
Ti-49Al	Extruded	1100	0.1	39
48-2-2	Cast Duplex	800	7.0	1800
48-2-2*	Wrought Duplex	800	13.8	2000
48-2-2**	Wrought Duplex	800	13.8	3900
48-2-2*	Cast Duplex	800	13.8	2300
48-2-2**	Wrought Fully Lamellar	800	13.8	2270
Ti-52Al**	All γ	800	13.8	640

#measured by combustion analysis
* and ** indicate two independent high pressure charging experiments

At higher hydrogen gas pressures, the hydrogen uptake increased substantially compared to the 0.1 MPa charging. Following charging at 13.8 MPa and 800°C the cast 48-2-2 material contained 2300 wppm (8 atomic%), compared to only 50 wppm at 0.1 MPa and 850°C. Under the same high pressure charging conditions, the single phase gamma Ti-52Al material was subject to a hydrogen uptake of only 640wppm, again due to the lower solubility of hydrogen in the γ phase, compared to the α_2 phase. As will be discussed

further in the following section, these high levels of hydrogen resulted in hydride formation, whereas hydrides were not generally observed following low pressure charging.

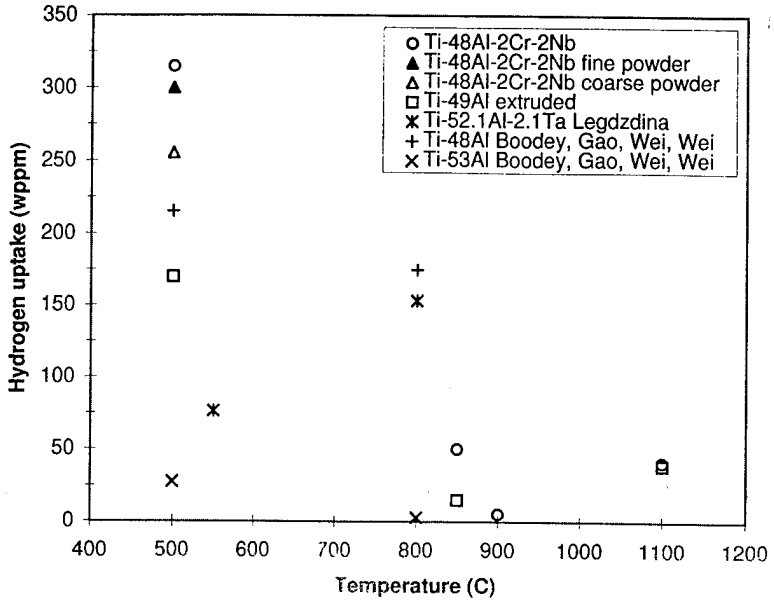

Figure 2 - Hydrogen uptake for a several different TiAl-based alloys.

3.3 Hydrogen-Induced Changes in Microstructure

The post-charged microstructures of the γ-based alloys examined varied substantially with composition, microstructure and charging pressure. In the following sections these hydrogen-induced changes in microstructure are described in detail, including the characterization of a new hydride phase, designated as the "θ" phase. Microstructural changes have been studied by optical, scanning and transmission electron microscopy, energy dispersive spectroscopy, Auger electron spectroscopy, and X-ray analysis. Table III briefly summarizes the results of these detailed examinations for specific initial microstructures and compositions along with the charging conditions and the section of this report where these observations are documented in detail.

Table III - Summary of Hydrogen-induced Microstructure Changes

Alloy and Initial Microstructure	H Charging Conditions	Microstructural Observations	Section
Cast, Wrought 48-2-2, Ti-49Al, Ti-52Al	500°C to 1100°C + 0.1MPa	No hydrides observed	3.3.1
Wrought Duplex 48-2-2	740 °C + 0.1 MPa	No hydrides, except in the near surface regions, where θ and FCC hydrides were observed.	3.3.5
Duplex 48-2-2, cast and wrought	800 °C +13.8 MPa (1st charging)	θ hydride.	3.3.1
Duplex wrought	800 °C +13.8 MPa (2nd charging)	θ and FCC hydrides.	3.3.1
Wrought, Lamellar 48-2-2	800 °C + 13.8 MPa	FCC hydrides were observed in α_2 and γ laths, with a higher volume fraction than charged at 7 MPa.	3.3.2
Wrought, Lamellar 48-2-2	800 °C + 7.0 MPa	FCC hydrides were observed in α_2 and γ laths.	3.3.2
Ti-52 Al	800 °C + 13.8 MPa	FCC plus occasional θ hydrides were observed.	3.3.3

3.3.1 Duplex Ti-48Al-2Cr-2Nb

The pre-charged duplex microstructures of cast and wrought 48-2-2, as shown in Figure 1, consisted of a mixture of equiaxed γ and lamellar γ - α_2 grains, along with some grain boundary α_2. No significant changes in these microstructures were observed following low pressure charging at 0.1 MPa over the temperature range from 500 to 1100 °C. Under these charging conditions, the hydrogen content of the material increased by a maximum of

315 wppm. Post-charged materials examined by X-rays and scanning and transmission electron revealed only the α_2 and γ phases with no significant changes in their distribution. However, as will be discussed in further sections, the 315 wppm level of hydrogen did adversely affect tensile ductility. Also, hydrides were observed in near-surface regions under some conditions; the details of these observations are given in Section 3.3.4.

Substantial changes in microstructure were observed under higher pressure charging conditions. Gas phase charging at 800°C and a pressure of 13.8 MPa resulted in hydrogen uptakes of 2000 wppm and 2300 wppm for the wrought and cast materials, respectively, in the first charging experiment. The second exposure of the wrought material (only) to a hydrogen pressure of 13.8 MPa at 800 °C resulted in a hydrogen uptake of 3900 wppm, as compared to 2000 wppm in the first high pressure charging experiment. There were also parallel differences in the microstructures of the post-charged materials in the first charging, as compared to the second charging run for the wrought material, as discussed further below.

Following charging and subsequent cooling to room temperature, the microstructures of all duplex materials were dramatically altered. The lamellar character of the microstructure was disturbed and a high density (approximately 25 vol%) of small, blocky precipitates were present throughout the microstructure. Figure 3 is a backscattered micrograph of the wrought material following the first high pressure charging experiment. The precipitates, with the brighter contrast, were preferentially located in former lamellar grains of the microstructure, but also within gamma grains. These precipitates were present throughout the entire cross section of 8mm x 8mm x 14mm charging samples, indicating hydrogen diffusion through the entire sample during charging. The precipitates, which to our knowledge have not been previously observed in other studies of hydrogen charging of

gamma titanium aluminides, are hydrides that will subsequently be referred to as the "θ" phase. The detailed characterization of this and other hydride phases observed follows.

Figure 3 - Duplex microstructure following charging at 800°C and 13.8MPa for 60 hrs.

The charged samples were extremely brittle following the 13.8 MPa charging treatment, and extreme care was required to produce and handle TEM foils. Eight and five foils were viewed for first and second charging experiments, respectively, for the wrought material. Two foils were successfully prepared from the cast material from the first charging run. No significant differences between the cast and wrought materials, both charged in the first high pressure experiment, were apparent.

TEM bright field images and diffraction patterns as well as X-ray analyses revealed the presence of a new ternary hydride (the "θ" phase) in all materials examined following the high pressure charging treatment, except for the fully lamellar 48-2-2. Figure 4 is a bright field image of the duplex wrought material following the first charging experiment. An

isolated precipitate of the new hydride is embedded in a γ grain with twins, where the twinning plane inclined to the image plane.

A considerable amount of the θ hydride phase as well as locally dense populations of a FCC hydride phase (more details on this hydride are also given below) were also observed in the material following the second high pressure charging experiment. Figure 5 shows a region where FCC hydrides are predominately present along with a few θ hydride grains located in the grain boundaries. TEM BF images also revealed extensive amounts of the FCC hydride phase in the equiaxed γ phase region as well as lamellar regions, Figure 6 and 7. Considering the higher hydrogen uptake associated with the second set of charging experiments, it appears that the FCC hydrides are associated with the higher hydrogen uptake. More detailed analysis of local compositional fluctuations (discussed in later sections) suggest that the original microstructural inhomogeneity of the forged material may be the source of some of the differences in the response to hydrogen in the first versus the second charging experiment.

3.3.1.1 Characterization of the θ Hydride

TEM observations of the charged 48-2-2 material at relatively low magnification, Figures 8 and 9, showed the new θ phase to be preferentially present in the prior α_2 regions of the microstructure including grain boundary α_2 and lamellar regions. In these figures, the darker, blocky precipitates are the new hydride phase. Some traces of the original lamellar structure are apparent, Figure 9. Interestingly, these blocky precipitates did not always extend across the entire diameter of the original α_2 lamellae. No evidence of the α_2 phase was found after charging based on X-ray and SAD patterns. The newly formed phases also had no consistent morphology. Some exhibited an elongated morphology which is probably derived from initial lamellar structure, Figure 10. In other regions, Figure 4, isolated precipitates of the new phase were embedded in the γ phase, apparent from the

Figure 4 Isolated precipitate of the new hydride is embedded in the γ-grain with twins.

Figure 5 TEM bright field image showing densely populated FCC hydrides and few tetragonal hydride grains are present at duplex 48-2-2 following charging at 13.8MPa and 800°C.

Figure 6 Low magnification bright field image showing densely populated hydride present in the equiaxed γ grains of duplex 48-2-2 charged at 13.8MPa.

Figure 7 Low magnification bright field image showing densely populated hydride present in the lamellar grains of duplex 48-2-2 charged at 13.8MPa.

surrounding twinned regions. Conversely, Figure 11 shows three hydride grains that are clustered together. In Figure 8 small blocky hydride grains are present along γ grain boundaries and their shapes and locations resemble the morphology of grain boundary α_2 present prior to being charged. The large misfit of the hydride presumably results in large internal stresses. Cracks were visible mostly along hydride grain boundaries in the TEM foils, indicated by arrow, Figure 10.

SAD patterns confirmed that the equiaxed γ phase maintains the same $L1_0$ structure of the γ phase as in the uncharged state, but with a slight increase in lattice parameters. Thick walls of dislocations were always observed along grain boundaries between the θ phase and γ grains; these dislocations presumably serve to accommodate a large volume misfit of the new phase, Figure 10. Additionally, the γ phase after charging possesses a very high density of dislocations and broad twins, Figure 4. It is difficult to establish whether they were induced by hydrogen charging; TEM BF image examination showed that after the 1280 °C heat treatment there existed abundant transformation or annealing twins in γ regions.

A higher magnification bright field view of one precipitate is shown in Figure 12. Accompanying this are a few selected area diffraction (SAD) patterns, Figure 13. In Figure 12 lattice fringes can be clearly seen in the entire grain under incident beam directions [hk0], indicating that the new phase has a large unit cell in one dimension, parallel to the fringe plane normal, through the entire grain. Obviously the hydride has a large density of planar faults which are not distributed uniformly. Additionally, it is interesting to note that the fringes were always parallel to the straight interface between the γ and the new hydride, where the two phases might be coherent or semi-coherent, Figure 10 and 14. The distribution and density of planar faults varied significantly from grain to grain. Some grains also revealed the presence of considerable amount of faults inclined to the image

plane, Figures 12 and 14. Fault loops, indicated by capital letter L, and edge-on faults on different planes, indicated by arrow, can be clearly seen in Figure 15.

To identify the lattice structure and unit cell parameters, an extensive characterization effort, which included analysis of SAD patterns and corresponding BF images as well as identification of fault planes, was conducted. Bright field micrographs and corresponding SAD patterns, Figure 12 and 13(a)-(c), were taken from the same region of an individual hydride grain under several zone orientations. The crystallographic angles among the zone axes were determined using Wulff-net stereo projections based on the experimental record of X and Y tilts. The angles were then compared to the those calculated from the unit cell model proposed. The initial five SAD patterns were labeled as A, B, C, D and E and are shown in the diagram of Figure 16. Studying the characteristics of the SAD patterns it was found that B, C and E are identical to that in Figure 13(b), and A, C correspond to (a) and (c), respectively. Inspection of the patterns from A to E confirmed that all zone axes chosen lie along a common Kikuchi band, with a consistent d-spacing as indicated in the patterns, (a)-(c). The angle between B and E is 90 degrees. The zone axes of B and C are located 26 and 27 degrees on each side of A. Thus, it can be deduced that the tilting axis is a four-fold symmetry axis. Also the zone A should have a two fold symmetry. Thus, a tetragonal unit cell with lattice parameters of a = 5.28 Å, c = 28.48 Å has been proposed. The five zone axes were indexed as shown in Figure 16. SADP analyses were further verified by comparing the measured angles with tabulated values based on the above unit cell; the accuracy was found to be within +/- 2 degrees.

The SAD patterns in Figure 13 (a)-(d) + (f) correspond to the [100], [120], [110], [001] and [551] zones of the new phase, respectively. The first more intense spot along the densely populated row of spots that are parallel to c* marked by an "x" in the diffraction pattern, corresponds to a d-spacing 4.74 Å, Figure 13(a)-(c). Note the presence of extra,

weaker reflections in the (hk0) patterns located at 1/3 and 2/3 distances between the transmitted spot and spot with d-spacing 4.74 Å. The allowed reflections are of the type k + L = 2n, indicating side-centered symmetry. However, for a tetragonal lattice there are only two possible Bravais lattices: primitive and body centered. Hence, the new phase has been identified as body centered tetragonal with lattice parameters a = 5.28 Å, c = 28.48 Å. Figure 13(d) was obtained from a hydride grain with different orientation with respect to one in Figure 13(a)-(c). The SAD pattern [001], exhibits four-fold symmetry; an identical lattice parameter of a = 5.28 Å was also calculated from this, which is consistent with the results obtained from [hk0] directions. [111], [031] and [131] patterns were also obtained from other hydride grains, Figure 13(e), (g) and (h), respectively. The calculated angles among the zone axes agree well with the above proposed unit cell. Finally, to prove the consistency of the results achieved under [hk0] and [001], a [001] SAD pattern was constructed from the observed [hk0] patterns based on the fact that [001] and [hk0] share the common planes (1/h, 1/k, 0). The main spots of the constructed [001] pattern agree well with the actual [001] pattern. This supports the original assumption of lattice type and parameters except that (110) types superlattice spots were missing which existed in the observed [001] pattern.

X-ray analyses revealed, Figure 17(a), that after the 1280 °C heat treatment the duplex microstructure contained γ and α_2 phases. In the charged spectrum, Figure 17(b), only peaks corresponding to the γ phase and the new hydride phase were observed. The location of the major peaks in the X-ray spectrum for the hydride phase are given in Table IV. It is clear that the proposed lattice accounts well for the majority of X-ray peaks of the hydride phase.

Figure 15 reveals that the hydride imaged under [120] beam direction contains a number of faults. Besides the existence of planar faults parallel to (002) planes, dense faults located

on planes inclined to the image plane are present. Examining the images, Figures 12 through 15 and Figure 18, lattice fringes are clearly visible, with a constant spacing of 14 Å. The tilting experiments demonstrated that their constant spacing does not change as long as the incident beam direction is [hk0], Figure 13(a)-(c). This leads to the deduction that the tilting axis, which is perpendicular to the direction of the lattice fringes, should be the [002] direction. This is verified by streaks through (002) spot perpendicular to the fringe direction taking into account the rotations in the SADs and images relative to the microscope calibration. The d_{006}- spacing is 4.74 Å, which coincides with the d_{0001}-spacing of α_2 phase of 4.67 Å.

Disturbances in lattice fringes are present due to non-periodic planar faults oriented parallel to the incident beam, with an (002) habit plane. The spacing between these planar faults varied from region to region within the hydride, but typically occurred with a spacing of 3 to 20 times that of lattices fringes, Figure 18. Additional faults with habit planes other than (002) were also observed, Figure 19.

Table IV - Identification of X-ray Peaks of Bulk Duplex 48-2-2 Charged at 13.8 MPa

2θ (°)	33.4	34.4	38.8	39.5	40.1	42.4	44.6	51.0	55.7	64.1	65.5	72.6	82.8	86.0
hkl	019	022	121	026	1,1, 10	125	127	232	132	2,2, 12	1,3,1 0	042	338	246
2θ* (°)	33.4	35	38.7	39.5	40.4	41.9	44.9	49.8	56.0	64.3	65.6	72.8	82.8	85.8

2θ and 2θ* indicate practical measurement and theoretical values.

When the operating zone axis is [100], the extra edge-on fault planes were indexed as (011), (0$\bar{1}$ 1), (0$\bar{1}$ 3), (013) and (010) with SAD patterns showing streaks parallel to (011) and (0$\bar{1}$ 1). The observed angles of (011) and (0$\bar{1}$ 1), (0$\bar{1}$ 3) and (013) planes, were approximately 21 and 60 degrees respectively, which are consistent with the values of calculated angles 21.0 and 58.2 degrees based on the proposed unit cell. The edge-on plane being perpendicular to (001) obviously is the (010) plane. Additionally, due to the tetragonality of the unit cell, the fault planes other than those mentioned above can also be (101), (103), (200) by permutation. This was verified by the [001] pattern with corresponding BF images showing perpendicular edge-on planes (200) and (020), Figure 20. The faults other than (002) faults were always observed as isolated faults which can be best revealed by bright field images taken with a 2-3 degree tilt away from [100] zone axis, Figure 21(a) and (b). In Figure 21(a) an elongated θ hydride particle of the duplex 48-2-2 charged at 13.8 MPa was viewed along a [100] direction showing edge-on faults with the following habit planes: (002), (011), (013) and (020). A two or three degree tilt with the incident beam parallel to (002) plane clearly demonstrated the features and the interactions of faults, Figure 21(b). Edge-on planar faults do not end inside the crystal, instead, faults on two different planes they are connected, indicated by "C". Additionally, the (013) type faults are associated with the regions with no lattice fringes present, Figure 19.

The BF images and corresponding zone axes [031], and [131] are shown in Figures 21 and 22. In Figure 21 streaks in the SAD patterns are perpendicular to the edge-on fault plane. Thus, the fault habit planes are identified as (026), (2$\bar{2}$ 6) and (200). The angles measured between (200) and (2$\bar{2}$ 6), (026) and (2$\bar{2}$ 6) are approximately 50 and 40 degrees, respectively, consistent with the angles 50.1 and 39.9 degrees calculated from the proposed unit cell. When the incident beam direction is [131], the edge-on fault planes, (02$\bar{6}$), ($\bar{2}$ 02) constitute a 95 degree angle which is again consistent with the angle 95.1° calculated from the unit cell, Figure 22. Figure 23 shows a bright field image of a θ hydride under

zone axis [111] with corresponding [111] SAD inset. The edge-on fault planes revealed an angle close to 90 degrees, which was identical to the angle measured from the $(01\bar{1})$ and $(10\bar{1})$ spots in the diffraction pattern and also consistent to the two planes angles calculated from the cell which is 88 degrees. In summary, the fault planes observed in the tetragonal hydrides are (002), (011), (013), $(0\bar{1}\ 1)$, $(0\bar{1}\ 3)$, (200) and $(2\bar{2}\ 6)$. The exact nature of these faults could not be determined due to inadequate knowledge of the atomic positions of atoms within the unit cell.

In summary, the θ hydride phase has a body centered tetragonal structure with a large "c" dimension unit cell. It is also a highly faulted structure with a number of characteristic fault planes. However, further characterization of the θ hydride by convergent beam electron diffraction (CBED) was not possible due to the high density of faults and thus at this time the atomic positions within the unit cell are still unknown. The possible space groups for this hydride are discussed further in Section 3.5. In addition to the new tetragonal hydrides, FCC hydrides were also observed in the duplex material charged at high pressures. The same hydrides were observed to be present in the Ti-52Al and the lamellar 48-2-2 and are described in more detail in the following sections.

3.3.1.2 Characterization of the δ Hydride

X-ray spectra and BSE images did not reveal noticeable microstructural differences in the duplex 48-2-2 following two separate charging experiments at 13.8 MPa and 800 °C. However, TEM BF images, Figure 24, revealed the presence of a second hydride with completely different morphology and lattice structure compared to the θ hydride, predominantly present in the 48-2-2 foils prepared from the second charging experiment.

Figure 8 Hydride phases surrounded by dense dislocations are present along γ grain boundaries.

Figur 9 Low magnification bright field image of hydrides plus γ grains. Darker, blocky precipitates are the new phase. Traces of the lamellar morphology are visible.

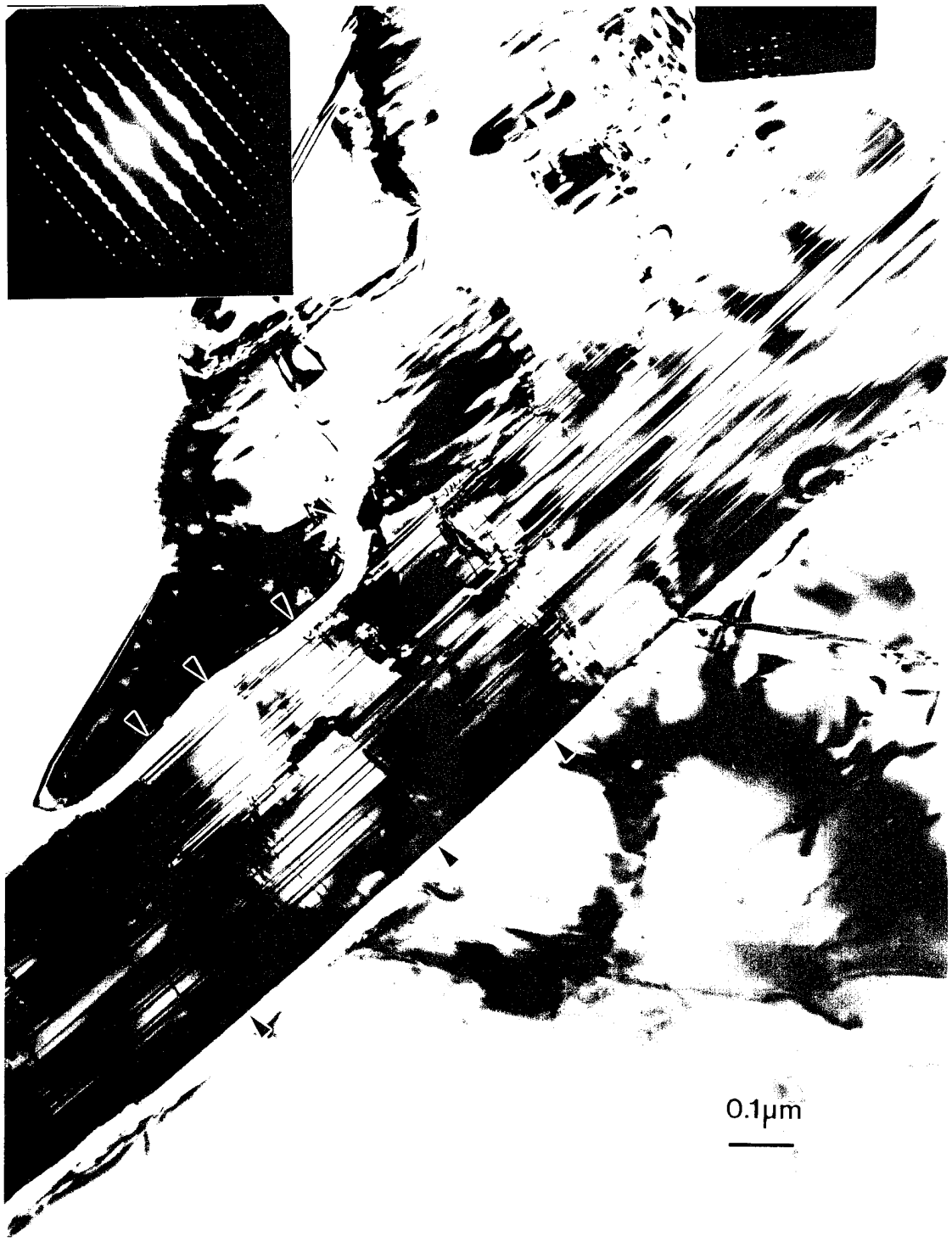

Figure 10 Cracks are always present in interfaces between γ and hydrides due to drastic lattice misfit upon precipitation (13.8 MPa charged duplex 48-2-2).

Figure 11 Bright field image showing a cluster of θ hydrides for duplex 48-2-2 charged at 13.8MPa with corresponding [100] zone diffraction pattern inset.

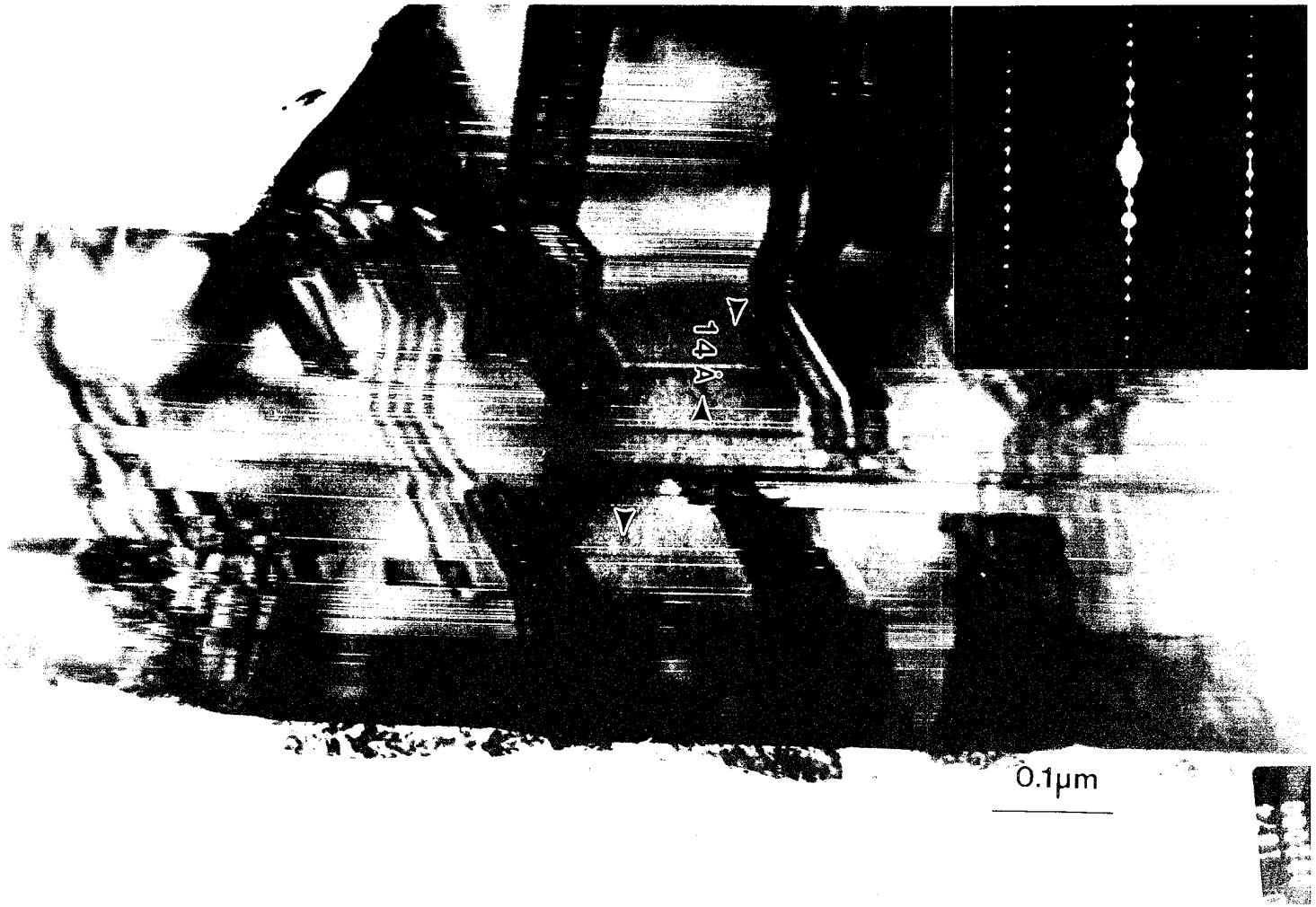

Figure 12 Bright field image of a θ hydride for duplex 48-2-2 charged at 13.8MPa with corresponding [120] zone diffraction pattern inset.

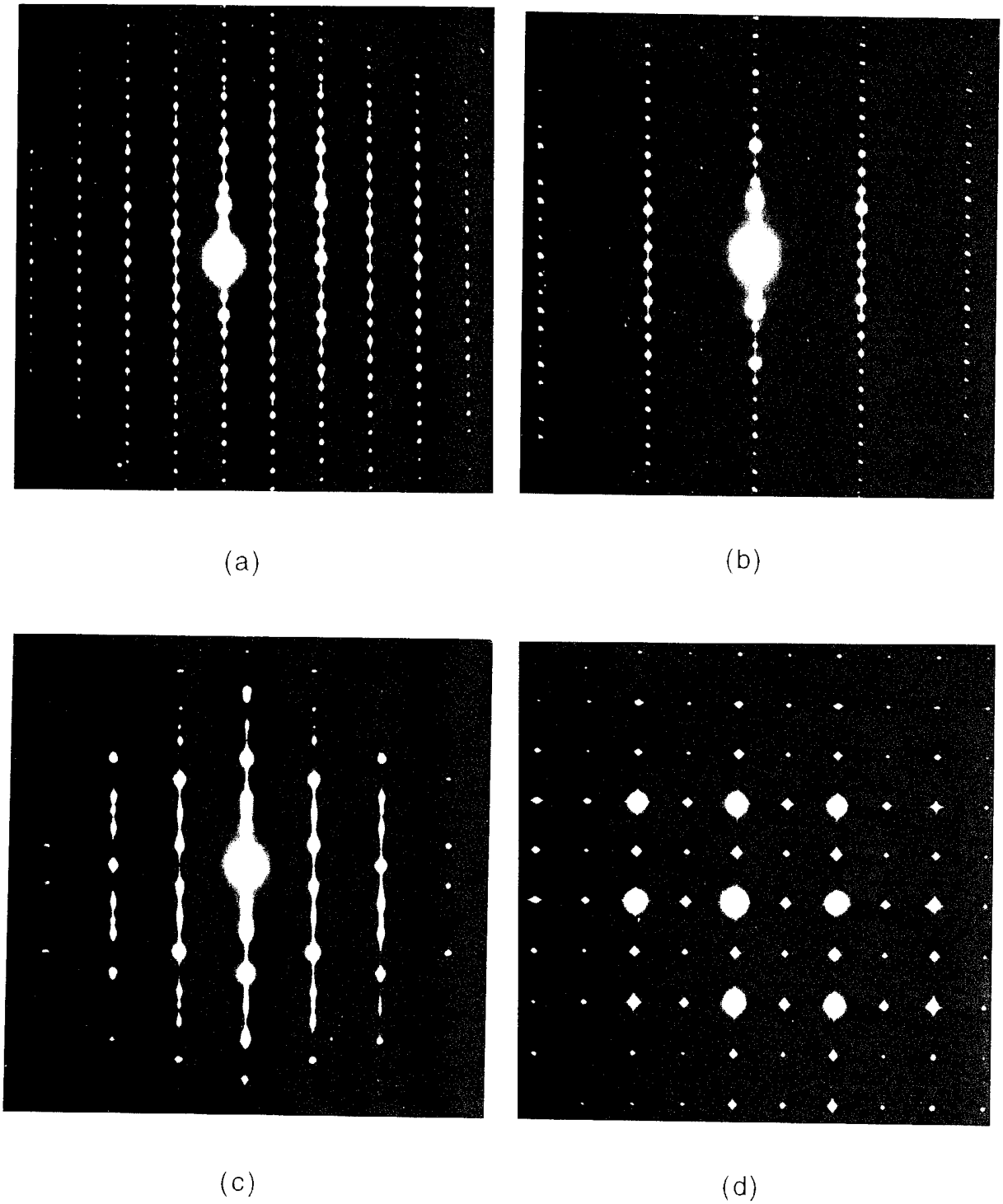

Figure 13 SAD patterns of tetragonal hydrides in 13.8 MPa charged duplex Ti-48-2-2 material [100], (a); [120], (b); [110], (c) and [001] (d).

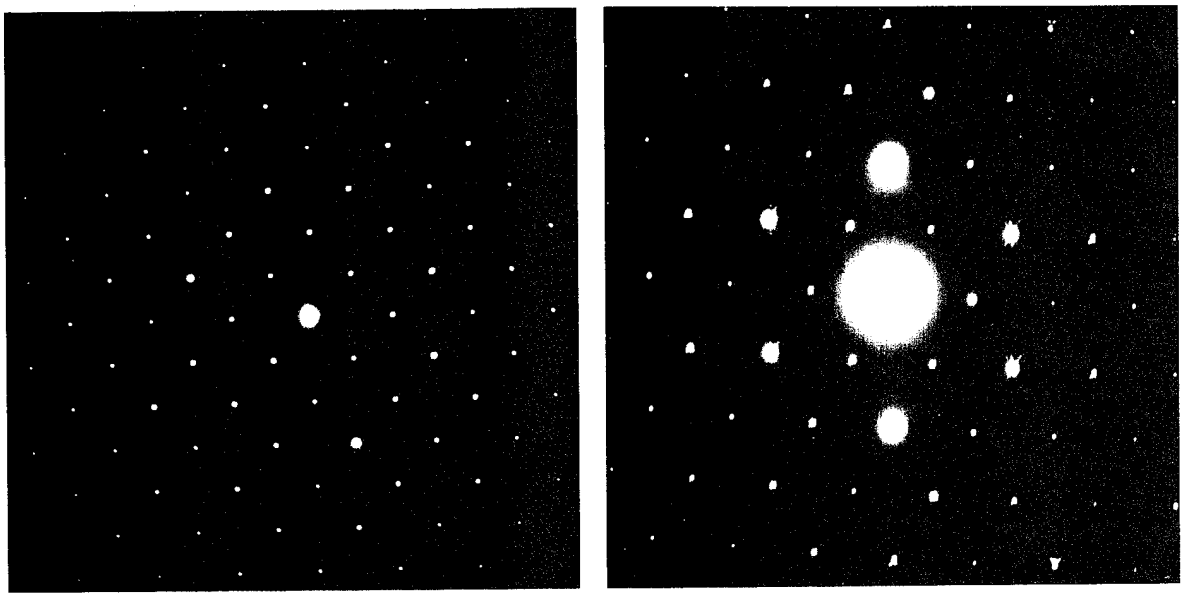

(e) (f)

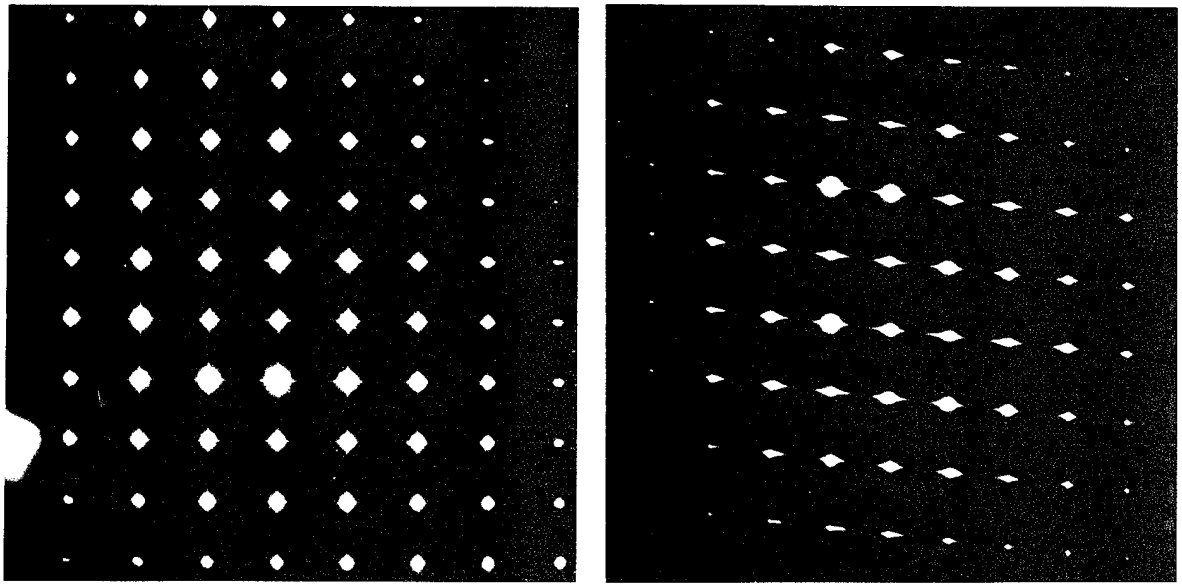

(g) (h)

Figure 13. SAD patterns of tetragonal hydrides in 13.8 MPa charged duplex Ti-48-2-2 material [111], (e); [551], (f); [031], (g) and [131] (h).

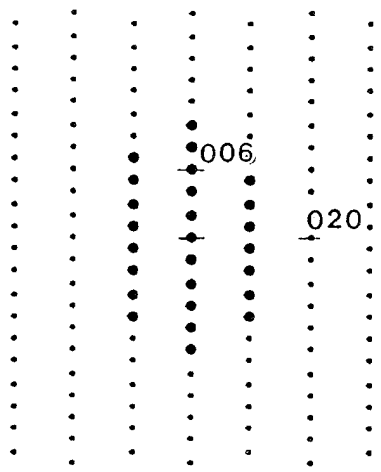

(a)

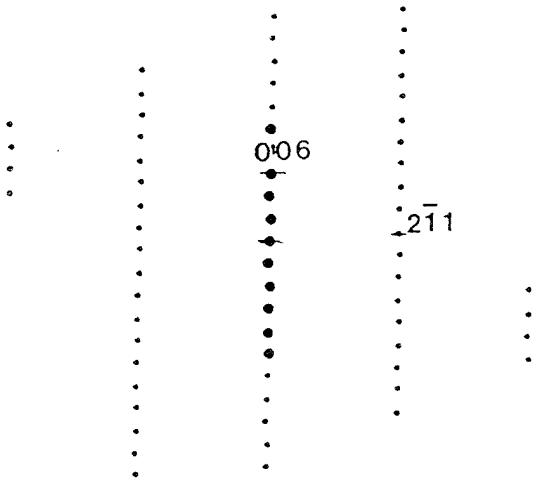

(b)

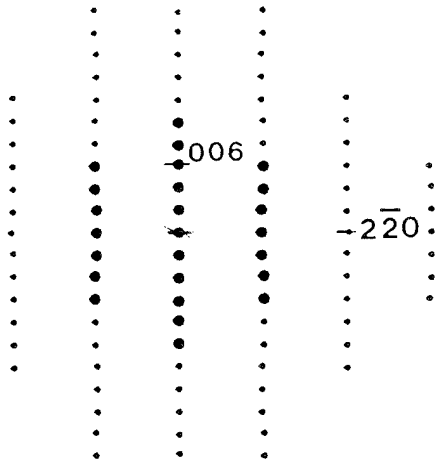

(c)

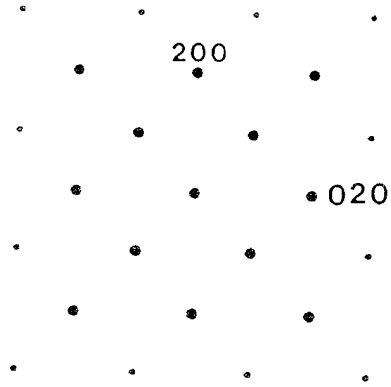

(d)

Indexed SAD patterns for Figure 13. [100], (a); [120], (b); [110], (c) and [001], [d].

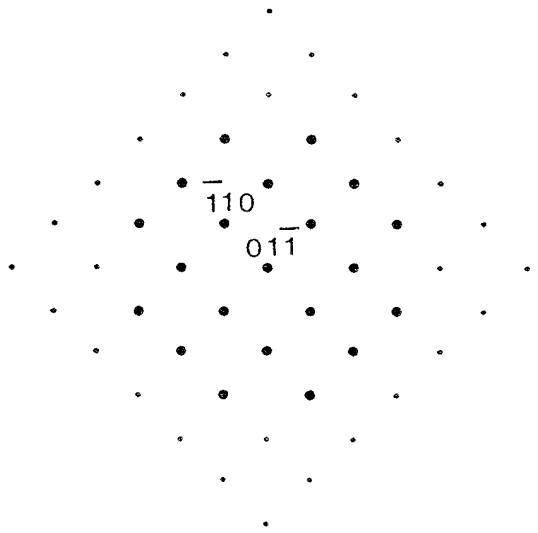

(e)

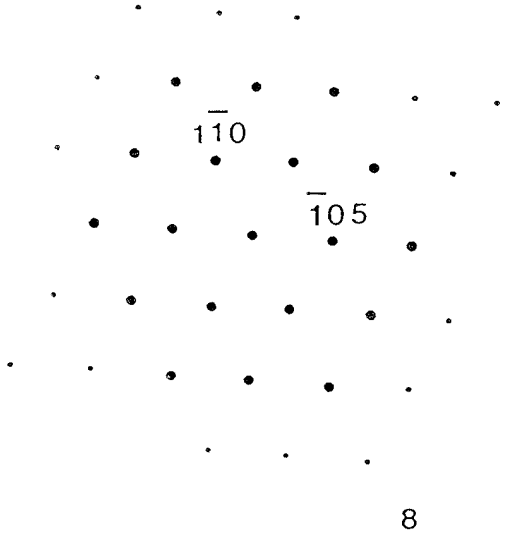

(f)

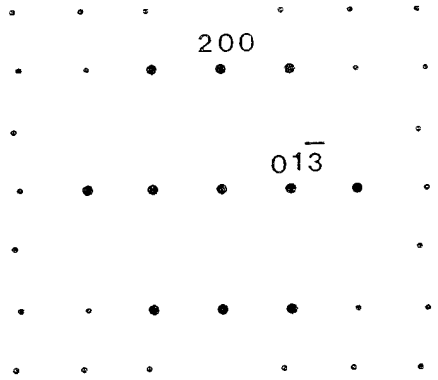

(g)

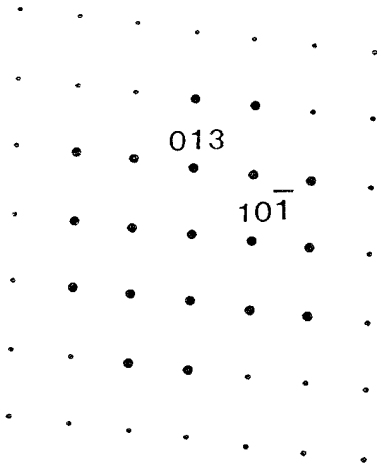

(h)

Indexed SAD patterns for Figure 13 [111], (e); [551], (f); [031], (g) and [$1\bar{3}1$], [h].

Figure 14 Bright field image of a hydride revealing lattice fringes parallel to its straight interface with γ matrix.

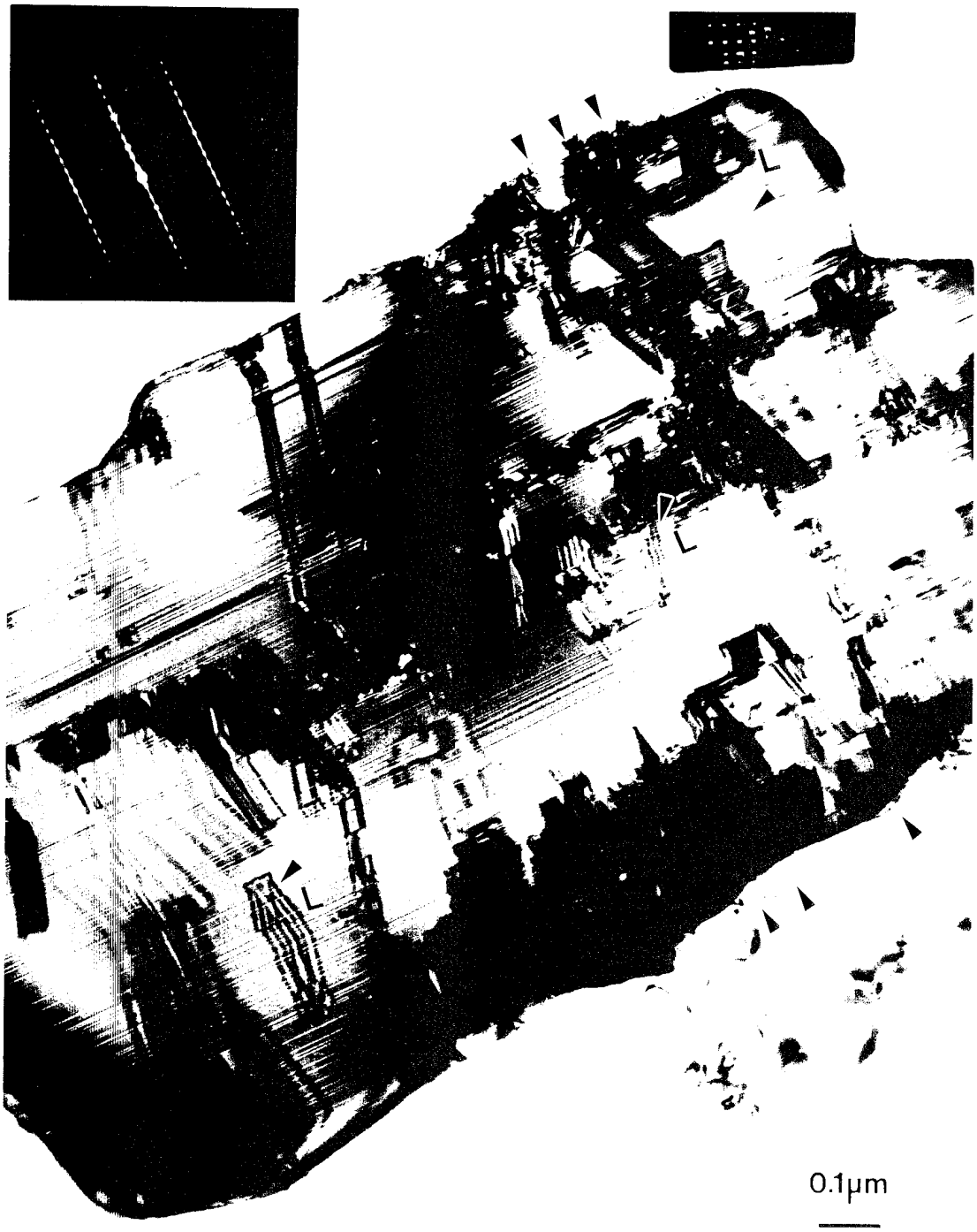

Figure 15 A hydride particle of duplex 48-2-2 charged at 13.8 MPa viewed along [120] direction, showing dense faults located in planes inclined to the image plane including fault loops and a thick wall of misfit dislocations.

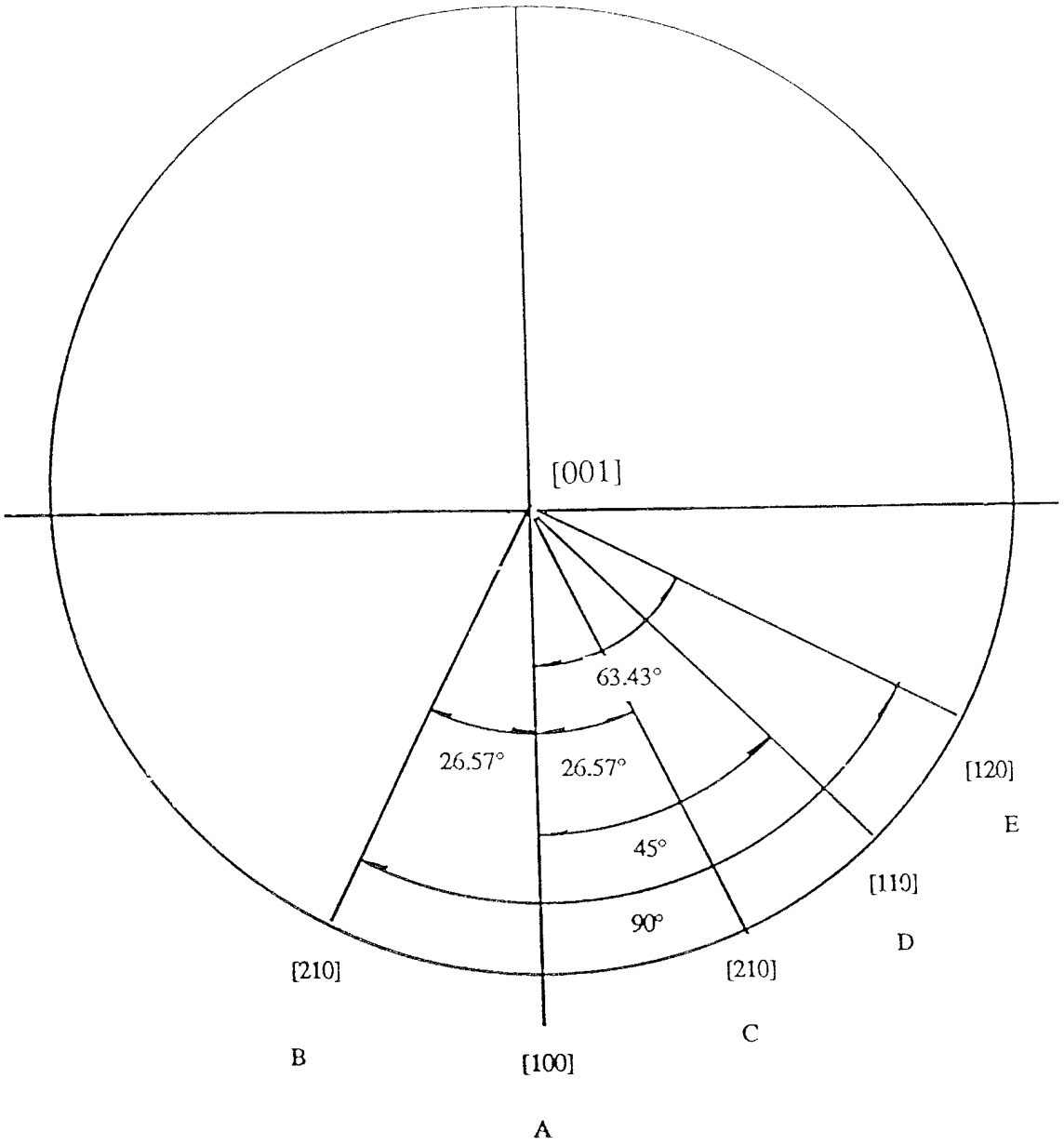

Angle mearsured:

AB: 27°
AC: 26°
CD: 18°
DE: 19°
AD: 44°

Figure 16 Schematic drawing of the [001] projection of the [hk0] zone axes.

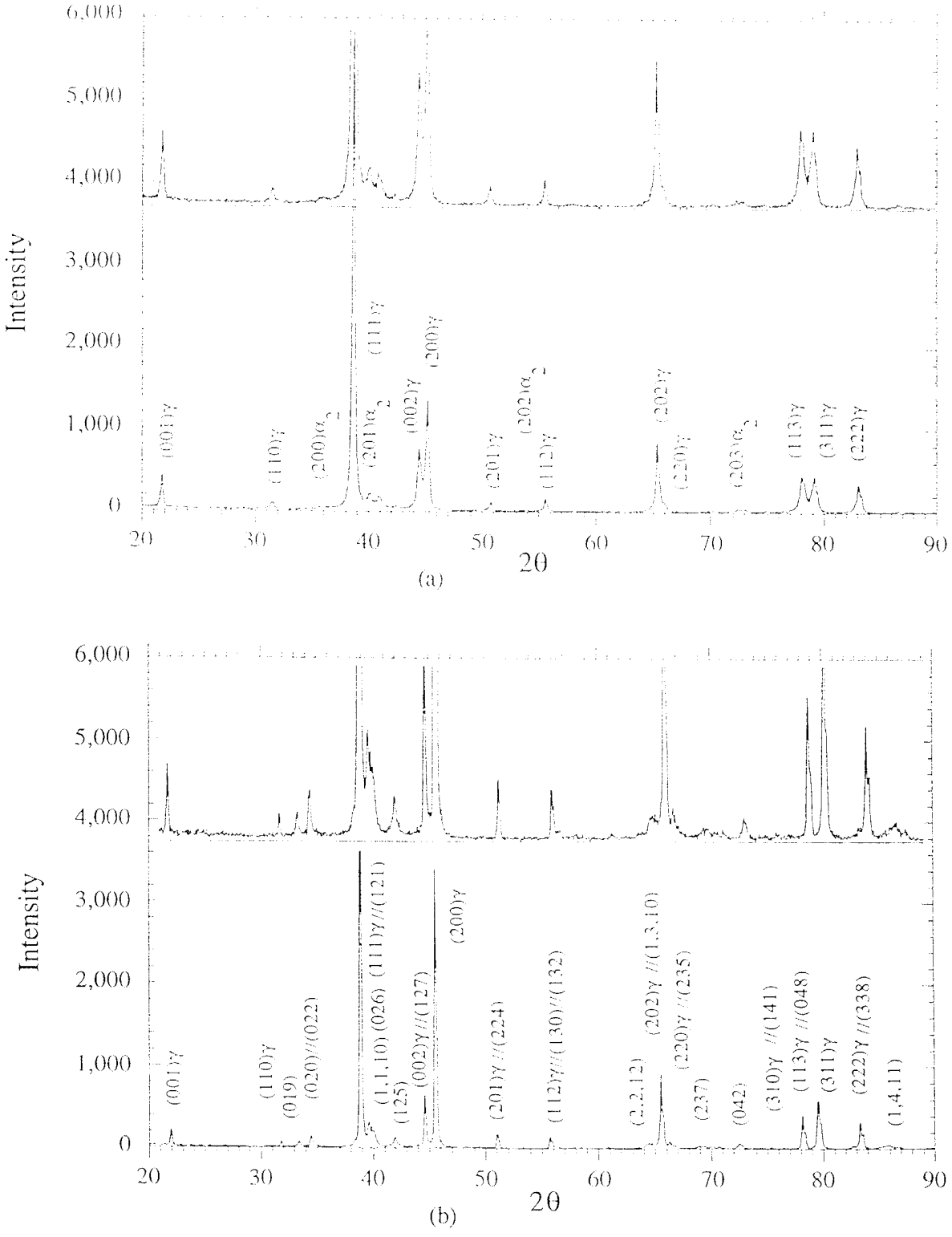

Figure 17 X-ray spectra of duplex 48-2-2 following heat treatment at 1280°C, (a) and charged at 13.8MPa from the bulk material, (b).

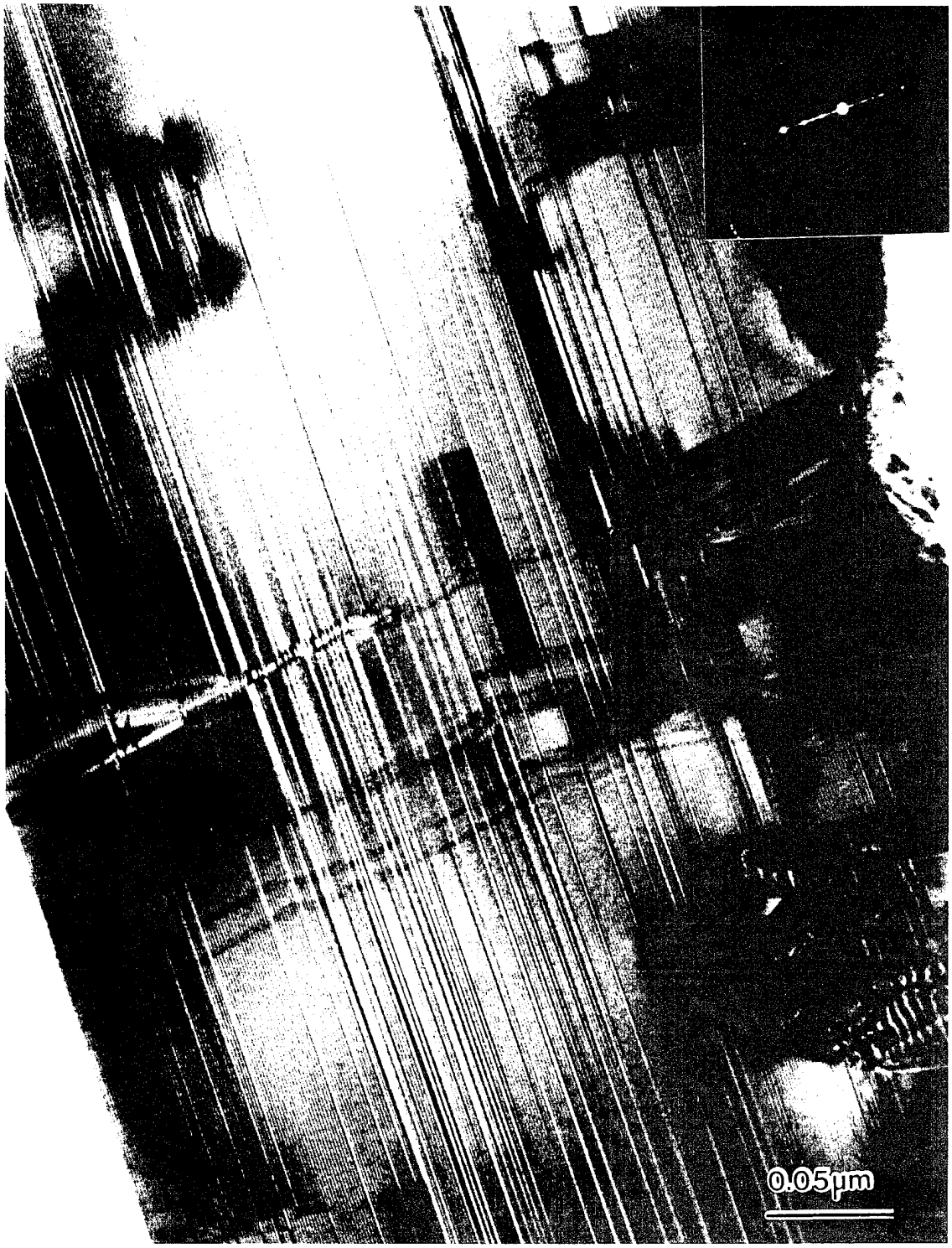

Figure 18 High magnification bright field image of a hydride showing lattice fringes with a constant spacing of 1.4nm parallel to (002) planes.

Figure 19 BF image and corresponding SAD pattern of a hydride revealing extra edge-on planes other than (002).

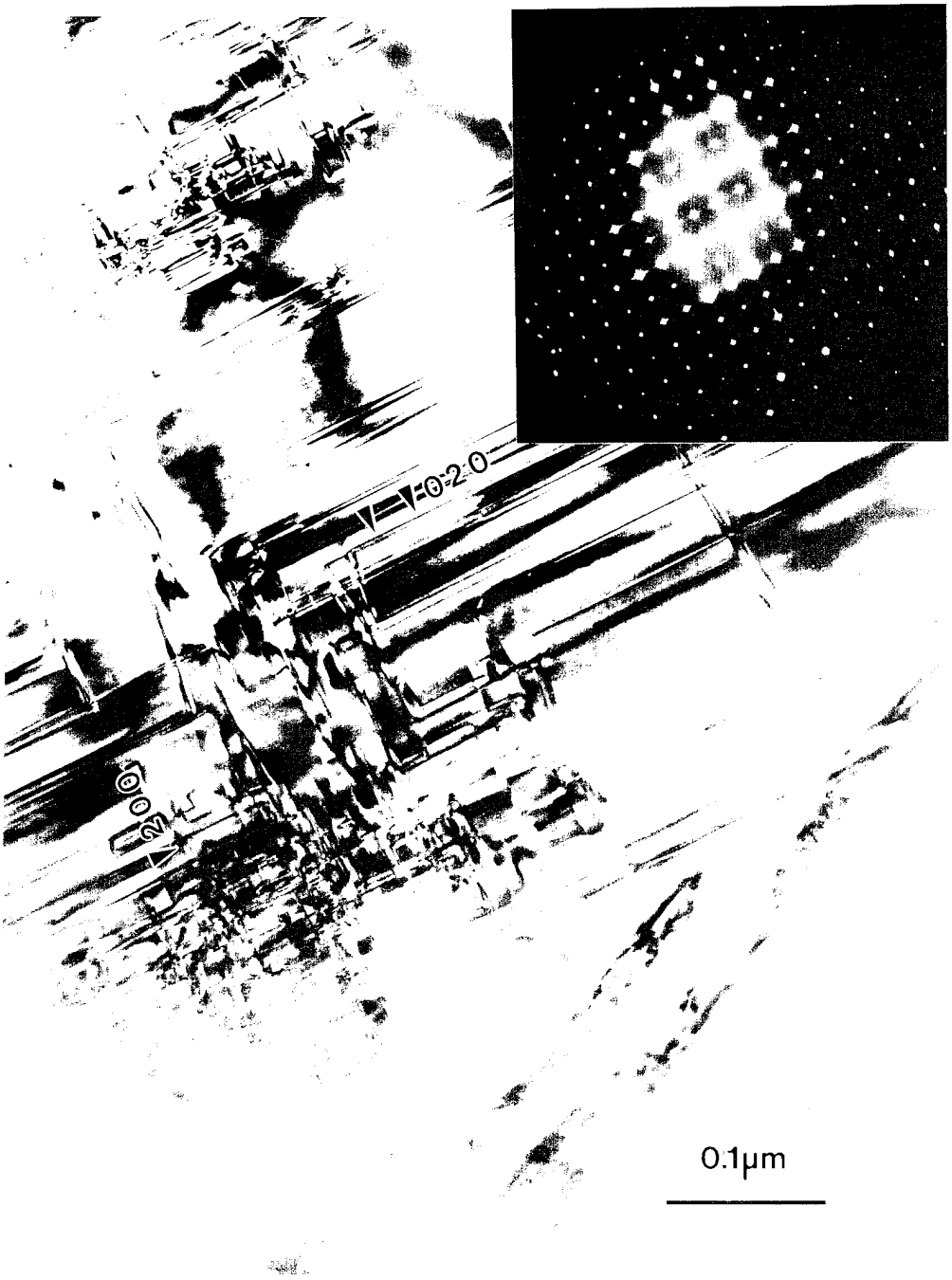

Figure 20 Bright field image of a θ hydride showing faults with corresponding [001] zone diffraction pattern inset.

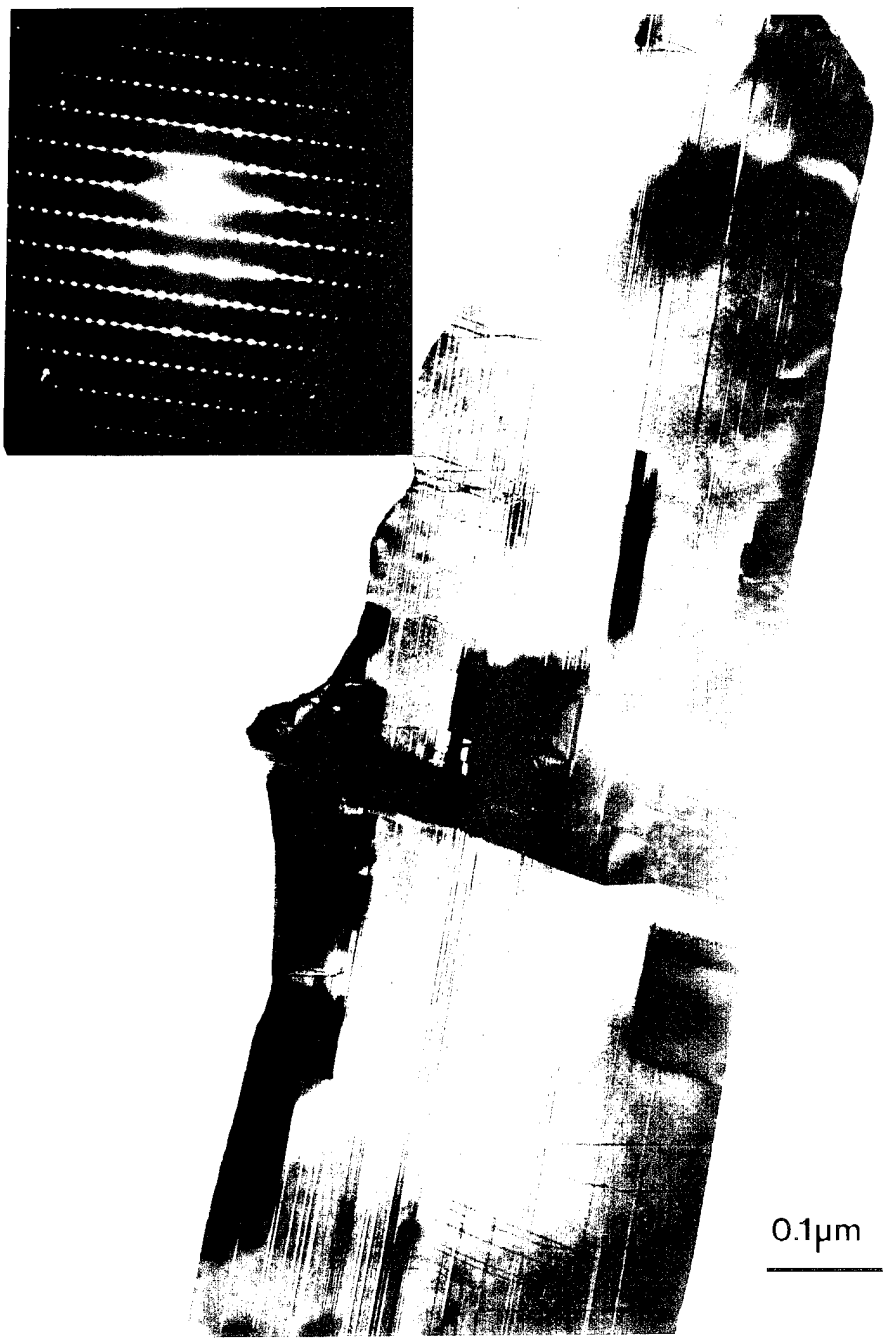

(a)

Figure 21 A hydride particle of duplex 48-2-2 charged at 13.8 MPa viewed along [100] direction, showing edge-on faults, (a) and viewed a few degree from [100], showing the intersections of faults, (b).

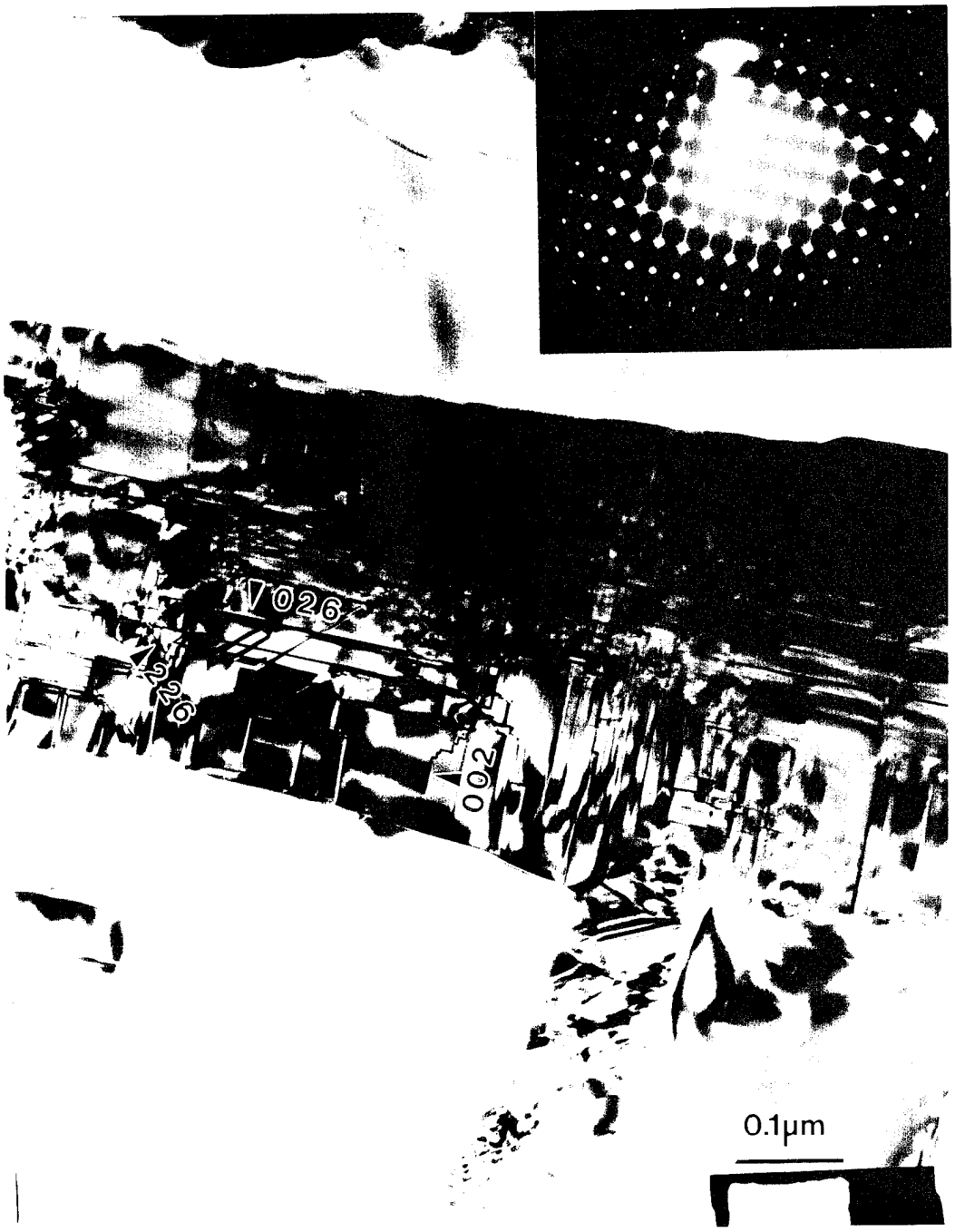

(b)

FIgur 21 Bright field image of a θ hydride showing faults with corresponding [031] zone diffraction pattern inset.

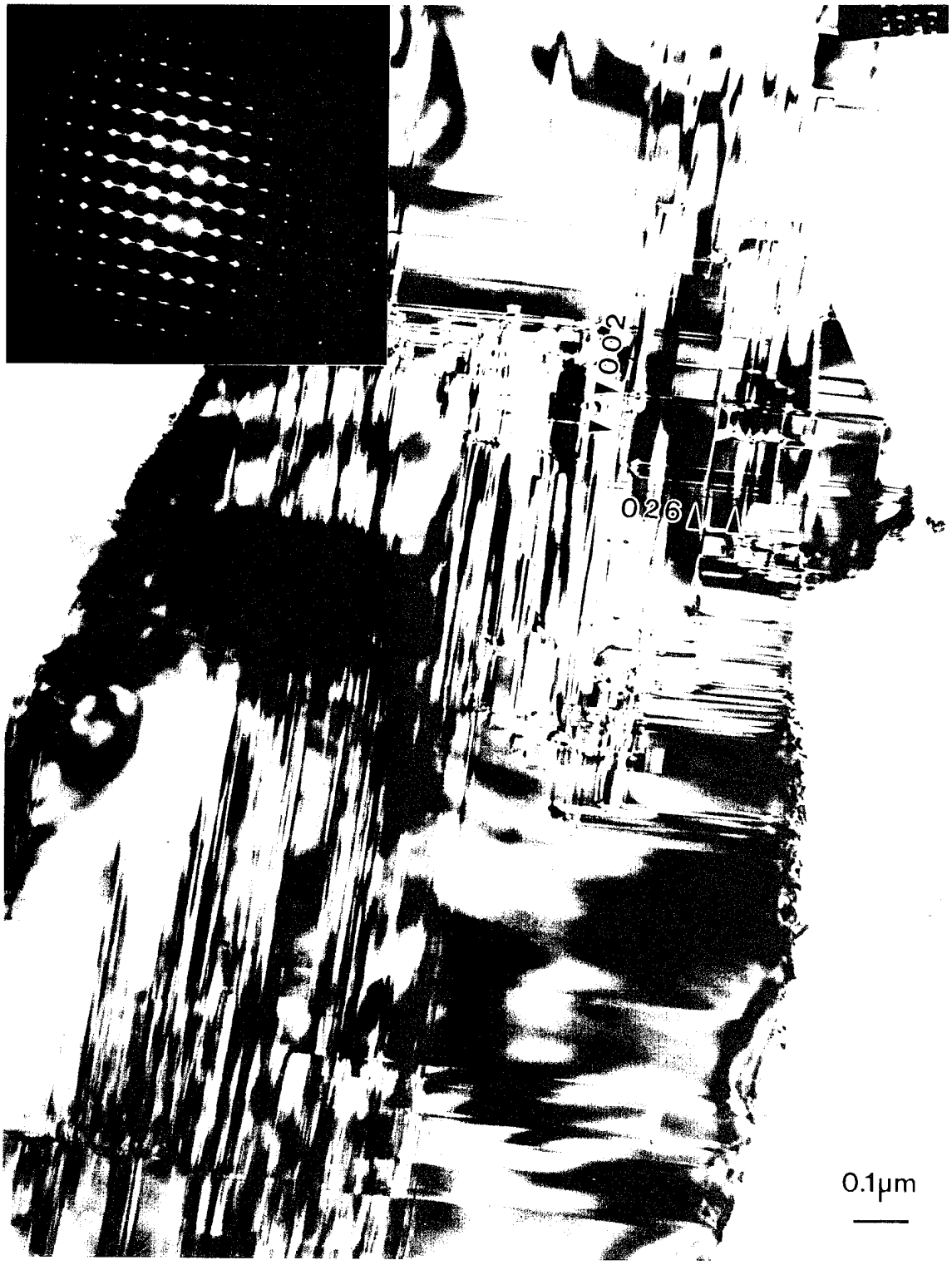

Figure 22 Bright field image of a θ hydride showing faults with corresponding [131] diffraction pattern inset.

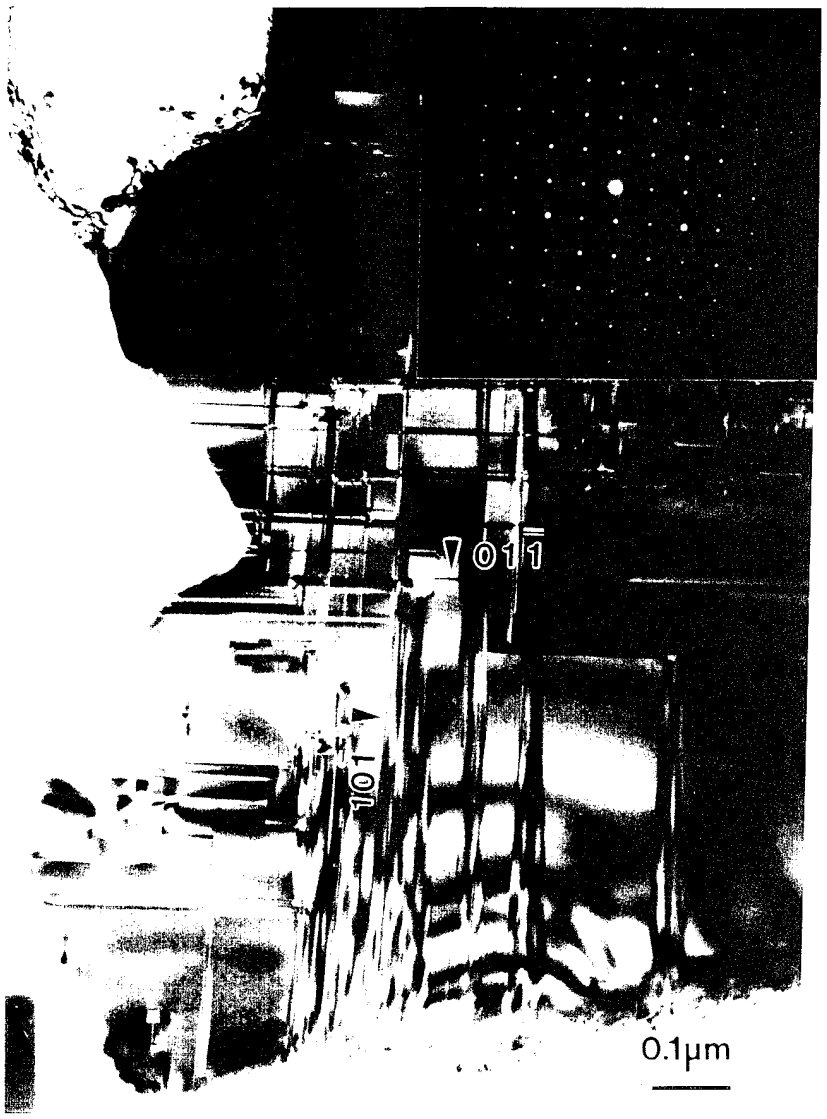

Figure 23 Bright field image of a θ hydride showing faults with corresponding [111] zone diffraction pattern inset.

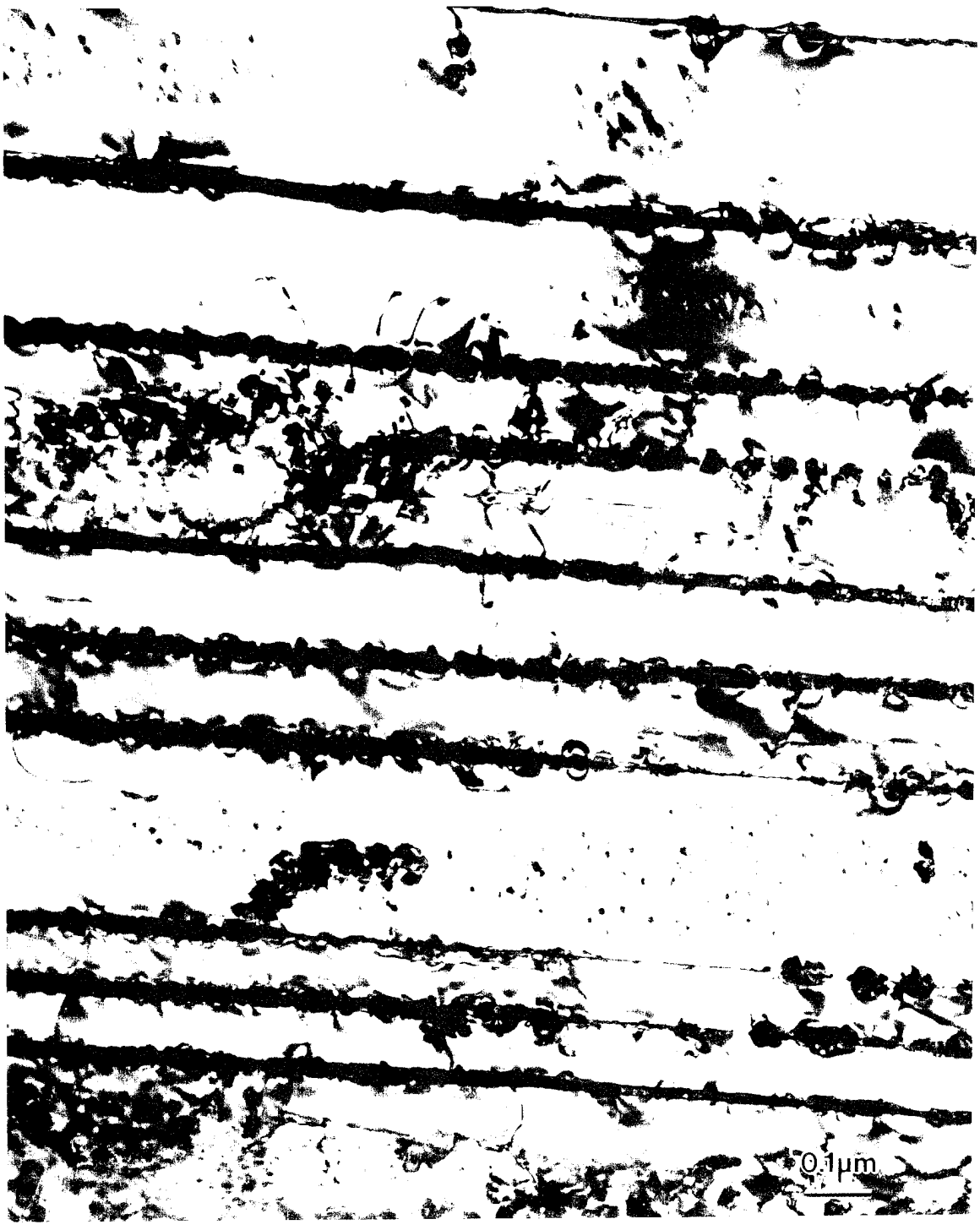

Figure 24 Bright field image of lamellar 48-2-2 charged at 7MPa showing a similar morphology as that in 13.8MPa charged material but with needle shaped precipitates dispersed in the γ laths. (a) and faceted hydrides present in γ laths and along a twin boundary (b).

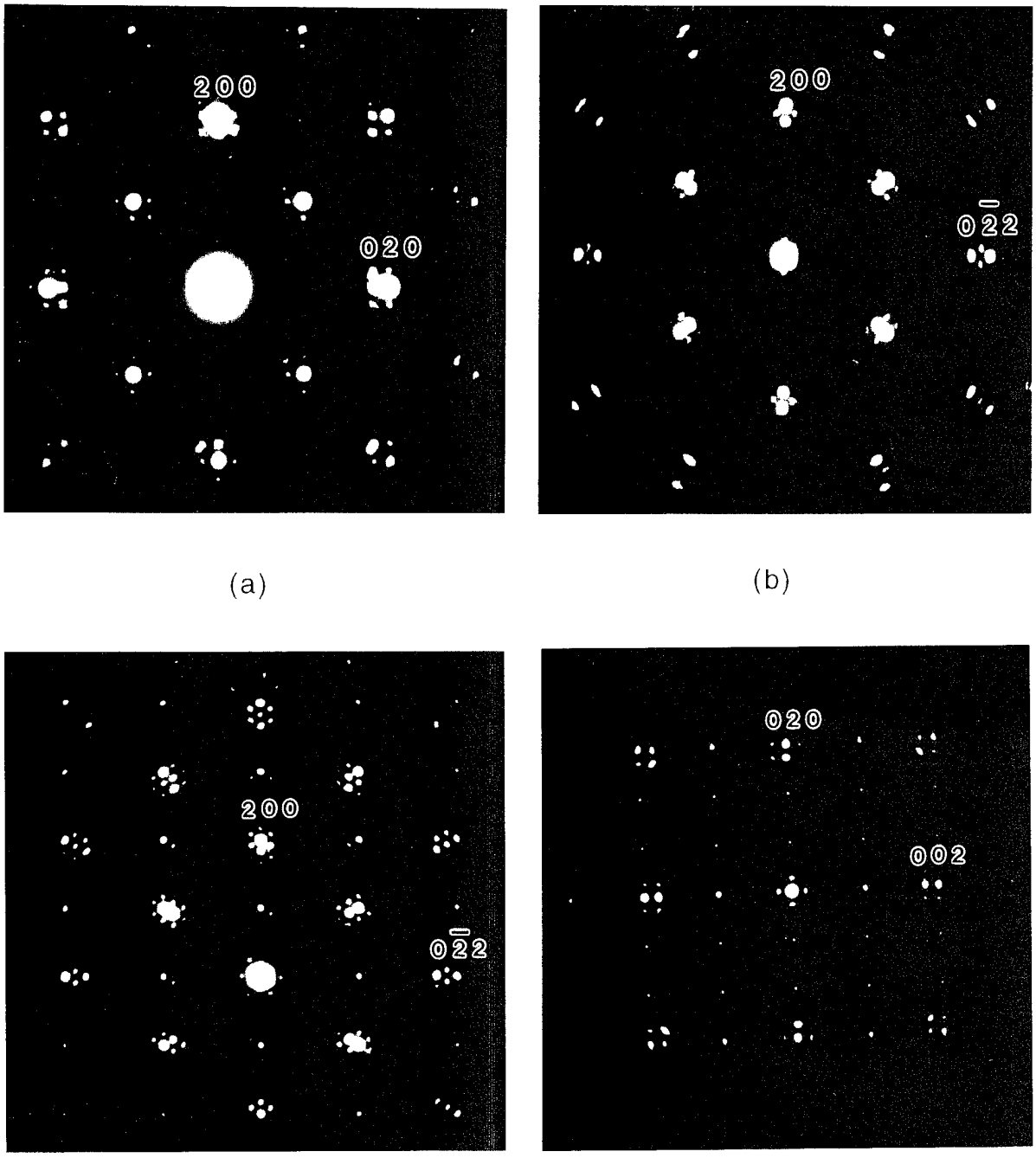

Figur 25 AD patterns of the γ phase and FCC hydrides showing a cube-on-cube orientation for 13.8 MPa charged duplex 48-2-2: [001], (a) ; [110], (C); [011], (b) and [100], (d).

The observation of SAD patterns corresponding to a number of low index zone axes, such as [001], [011], [110], [010], [012], [112] and [111], confirmed the presence of a FCC hydride with a lattice parameter of a = 4.45 Å, Figure 25. All SADPs consistently exhibited a clear crystallographic relationship with respect to the γ matrix. The hydride and matrix possess a cube-on-cube orientation relationship, that is $(001)\gamma//(001)_\delta$, $[100]\gamma//[100]_\delta$. Thus, the hydride was isomorphous with TiH_2, the δ titanium hydride, which has a FCC structure with a lattice parameter of a = 4.45 Å.

It is interesting to note that satellite spots appeared in all the SAD patterns, Figure 25(a)-(h), arising from double diffraction due to the fact that hydrides were precipitated in the γ matrix. A computer simulated pattern, Figure 26, was generated using the two unit cells: the γ phase, a = 4.03 Å, c = 4.12 Å and the δ phase, a = 4.45 Å under beam direction [001]. The principle for simulation is as follows: initially, the patterns are superimposed with the center spots together to produce the basic pattern expected from both crystals under beam direction [001]. Each diffracted beam in the γ phase then served as an incident beam for the δ hydride, and the locations of the spots arising from double diffraction are then obtained by superimposing the characteristic diffraction pattern from the hydride on that of γ phase, but with the origin of the former displaced to strongly diffracted spots [1]. It is apparent that the positions and the relative intensities of the satellite spots in the simulated pattern agree well with the observed [001] pattern.

TEM bright field images of the FCC hydrides showed a facetted morphology. The hydrides have sizes ranging from 10 nm to 100 nm. Moiré fringes associated with hydrides are clearly visible. Close inspection of the images, particularly the very small precipitates, under beam directions [001] and [010] revealed a cubic or an octahedral shape. Apparently, the hydride formation was associated with defects, such as dislocations, grain

or twin boundaries which are likely to be due to the fact that the misfit between γ and the hydride phases is approximately 11% along the [100] direction. The presence of dislocations around the hydrides indicates that the accommodation of the hydrides in the γ matrix involves some degree of plastic deformation. The high contrast in the γ matrix adjacent to the hydride particles clearly demonstrated a significant amount of elastic strain associated with the hydride formation, Figure 27.

3.3.2 Lamellar Ti-48Al-2Cr-2Nb

The fully transformed lamellar microstructure of 48-2-2 was produced by heat treatment at 1400 °C for 3 hrs, Figure 28(a). Fully lamellar structures from the wrought material were subjected to hydrogen charging at pressures of 7 MPa and 13.8 MPa (second charging) for 60 hrs at 800 °C. The resultant hydrogen uptake for the forged sample charged at 13.8 MPa was 2270 wppm, compared to 3900 wppm for duplex 48-2-2 and 640 wppm for the single phase Ti-52 Al materials charged under the same conditions, Table II.

The X-ray spectra for the initial, hydrogen charged samples of lamellar structure at 7 MPa and 13.8 MPa are given in Figures 29(a)-(c). The X-ray spectrum of the precharged materials exhibited the peaks characteristic of the γ and α_2 phase, Figure 29(a). X-ray spectra following hydrogen charging at 7 MPa and 13.8 MPa revealed no traces of the α_2 phase, but did indicate the presence of a large amount of the γ phase. In addition, new peaks of low intensity compared to the γ phase were observed, Figure 29(a) and (b). These could be attributed to the presence of the FCC hydride with a lattice parameter of a = 4.45 Å. This result suggests that the bulk α_2 phase, which contains a high proportion of Ti, converts to the hydride phase. As a consequence of texture in the bulk sample, the peak

intensities do not agree with theoretical values. The low intensity of the hydride peaks resulted from the small volume fraction of hydride.

Figure 28(a) shows the microstructure of 48-2-2 in the pre-charged lamellar condition. The charging experiments conducted at 7 and 13.8 MPa produced similar microstructural morphology at BSE level, Figure 28(b) and 30. Unlike the duplex materials, the lamellar character of the microstructure was retained to a greater degree and traces of the original lamellar morphology are still clearly visible, Figure 28(b) and 30(a). SAD examination did not reveal any traces of the α_2 phase, a result consistent with the X-ray observations. TEM studies confirmed that the structure and lattice parameter of the hydrides were identical to the δ FCC hydride produced in the duplex 48-2-2 charged at 13.8 MPa. Hydrides with a facetted morphology similar to those observed in the duplex material were present in the prior α_2 regions as well as within the γ laths and along lamellar and twin boundaries, Figure 31(a) and (b). Bright field images also revealed Moiré fringes associated with hydrides, Figure 31 and 32. A higher volume fraction of hydrides was generated in the material charged at 13.8 MPa, compared to that at 7 MPa due to the fact that the former material absorbed more hydrogen than the latter. Also, with the lower charging pressure, small platelet shaped precipitates were observed within γ laths, Figure 31, while facetted hydrides were observed in the γ laths, Figures 32(a) and (b). Legzdina, et al. have suggested [2] that these small hydride platelets observed at γ laths may have formed during cooling from the hydrogenation temperature at 800°C, whereas the larger hydrides presumably formed during charging where they had the opportunity to attain a low energy configuration and undergo coarsening. This is based on the fact that both sets of hydrides have the same crystal structure and same growth morphology, but differ greatly in size.

Hydride precipitation occurred on a number of different low index planes of the γ laths of the lamellar microstructure, Figure 32. Apparently this profuse hydride precipitation on a

variety of different low index planes results in partial loss of the lamellar character of the microstructure, as apparent when observed at the BSE level, Figure 30(b).

3.3.3 Single Phase Ti-52Al

The microstructure of the single γ phase Ti-52 Al, which was subjected the same heat treatment of the duplex 48-2-2, is shown in Figure 33(a). The Ti-52 Al material was composed of single phase γ grains (with grain size in the range of 100 - 300 μm). A small volume fraction of precipitates was distributed along the grain boundaries and throughout the matrix, and was assumed to be a consequence of the casting processing conditions. EDS analyses performed in an AEX 200 Transmission Electron Microscope confirmed that the particles are alumina.

The X-ray spectra for the initial and hydrogen charged samples are given in Figure 34 (a) and (b). Following heat treatment at 1280 °C/3 hrs + 900 °C/4 hrs, air cool, the X-ray spectrum of the initial microstructure consisted of peaks only from the γ phase, Figure 34(a). Charging at 13.8 MPa, resulted in a hydrogen uptake 640 wppm, Table II, which was much lower compared to duplex and lamellar 48-2-2 charged under the identical pressure. Apparently, it is due to the fact that γ phase has a much lower hydrogen solubility compared to α_2 phase. BSE micrographs showed precipitates preferentially along grain boundaries as well as in interior grains, Figure 33(b). The precipitate distribution in interior grains was somewhat inhomogeneous, apparently due to the segregation from the casting process. X-ray analysis confirmed that the precipitates were δ FCC hydrides, identical to the FCC hydrides observed in duplex and lamellar 48-2-2. A TEM bright field image, Figure 35, revealed cubic and octahedral hydrides aligned in the γ matrix under beam direction $[011]_\gamma$. Resolved Moiré fringes are clearly visible and the SAD patterns of the hydrides appeared to be identical to those obtained from lamellar and duplex 48-2-2.

Although FCC hydrides are predominantly present along grain boundaries and in the γ phase region, tetragonal θ hydride grains identical to the hydrides observed in the duplex 48-2-2 charged at 13.8 MPa, were also occasionally detected in the γ matrix. Figure 36 shows a θ hydride particle embedded in γ matrix and surrounded by a high density of dislocations. The θ hydride imaged under [120] zone axis showed lattice fringe patterns, similar to those observed at duplex 48-2-2 under [hk0] directions. A micrograph at relatively higher magnification for the same hydride grain exhibited resolved fringes with corresponding SAD pattern inset, Figure 37 and 38. The SAD pattern did reveal a deviation of the spot periodicity parallel to c* of the proposed θ phase. This may indicate the presence of a phase closely related to the θ hydride. Such deviations in this periodicity were also occasionally noted in the 48-2-2 duplex material.

In a number of regions, the FCC and θ hydrides were closely spaced at a distance as small as a few micrometers. This may indicate that the compositional conditions are such that a three-phase $\gamma - \delta - \theta$ region exists, or alternatively that the precipitation kinetics for δ hydrides is rapid and abundant precipitation occurs during cooling from the charging temperature. Due to lack of further availability of high pressure hydrogen facilities, it was not possible to examine this issue further.

To explore the effect of alloy composition, particularly the Ti/Al atomic ratio, on hydride formation, EDS analyses were performed on large number of FCC and θ hydride precipitates and the surrounding γ matrix of 48-2-2 and Ti-52 Al, both charged at 13.8 MPa in hydrogen gas, Table V - VI. A parallel study was also performed on the TEM foils of duplex 48-2-2 which had predominantly FCC and θ hydrides present from the second charging experiment, Table VII. The average values of the Ti/Al ratios measured from a

few particles from each foil are given in Tables V - VII. It is apparent that FCC and θ hydrides observed in 48-2-2 (second charging) and Ti-52 Al both are Ti rich, while the TiAl matrix is Al rich. In the 48-2-2 duplex material where the hydrides were predominantly the θ hydrides, the matrix on average was Ti rich. Again this may indicate that the differences in the hydride populations between the first and second high pressure charging experiments are due to macrosegregation in the forging. The data for the Ti/Al ratios of FCC hydrides in Ti-52 Al have large scatters over a range of 1.14 to 2.19. On the contrary, FCC hydrides of duplex 48-2-2 appeared to have ratios over a narrow range of 1.40-1.42. Since FCC hydrides of single γ phase originated from the grain boundaries, twin boundaries as well as interior γ grains, a wide range of Ti/Al ratios might be expected.

Table V - EDS Results of Single γ Phase Ti-52Al

Following H charging at 13.8 MPa

File Name	H-5212H13-A5G-1		H-5212H13-A5G-2		H-5212H13-A5G-3		H-5212H13-A5G-4		H-5212H13-A5G-5		H-5212H13-A5G-6	
Particle ID	γ-matrix		FCC Hydride		FCC Hydride		Tetragonal Hydride		Al_2O_3		FCC Hydride	
Element Line	Ti	Al	Ti	Al	Ti	Al	Ti	Al	Ti	Al	Ti	Al
Weight %	57.42	42.58	66.88	33.12	79.51	20.49	73.04	26.96	5.89	94.11	72.78	27.22
Atomic %	43.17	56.83	53.22	46.78	68.61	31.39	60.41	39.59	3.41	96.59	60.10	39.90
Ti/Al (At%)	0.76		1.14		2.19		1.53		0.035		1.51	

Table VI - EDS Results for Hydride and γ Phase Compositions in Duplex 48-2-2 Charged at 13.8 MPa (First Charging)

Element	γ				γ Ave.	θ				θ Ave.
Al (a/o)	50.71	44.31	34.56	51.82	45.35	36.60	34.43	34.29	35.95	35.33
Ti (a/o)	46.37	52.08	61.78	46.65	51.52	59.58	61.13	61.19	59.66	60.39
Ti/Al(a/o)	0.9	1.18	1.79	0.9	1.14	1.63	1.78	1.78	1.66	1.71

Table VII - EDS Results for Hydride and γ Phase Compositions in Duplex 48-2-2 Following 13.8 MPa H Charging (Second Charging)

File Name	H-4812H13-IW-1a				H-4812H13-IW-1b		H-4812H13-IW-2a				H-4812H13-IW-2b	
Particle ID	FCC Hydride				FCC Hydride		γ- matrix				γ- matrix	
Element	Ti	Al	Cr	Nb	Ti	Al	Ti	Al	Cr	Nb	Ti	Al
Weight %	62.98	25.05	6.37	5.61	71.27	28.73	54.89	37.21	2.02	5.88	59.47	40.53
Atomic %	54.20	38.27	5.05	2.49	58.28	41.72	43.62	52.49	1.48	2.41	45.25	54.75
Ti/Al (at%)	1.42				1.40		0.83				0.83	

It is reasonable that the FCC hydrides should have a higher Ti/Al ratios than the measured values due to the fact that the hydrides are preferentially embedded in the γ matrix. Some

amount of the γ matrix would inevitably be sampled by the electron beam when measuring composition. Considerable caution was taken in an attempt to reduce the sampling effect. The Ti/Al maximum ratio of 2.19 was obtained by examination of a FCC hydride cube located closely to the edge of the foil. It is thus thought that this value was closest to the true value. Additionally, the θ hydride observed in Ti-52Al has a Ti/Al atomic ratio of 1.53 which is very close to the results obtained from the θ hydrides of duplex 48-2-2 (Ti/Al =1.63-1.78).

3.3.4 Reversibility of Hydride Formation

To confirm the reversibility of hydride formation, degassing experiments were conducted on charged samples. Degassing in vacuum was carried out in the Sieverts apparatus at 900 °C for 48 hrs for all the lamellar and duplex 48-2-2 and single γ phase Ti-52 Al charged at 7 MPa and 13.8 MPa. Additionally, for the duplex 48-2-2 charged at 13.8 MPa degassing was also conducted at 1050 °C.

Following degassing in vacuum in a temperature range of 900 to 1050 °C, hydrogen was removed and the original phases restored for all the three microstructures, indicating that the hydride formation process is reversible. For lamellar 48-2-2 charged at 13.8 and 7 MPa, the original phase and original microstructural features were restored following degassing in vacuum at 900 °C, as indicated by X-ray and BSE results, Figure 39 and 40. BSE images and corresponding X-ray spectra were also obtained form the single γ phase Ti-52 Al charged at 13.8 MPa and subsequently degassed at 900 °C, Figure 41. The microstructure consisted of equiaxed γ grains plus small particles dispersed in the γ matrix, which were believed to be alumina. No distinguishable features were found in the BSE image and X-ray spectra compared to the situations prior to charging and following outgassing. Although the X-ray spectrum of the duplex 48-2-2 charged at 13.8 MPa and

degassed at 900 °C, indicated the original two phase structure of γ and α_2, had been restored, the BSE images revealed that the outgassed microstructure predominantly consisted of small blocky α_2 grains along grain boundaries and equiaxed γ as well as γ twins without any trace of the lamellar morphology, Figure 42. Additionally, no lamellar colonies were observed at the TEM level of observation. Slight coarsening of the α_2 grains and a higher volume fraction of γ annealing twins were observed in the duplex 48-2-2 samples degassed at 1050 °C compared to those degassed at 900 °C, Figures 42 (a) and 43(a). Additionally, the density of α_2 grains appeared to be variable from region to region, Figures 42(a) and 43(a) + (b). Although the original phases were restored, it is apparent their original morphology was not. This may be due to some redistribution of Al and Ti during the charging process.

3.3.5 Surface Microstructures Following Charging

In experiments conducted in both the Sieverts apparatus and the high pressure charging chamber significant microstructural differences were observed in the surfaces of some of the samples compared to the interior for the duplex 48-2-2 samples following charging at 0.1 and 13.8 MPa. These differences were only apparent under charging conditions where trace amounts of impurities were available (under conditions where samples were not wrapped in gettering Ta foils). These surface observations are summarized here due to the insight which they provide about the early stages of hydride formation. Additionally, they are relevant to earlier reports on the existence of hydrides after low pressure charging. Also, these observations may be technologically relevant, since in the manufacturing or service environments of these materials, more complex environments than pure hydrogen are likely to be encountered.

Blanks for this portion of the study were inserted in a quartz tube, evacuated and subsequently back filled with hydrogen to obtain a pressure of 0.1 MPa at exposure temperature. Ta was apparently an effective oxygen gettering agent, since the observations reported in the section apply only to those samples which were not Ta wrapped. A very thin bluish surface layer was observed following charging. The surfaces of all microstructural variants were examined by X-ray, SEM, TEM and Auger analyses. TEM foils were produced in the following manner: 3 mm disks were first mechanically punched. Then one side of each disk was slightly polished to remove the roughness, the other side was back-thinned and dimpled with a minimum thickness of approximately 30 μm. The disks were jet-polished in a solution consisting of 300 ml methanol, 180 ml butanol and 30 ml perchloric acid, maintained at -50 °C to -54 °C and 22.5 V.

TEM BF field images revealed the presence of large, dispersed oxide particles on the surface of duplex 48-2-2 charged at 0.1 MPa and 740 °C, Figure 44. The SAD ring pattern, Figure 44(c), taken from the dispersed particles confirmed the oxide to be Al_2O_3 with a rhombohedral structure and lattice parameters of a = 0.4844 nm and c = 1.324 nm, which can be described alternately as a hexagonal structure with lattice parameters of a = 0.5544 nm and c = 9.024 nm [3]. Although the volume fraction of the Al_2O_3 particles is fairly high, formation of a completely continuous oxide layer did not occur.

No hydride phases were observed in X-ray spectra, BSE images or TEM foils removed from the interior regions of the charged samples. The resultant X-ray spectrum of the isothermally forged duplex 48-2-2 charged at 0.1 MPa, is characteristic of γ and α_2 phases with no indication of peaks corresponding to other phases, Figure 45(b). A cross sectional BSE image, Figure 45(a), showed a microstructure similar to that the pre-charged material, Figure 1, with only slight differences; a few dark-contrast particles were embedded in the

matrix. Apparently, particles with bright contrast are the α_2 phase or lamellar colonies in the γ matrix. However, a small fraction of tetragonal hydrides in the α_2 laths of lamellar colonies and δ FCC hydride precipitates in equiaxed γ grains were observed in the surface foils, Figures 46 and 47. Figures 46(a) and (b), show the presence of lattice fringes in the α_2 laths with spacing ranging from 14 Å to 50 Å under beam direction $[11\bar{2}\ 0]\alpha_2$. The corresponding SAD patterns revealed the presence of extra reflections at locations of 1/3 and 2/3 between the transmitted spots and $(0001)\alpha_2$ spots when the beam direction is $[11\bar{2}\ 0]\alpha_2//[1\bar{1}\ 0]\gamma$. These spots are not as intense as those observed in the [hk0] θ phase, but they are intense enough to be distinguishable. The rest of the pattern is identical to the γ–α_2–γ twin pattern under $[1\bar{1}\ 0]\gamma$ zone axis. However, the appearance of distinct spots implies that a new structure, the θ hydride, is developing. Apparently, the θ hydrides are still in the early stage of growth. The α_2 and γ laths shown in Figures 46(a) and (b) are extremely fine. The X-ray beam employed in the EDS examinations sampled a region of approximately of 0.5 μm x 0.5 μm. Thus, it is not possible to measure the Ti/Al ratio of each individual lath. The average ratio over approximately half number of the lamellar laths of the colony in Figure 70(a), was 1.4. Assuming that the volume fractions of the γ and α_2 laths in the colony are approximately equal and the Ti/Al ratios of the γ laths are close to 1, this yields a Ti/Al ratio of the α_2 phase equal to 1.8, which is approximately the composition value of the α_2 phase at 800 °C in the equilibrium Ti-Al binary phase diagram. The estimated Ti/Al ratio of the α_2 phase is also similar to that measured for the θ hydride, which indicates that large scale diffusion redistribution of Ti and Al are not required for formation of the θ phase from the α_2 phase. These TEM observations confirm that the orientation relationship between the θ phase and α_2 or γ phases, is $(0001)\alpha_2//(111)\gamma//(001)_\theta$, $[11\bar{2}\ 0]\alpha_2//[1\bar{1}\ 0]\gamma//[100]_\theta$.

Slight differences were found in the bright field images shown in Figure 46(a) and (b). A few needle-like precipitates were also observed in the wider γ lath close to γ and α_2 lath interface, Figure 46(a). No SAD pattern was available due to the small sizes of the precipitates. However, their morphology resembles that of FCC hydride precipitates observed in the γ laths of lamellar 48-2-2 charged at 7 MPa, Figure 31(a). A higher density of such small precipitates was again observed in the equiaxed γ grains in the same TEM foil. Some elastic strains were associated with these precipitates and occasionally particles with Moiré fringes were observed. The shape, size and morphology of these particles are very different from oxides and bear a strong resemblance to the FCC hydrides.

Under these low pressure charging conditions, the hydrides populated only the surface region. A few lamellar colonies are shown in Figure 47, where a fraction of θ hydrides was observed in two lamellar colonies, Figures 46(a) and (b). Each colony in the same foil was carefully examined by SAD and bright field imaging. Although some BF images revealed a low density of lattice fringes in the α_2 laths, no extra recognizable reflections were observed in the SAD patterns of most lamellar colonies, indicating an irregular distribution of the surface hydride. Presumably, following charging the surfaces of the foils were not perfectly flat and the thickness removed during foil preparation was different from region to region.

Pronounced changes in the surface microstructure accompanied charging of the duplex materials at 13.8 MPa. Following the hydrogen exposure, a surface layer of a thickness varying between 10 and 150 μm was observed. Cross-sectional specimens imaged with back scattered electrons revealed regions of the γ phase and another phase with brighter contrast, similar in contrast to the hydrogen-induced phase in the interior. Embedded in the layer was a significant volume fraction of dark, blocky isolated particles, surrounded by Ti-enriched areas, Figure 48. BSE images viewed parallel to the surface regions of the same

cube showed an inhomogeneous microstructure. Dark rectangular or polygonal shaped particles with variable densities embedded in the brightly contrasted phase, are clearly visible, Figure 49.

WDX examination was performed on the large particles, brightly contrasting regions and γ regions. WDX analyses utilizing non-element standards revealed that the bright layer and γ matrix had compositions with a Ti/Al-ratio ranging from 1.58-1.77 and 1.01-1.07, respectively, Table VIII. Thus, the bright layer had a similar Ti/Al ratio as obtained from the tetragonal hydrides in the interior, which ranges from 1.63 to 1.78. The EDX results conducted on the dark large particles indicated the presence of considerable amounts of Al and O and little amounts of Ti, Cr, and Nb, Figure 50. Presumably the contents of Ti, Nb and Cr were due to the electron beam sampling of the γ-matrix.

Corresponding X-ray spectra for the surface of duplex 48-2-2 charged at 800 °C and 13.8 MPa, have been acquired. The observed peaks can be attributed to the presence of θ, γ phase, Al_2O_3 and TiO_2, Figure 51. Lattice parameters were consistent with Al_2O_3, with a rhombohedral structure, a = 0.4759 nm, c = 1.2992 nm and TiO_2 with a tetragonal structure and lattice parameters of a = 0.3785 nm, c = 0.9514 nm.

Table VIII - Ti/Al Ratios of Hydrides and γ Phases at the Surface Layers of Duplex 48-2-2 Following Charging in 13.8 MPa (WDX in SEM)

	Ti/Al (atomic)		
γ–matrix	1.03	1.07	1.01
Hydride	1.58	1.64	1.77

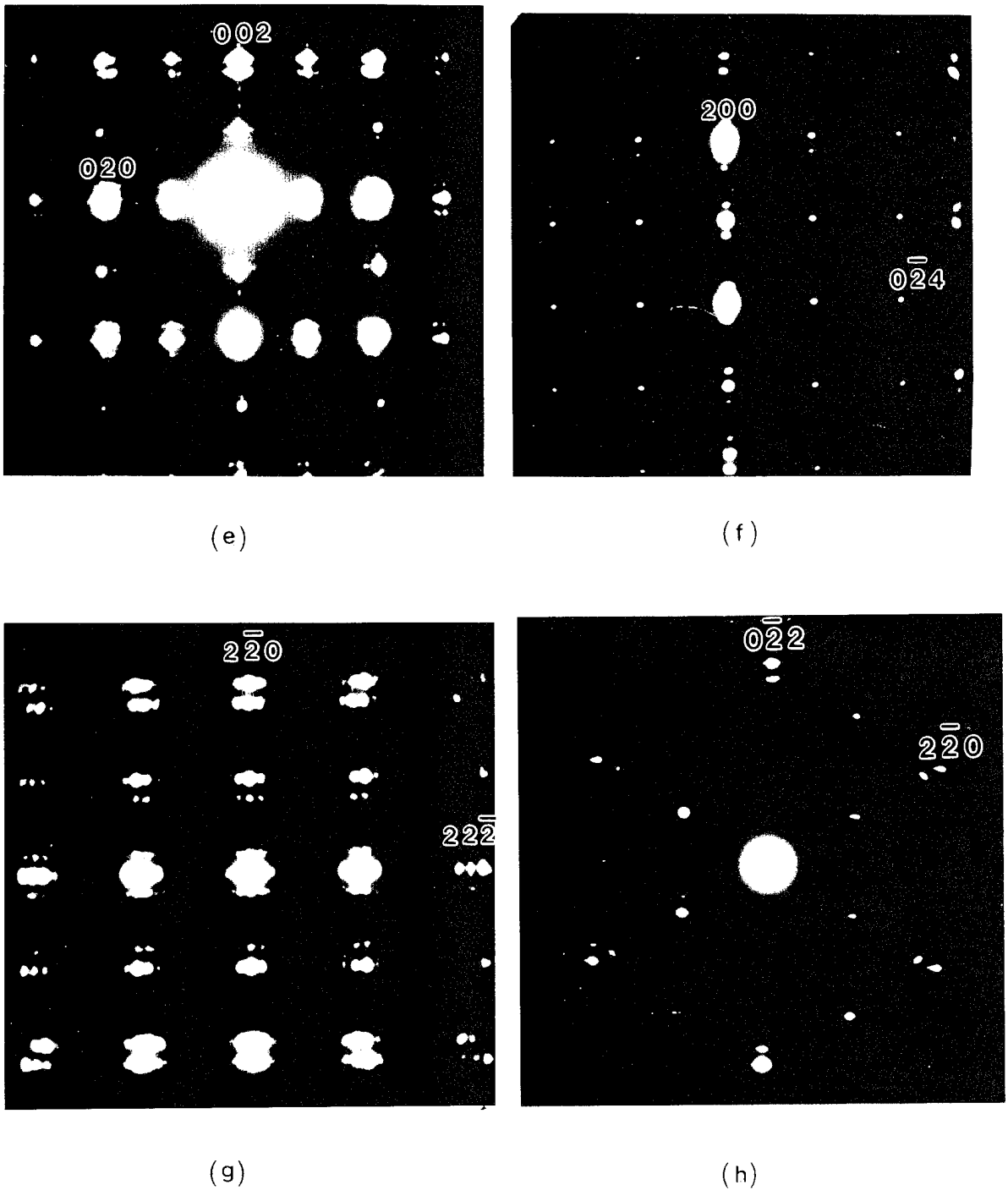

Figure 25 SAD patterns of the γ phase and FCC hydrides showing a cube-on-cube orientation for 13.8 MPa charged duplex 48-2-2 [100] + [010], (e) ; [012], (f); [112], (g) and [111], (h).

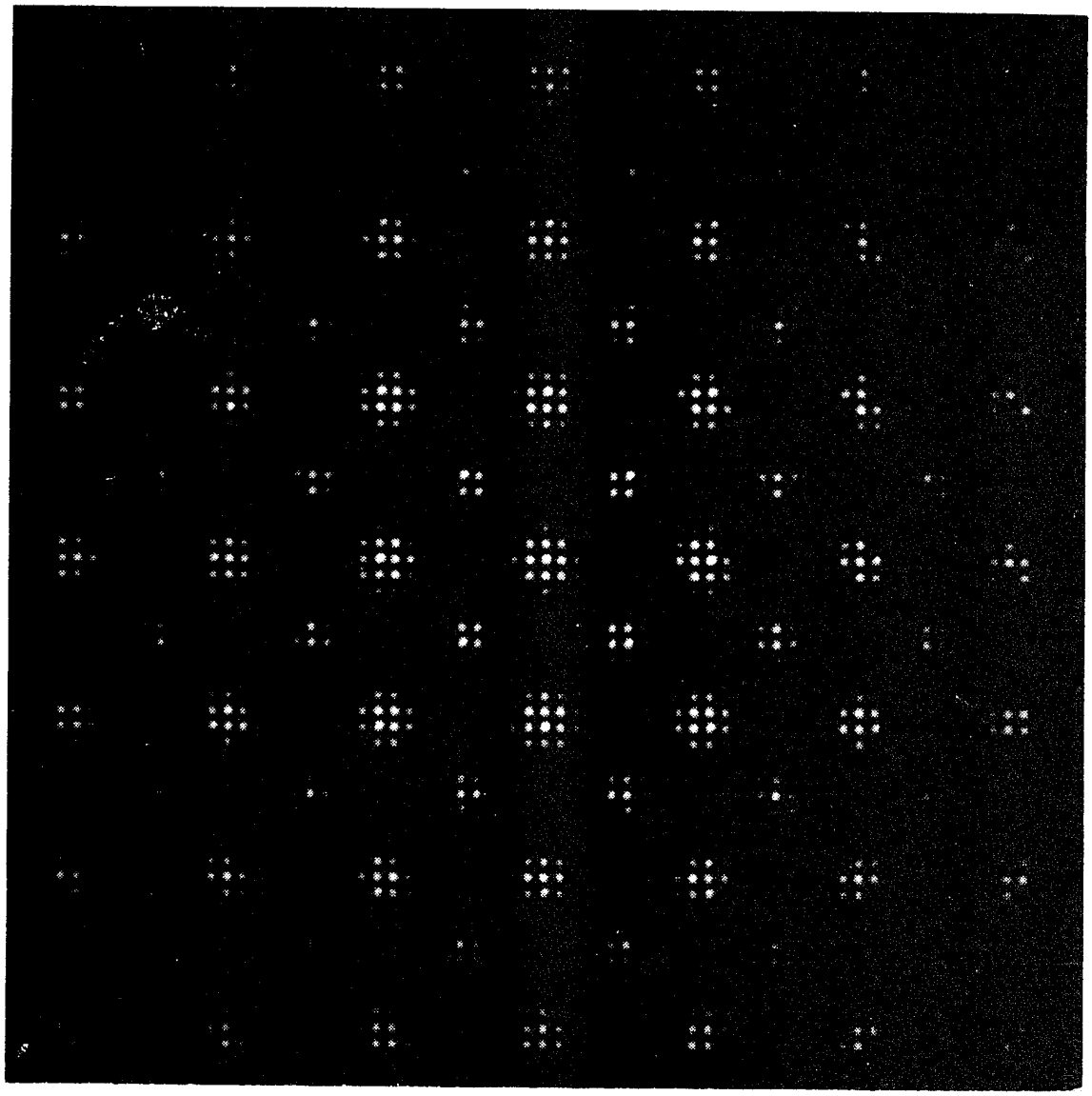

Figure 26 - Simulated diffraction pattern for FCC hydrides embedded in TiAl showing the effects of double diffraction.

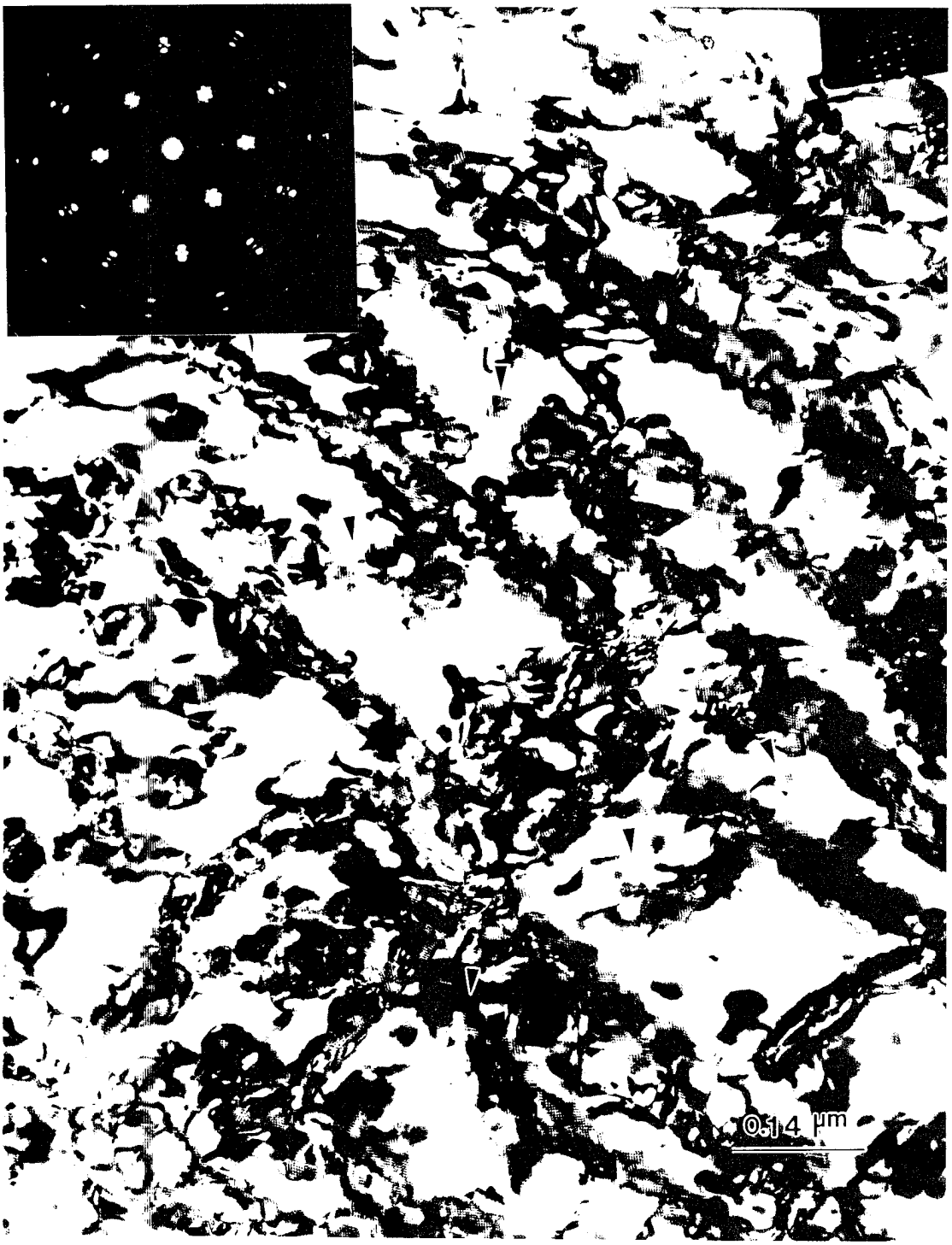

Figur 27 Densely populated faceted cubic hydrides embedded in γ matrix for 13.8 MPa charged duplex 48-2-2 under zone axis [011].

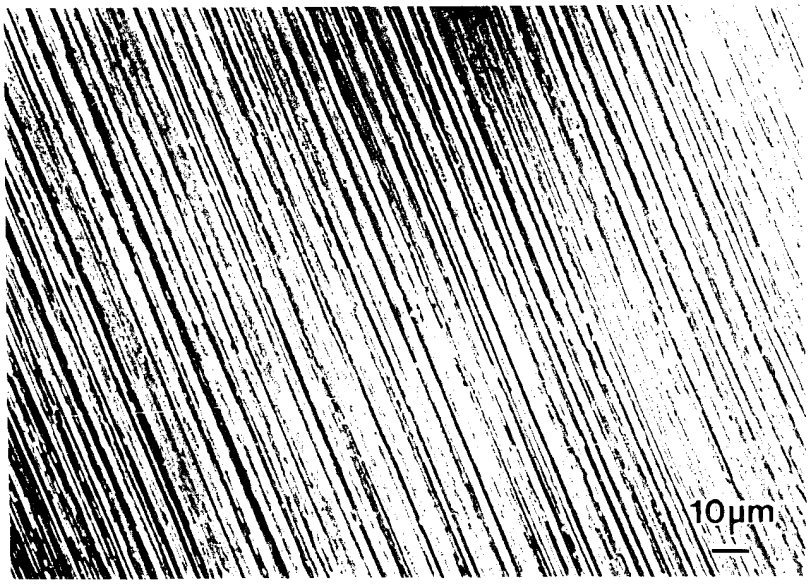

(a)

(b)

Figure 28 Microstructure of 48-2-2 in the pre-charged lamellar condition, (a) and following charging at 800°C and 7MPa for 60 hrs, (b).

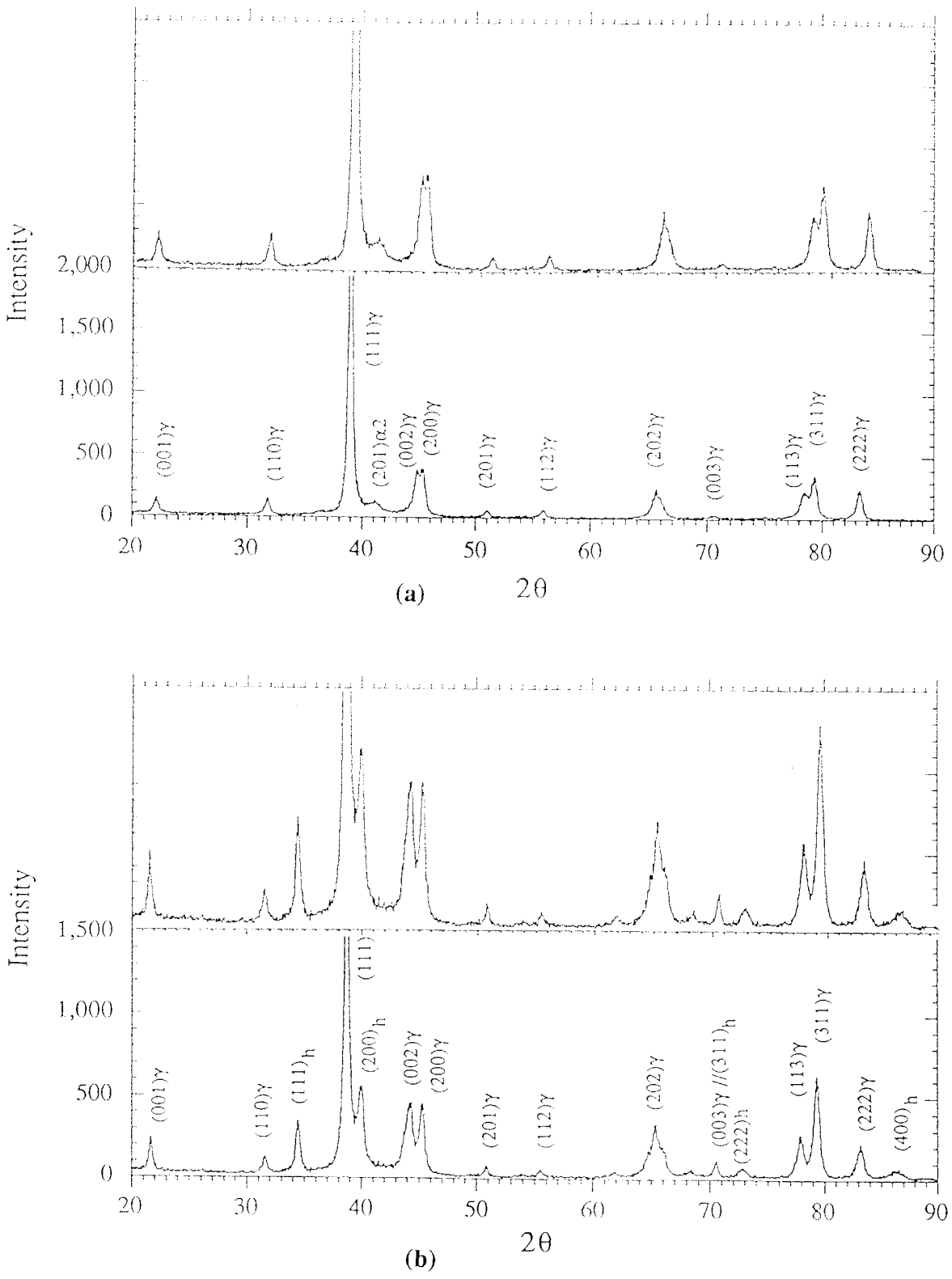

Figure 29 X-ray spectra of the pre-charged lamellar 48-2-2, (a); hydrogen charged at 800°C and 7MPa, (b) and charged at 13.8MPa, (c).

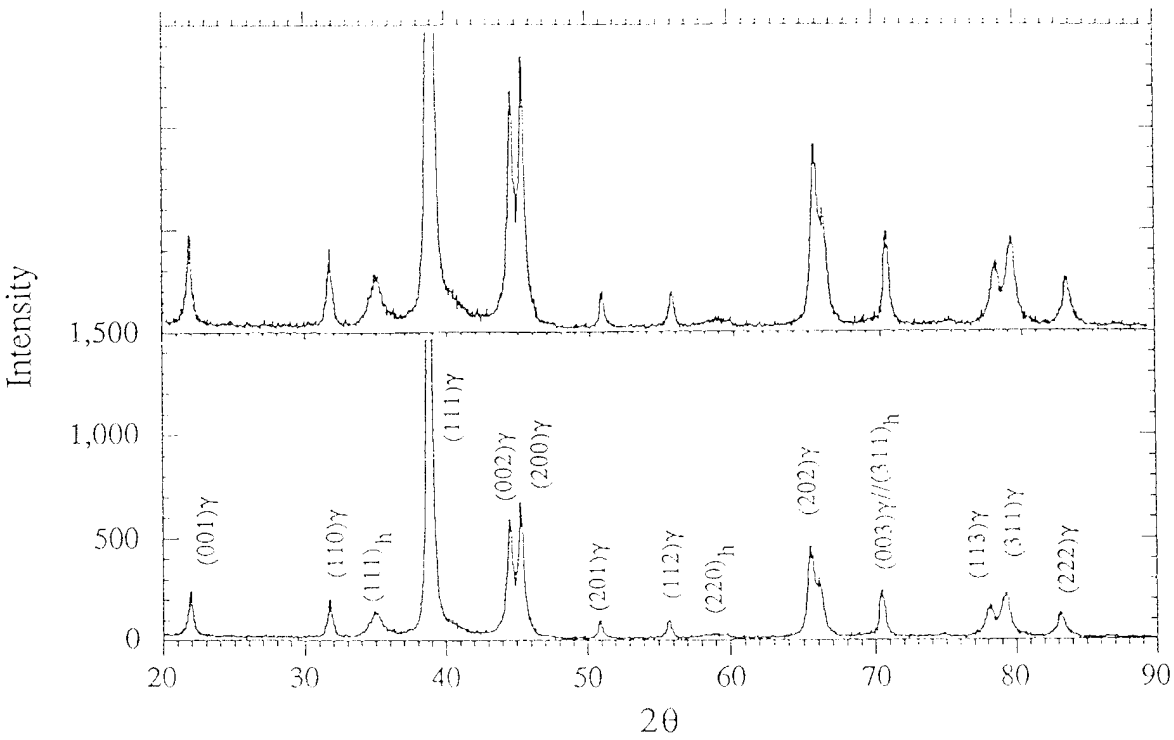
Intensity
1,500
1,000
500
0
20
30
40
50
60
70
80
90
2θ
(001)γ
(110)γ
(111)h
(111)γ
(002)γ
(200)γ
(201)γ
(112)γ
(220)h
(202)γ
(003)γ//(311)h
(113)γ
(311)γ
(222)γ

(c)

Figure 29

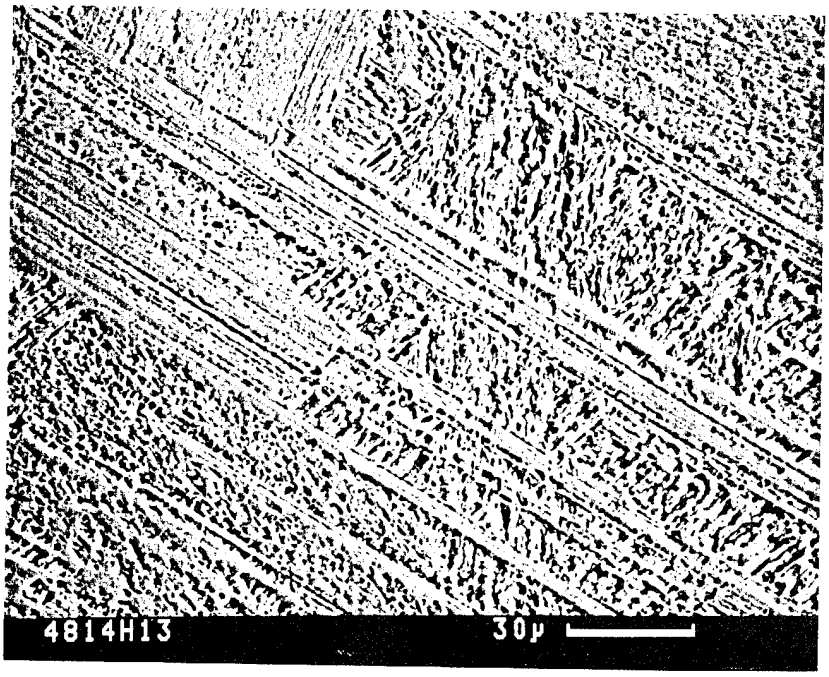

(a)

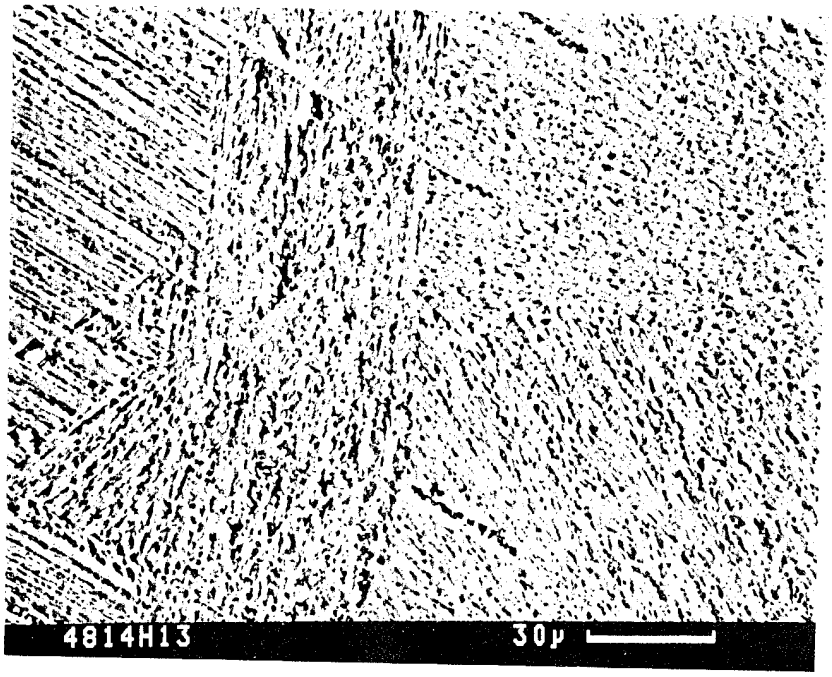

(b)

Figure 30 BS electron image of lamellar 48-2-2 charged at 13.8 MPa clearly showing the lamellar morphology (a) and partial loss due to hydride precipitation, (b).

Figure 31

Figure 32 TEM BF image of lamellar 48-2-2 charged at 13.8 MPa showing FCC hydrides.

(a)

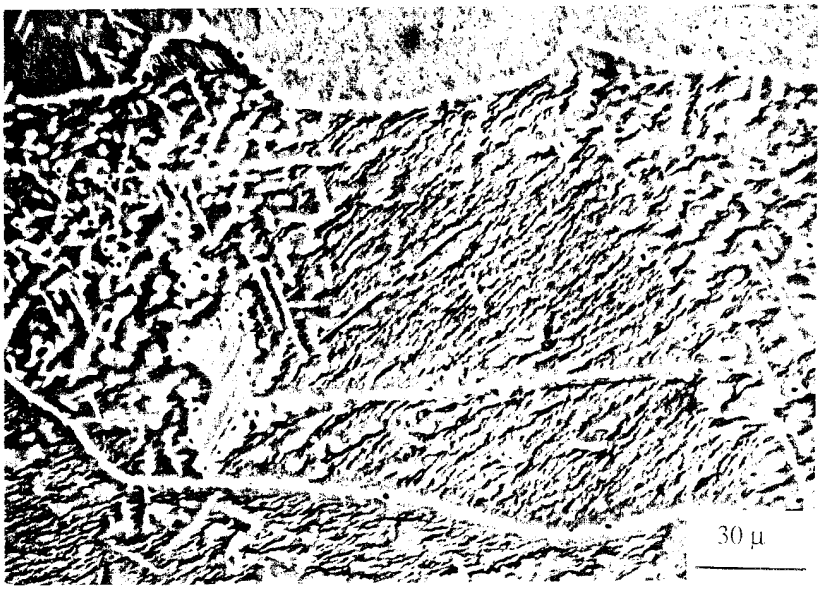

(b)

Figure 33 Microstructures of Ti-52Al prior to hydrogen charging, (a) and following charging at 800°C and 13.8MPa for 60 hours, (b).

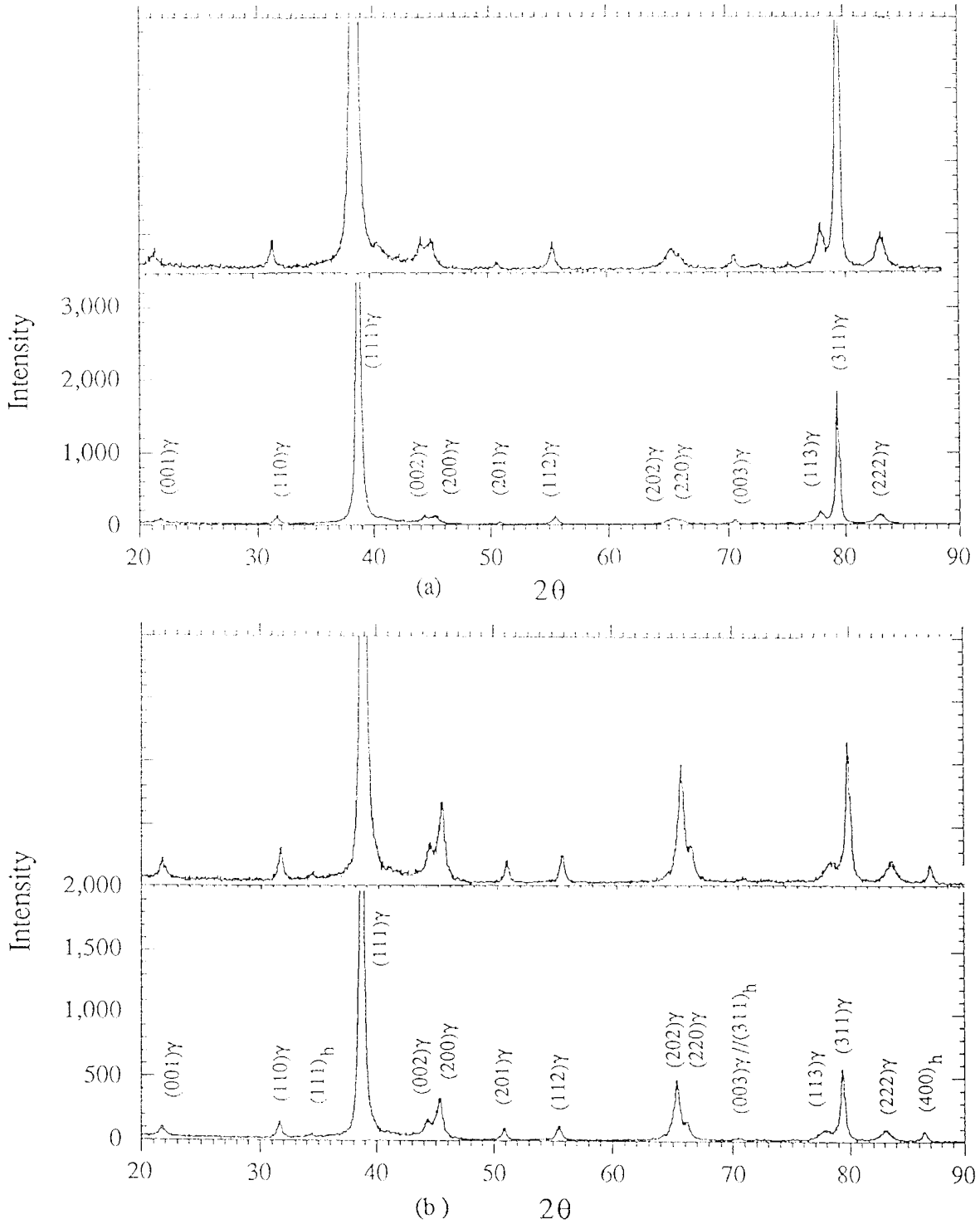

Figure 34 X-ray spectra of the pre-charged single phase γ Ti-52Al, (a) and hydrogen charged at 800°C and 13.8MPa, (b).

Figure 35 Bright field image of hydrides in Ti-52Al associated with dislocations. Moiré fringes associated with the faceted hydrides are visible under [011] zone.

Figure 36 TEM bright field image of the single phase γ Ti-52Al charged at 13.8MPa and 800°C revealing occational observation of θ hydrides embedded in γ matrix.

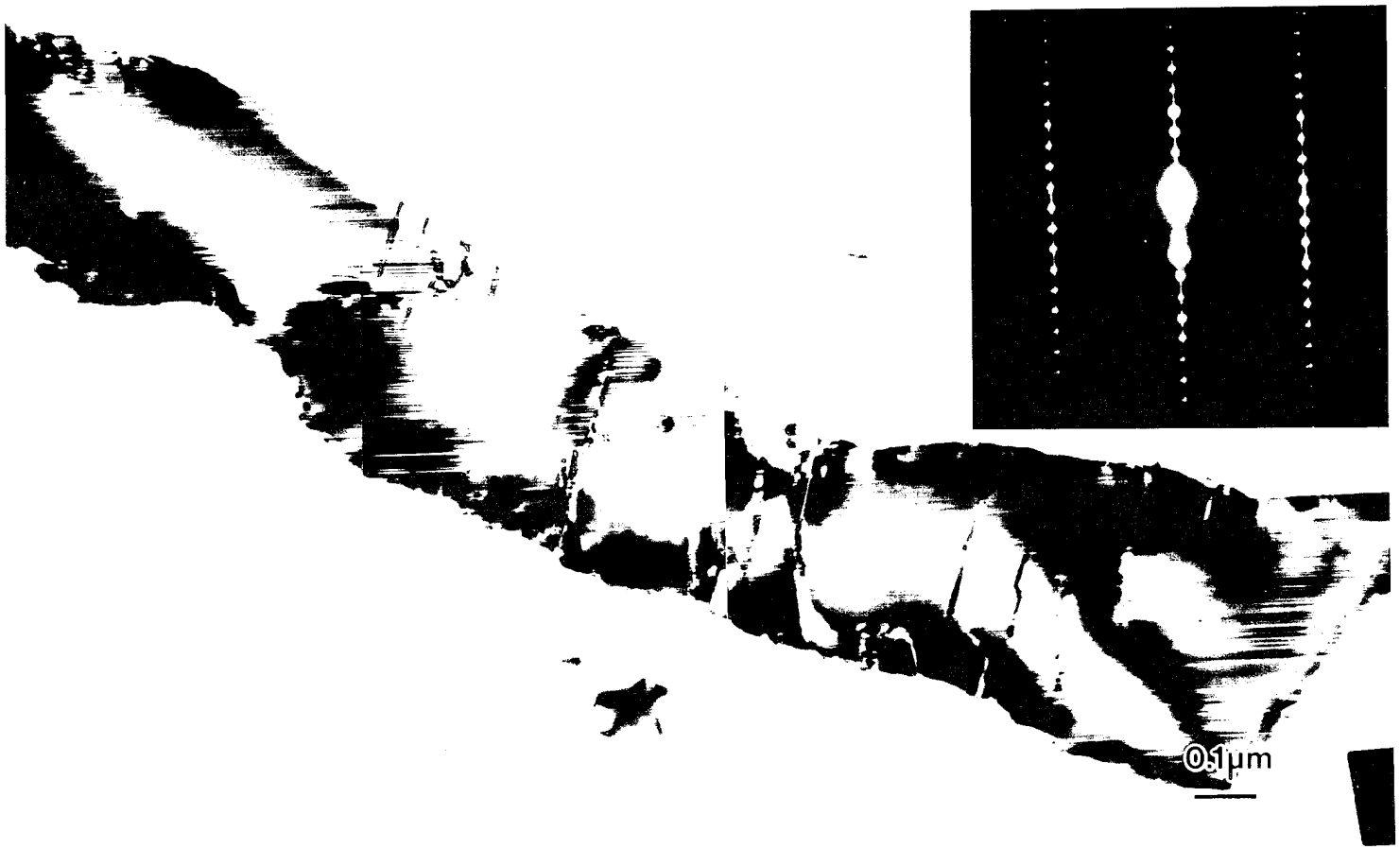

Figure 37 Tetragonal hydrides identical to those observed in 13.8 MPa charged duplex 48-2-2, were also occasionally observed embedded in γ matrix of Ti-52Al following charging at 13.8 MPa.

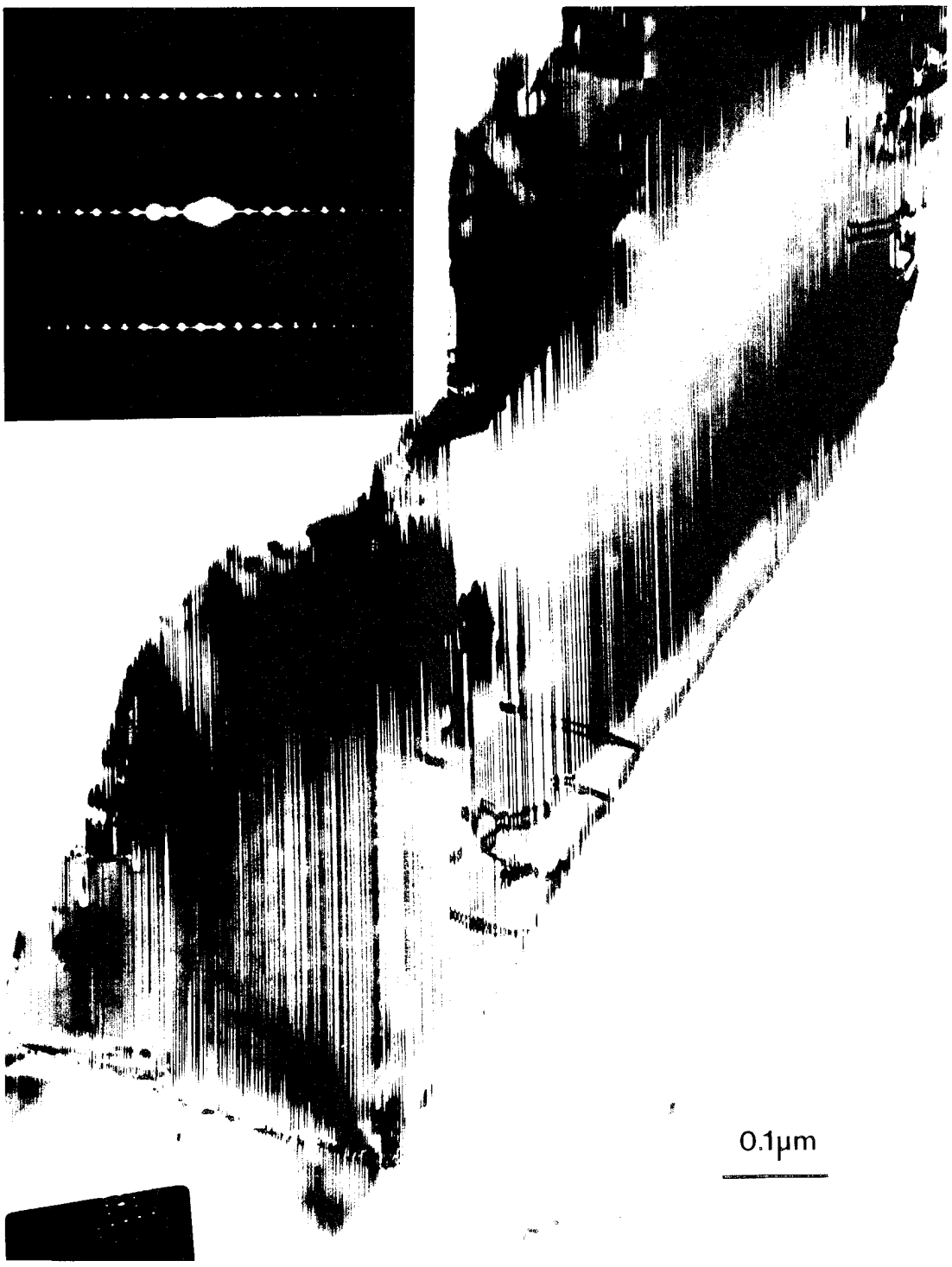

Figure 38 Enlargement of Figure 37, note the inset diffraction pattern showing a deviation in the 1/3 periodicity of spots parallel to c*.

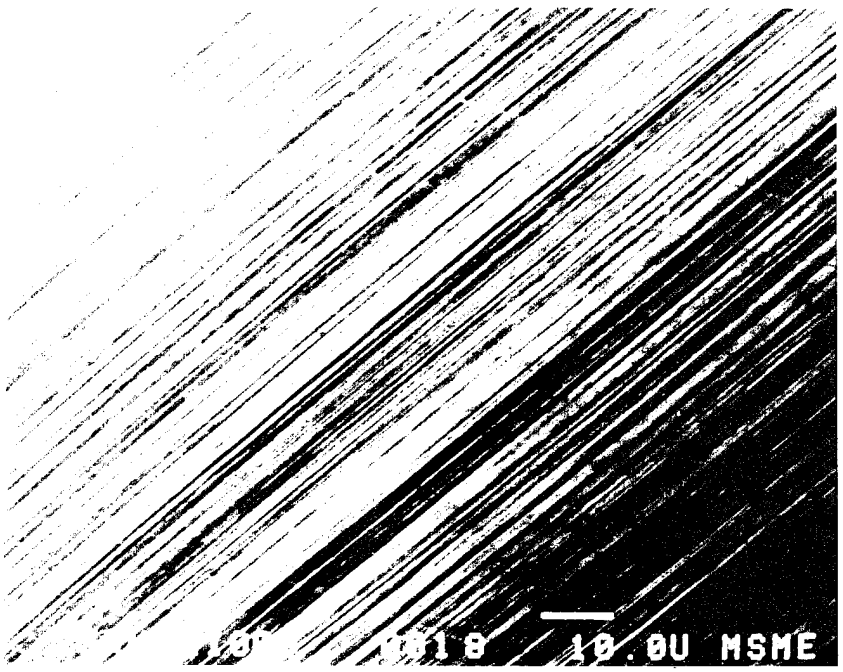

(a)

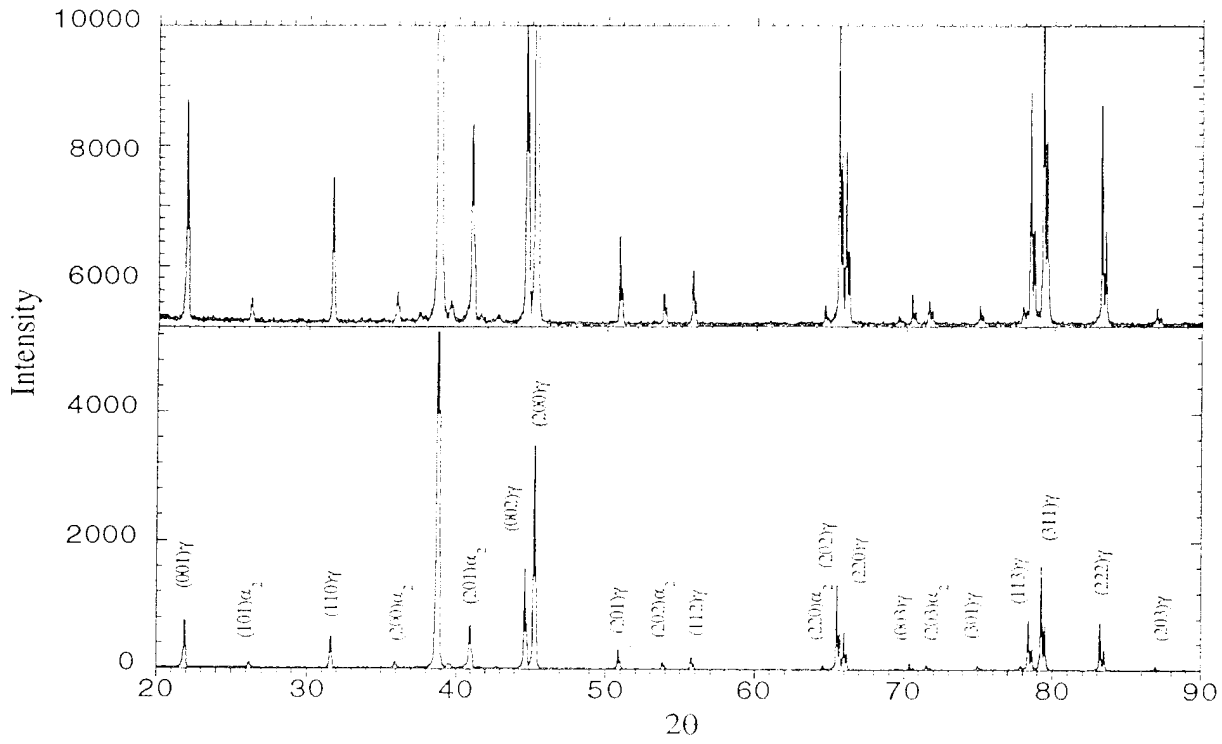

(b)

Figure 39 Microstructure following degassing at 900°C in vacuum for 72 hrs for fully transformed lamellar structure charged at 7 MPa, (a) and corresponding X-ray spectrum (b).

(a)

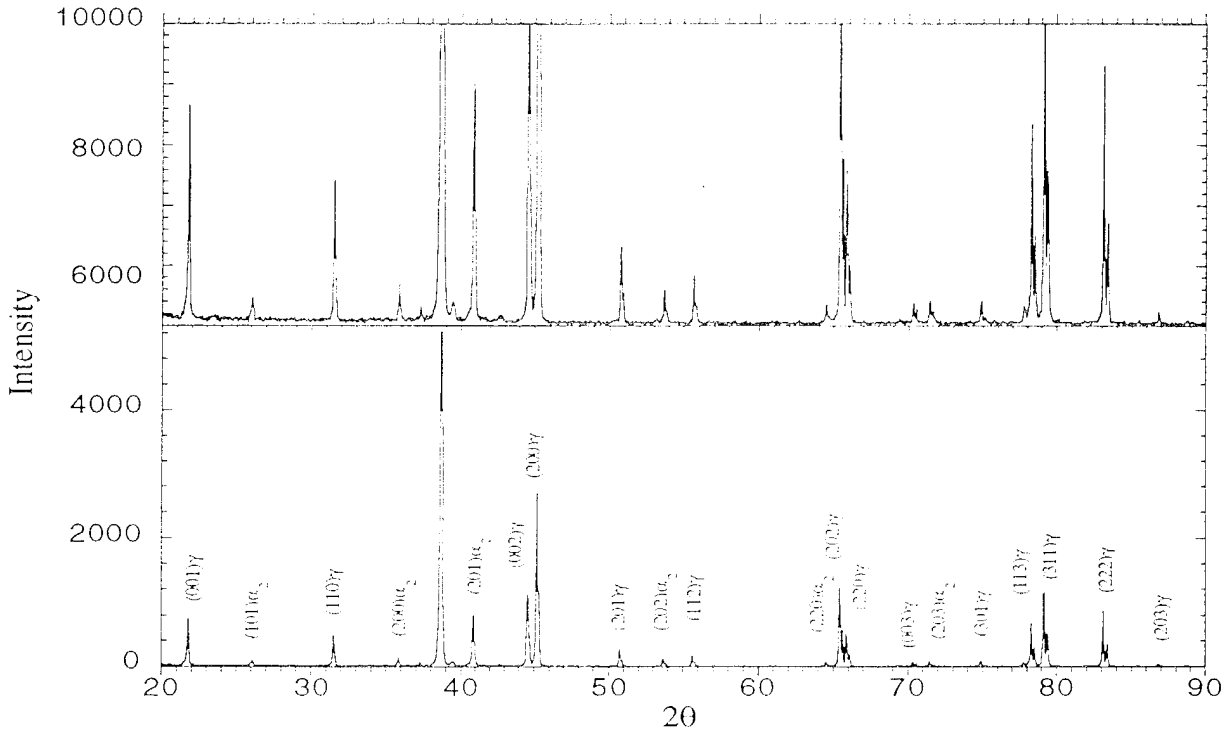

(b)

Figure 40 Microstructure following degassing at 900°C in vacuum for 72 hrs for fully transformed lamellar structure charged at 13.8 MPa, (a) and corresponding X-ray spectrum (b).

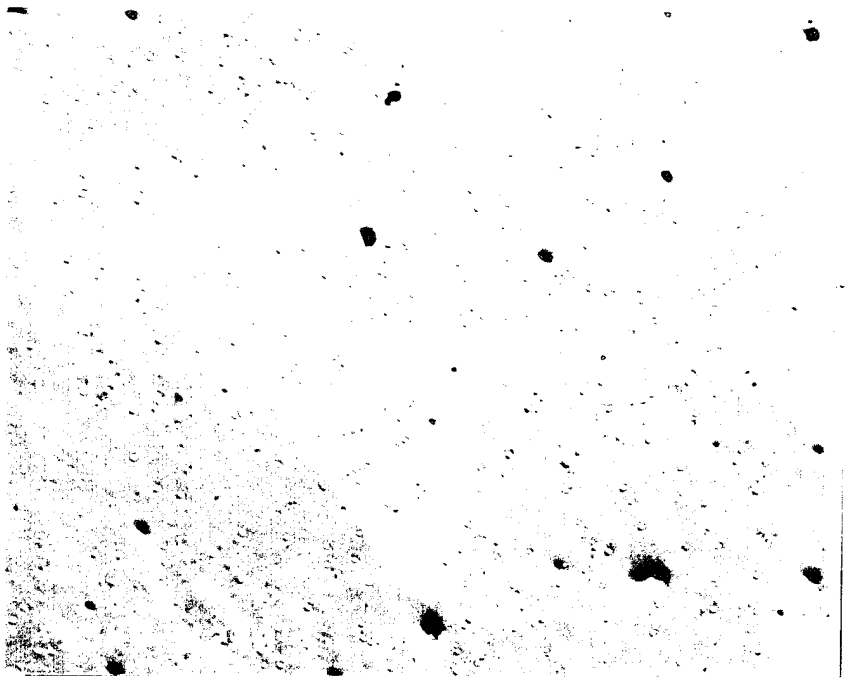

(a)

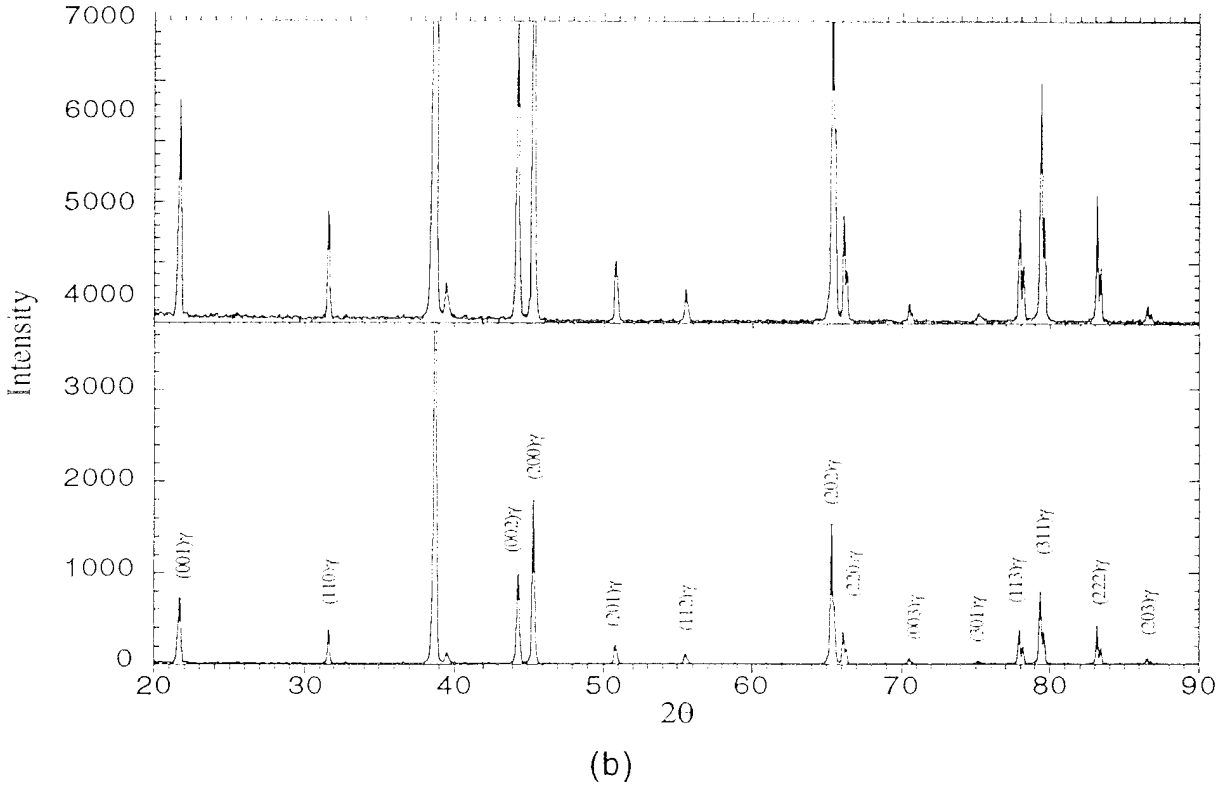

(b)

Figur 41 Microstructure following degassing at 900°C in vacuum for 72 hrs for single phase γ Ti-52Al charged at 13.8 MPa, (a); Corresponding X-ray spectrum (b).

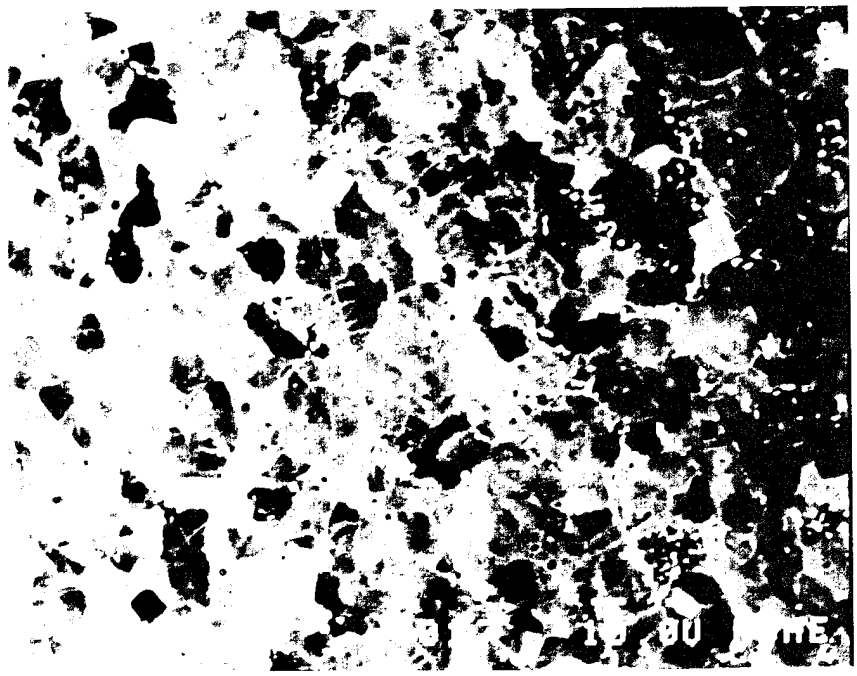

(a)

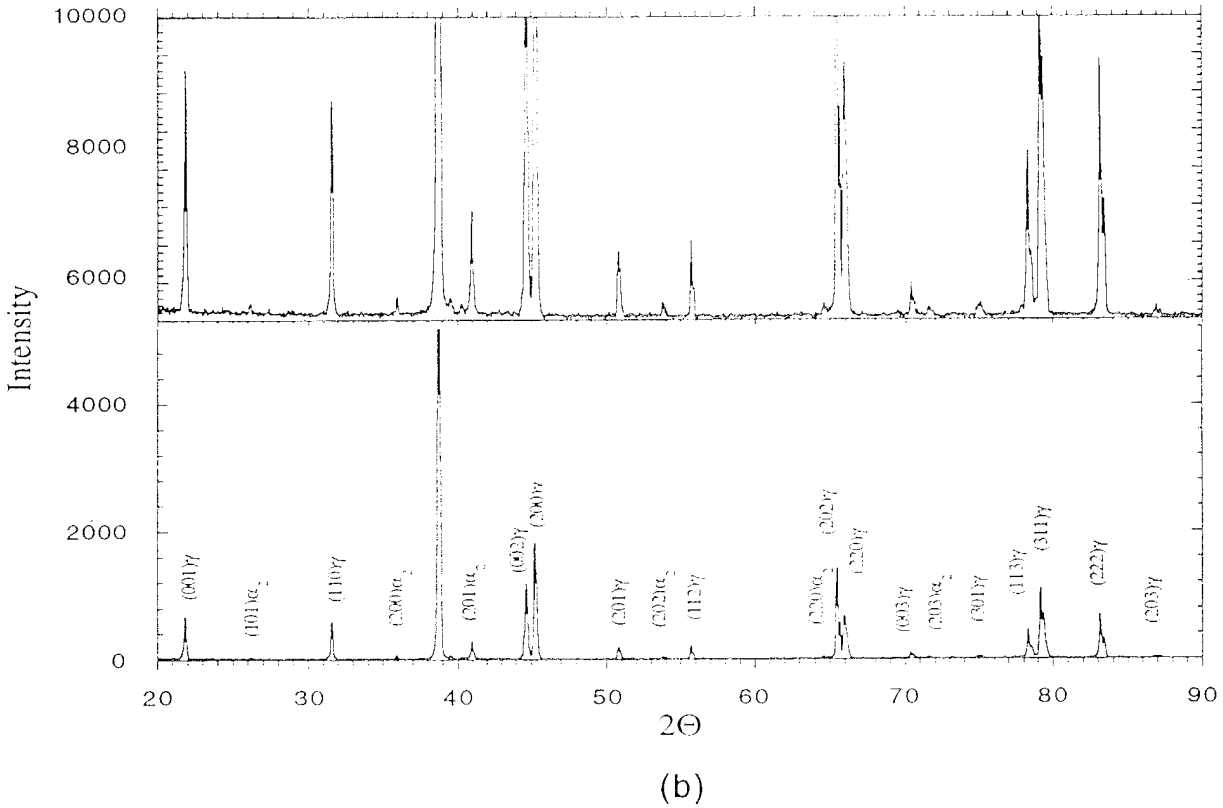

(b)

Figure 42 Microstructure following degassing at 900°C in vacuum for 72 hrs for duplex 48-2-2 charged at 13.8 MPa, (a) and corresponding X-ray spectrum, (b).

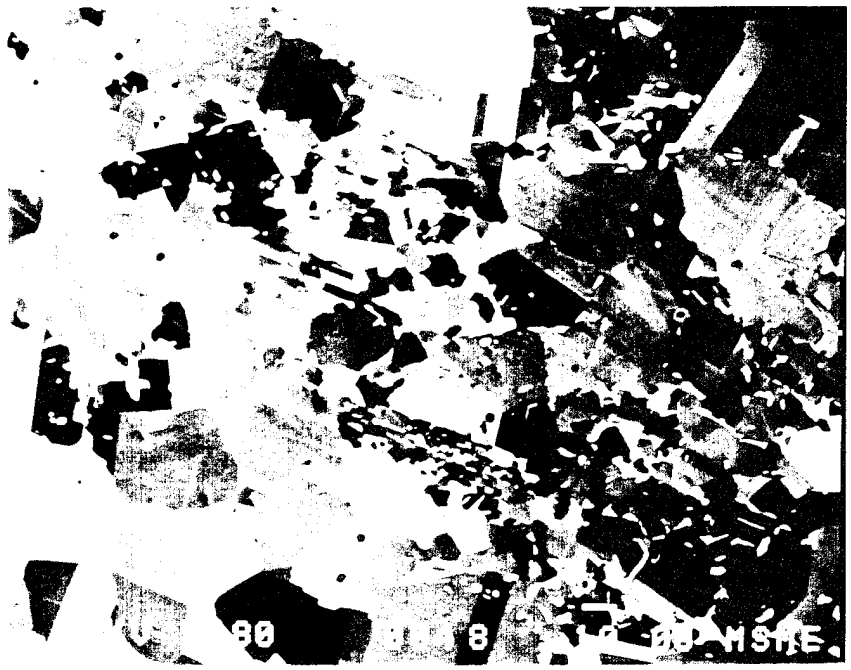

(a)

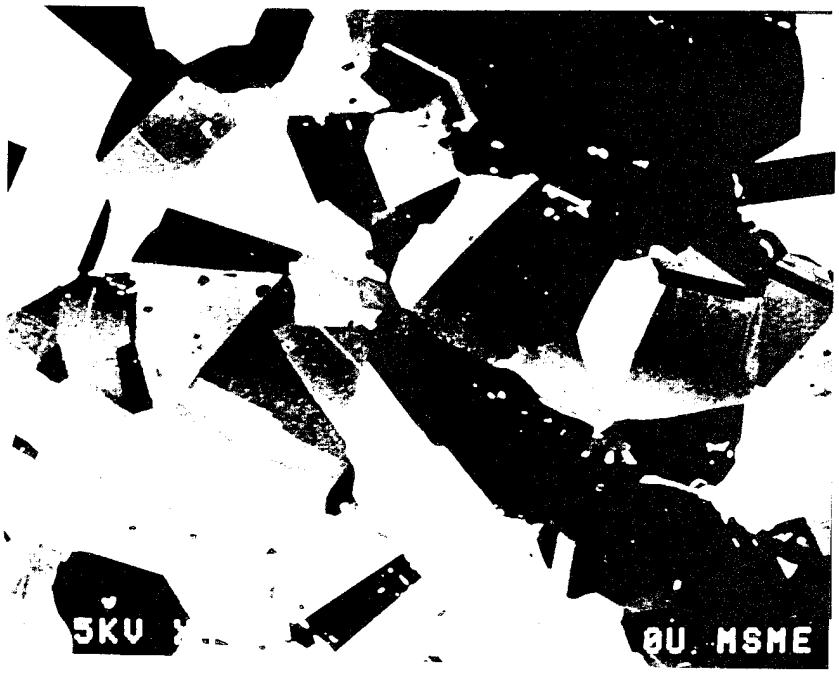

(b)

Figure 43 Microstructure following degassing at 1050°C in vacuum for 72 hrs for duplex 48-2-2 charged at 13.8 MPa showed an inhomogeneous microstructure, (a) and (b).

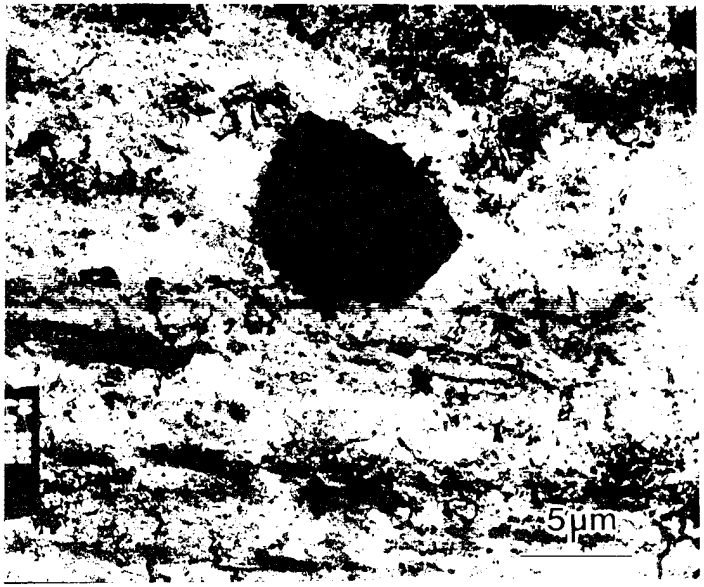

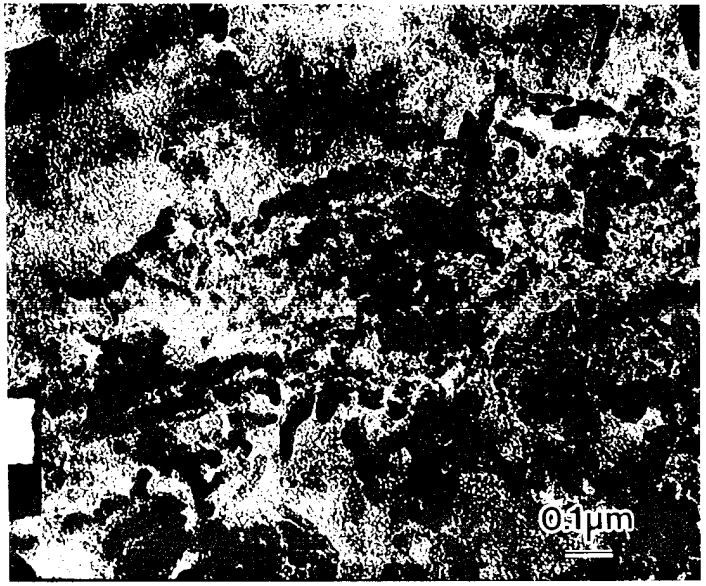

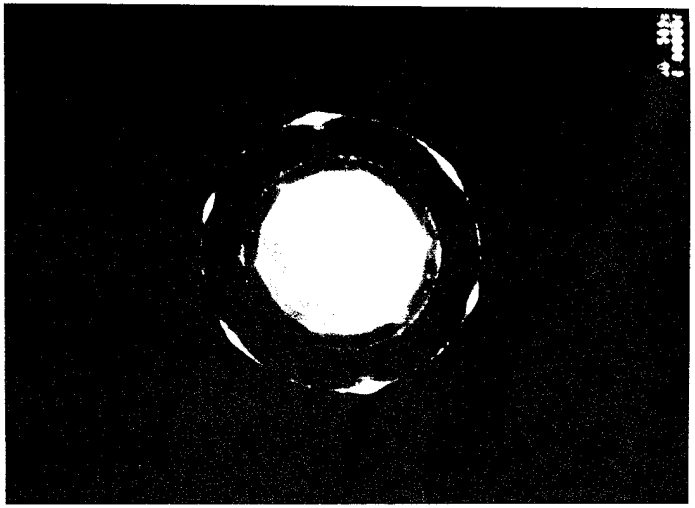

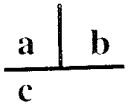

Figure 44

TEM bright field image of surface duplex 48-2-2 charged at 0.1MPa and 740°C revealing large and dispersed Al_2O_3 particles, (a): dispersed particles, (b): SAD ring pattern from (b), (c) and enlargement of (b), (d).

Figure 44 (d)

(a)

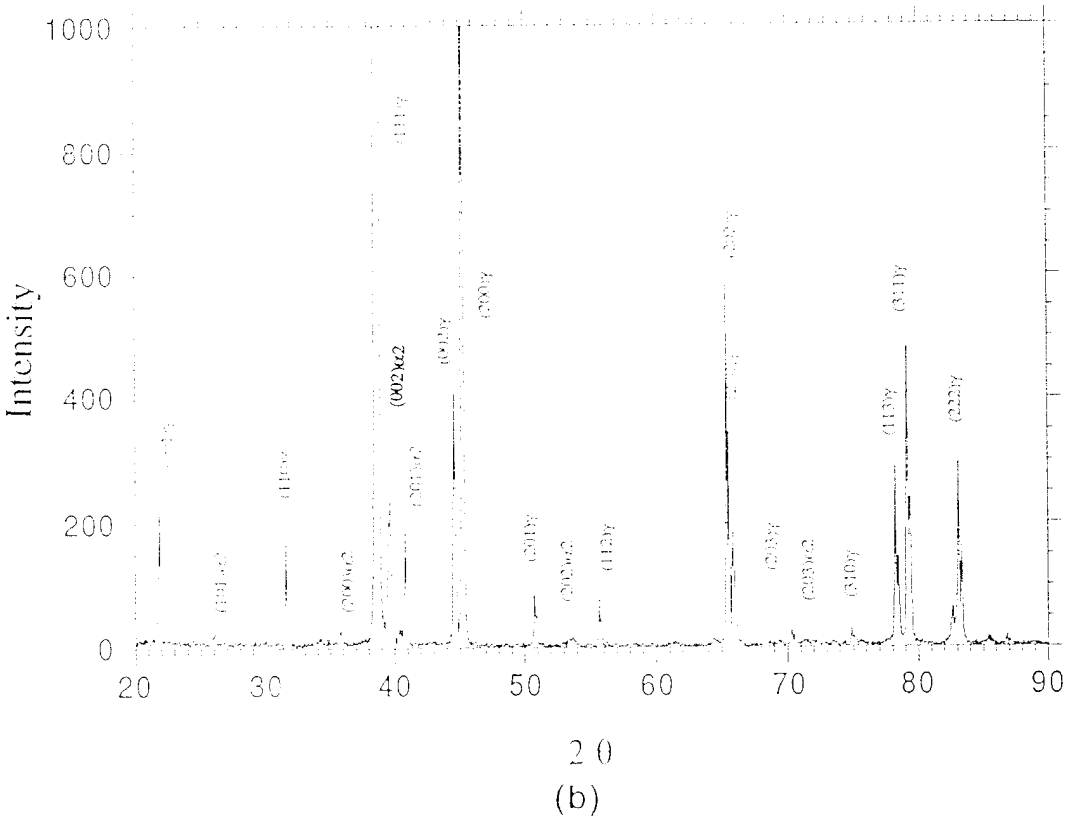

(b)

Figure 45 Cross section image for the duplex 48-2-2 following charging at 800°C and 0.1 MPa for 72 hrs. (a) and corresponding X-ray spectrum, (b).

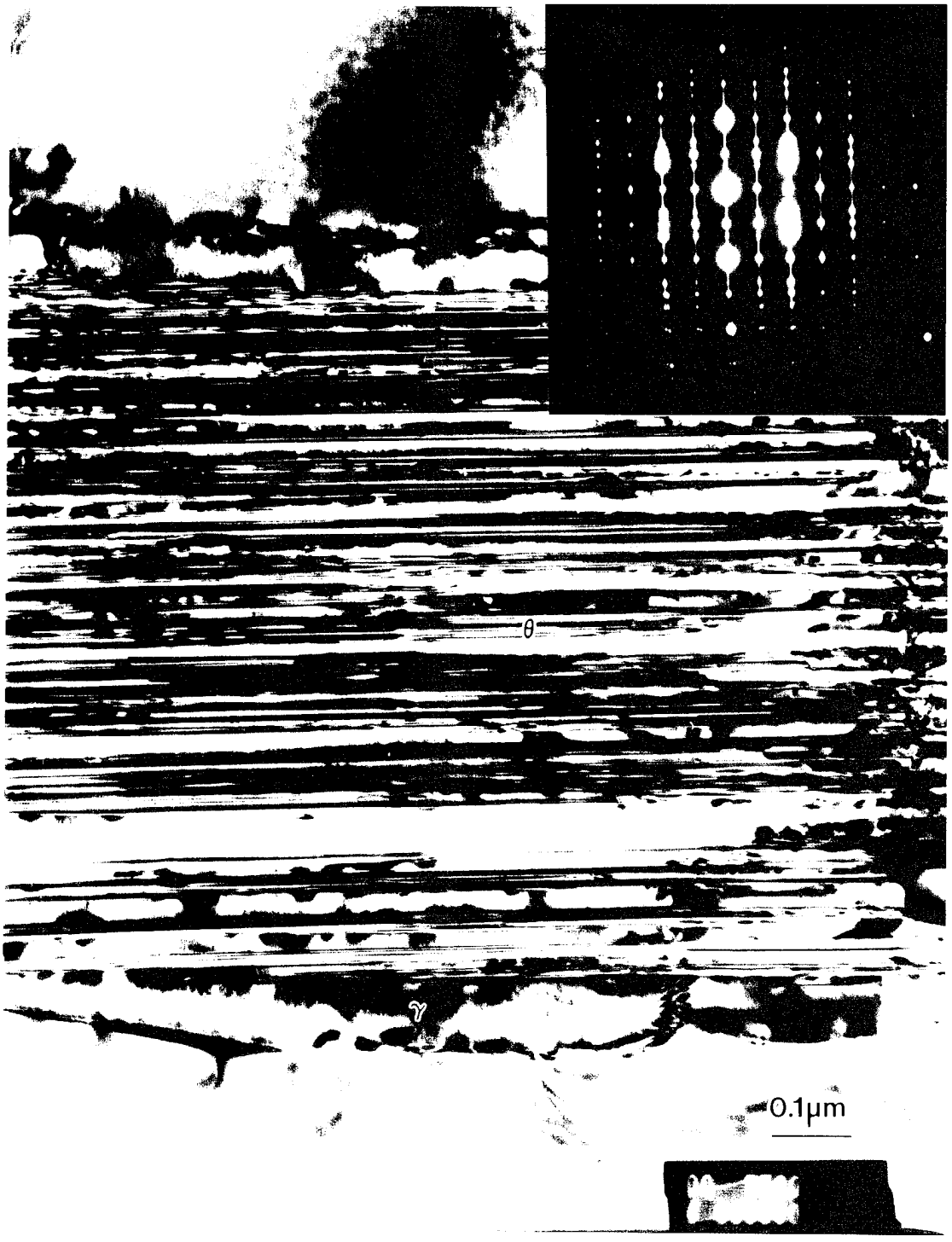

Figure 46 TEM bright field images from surface duplex 48-2-2 charged at 0.1MPa and 740°C, showing θ precipitates in α_2 laths of a lamellar colony, (a) and θ hydrides plus tiny precipitates in the γ lath (indicated by arrow), (b).

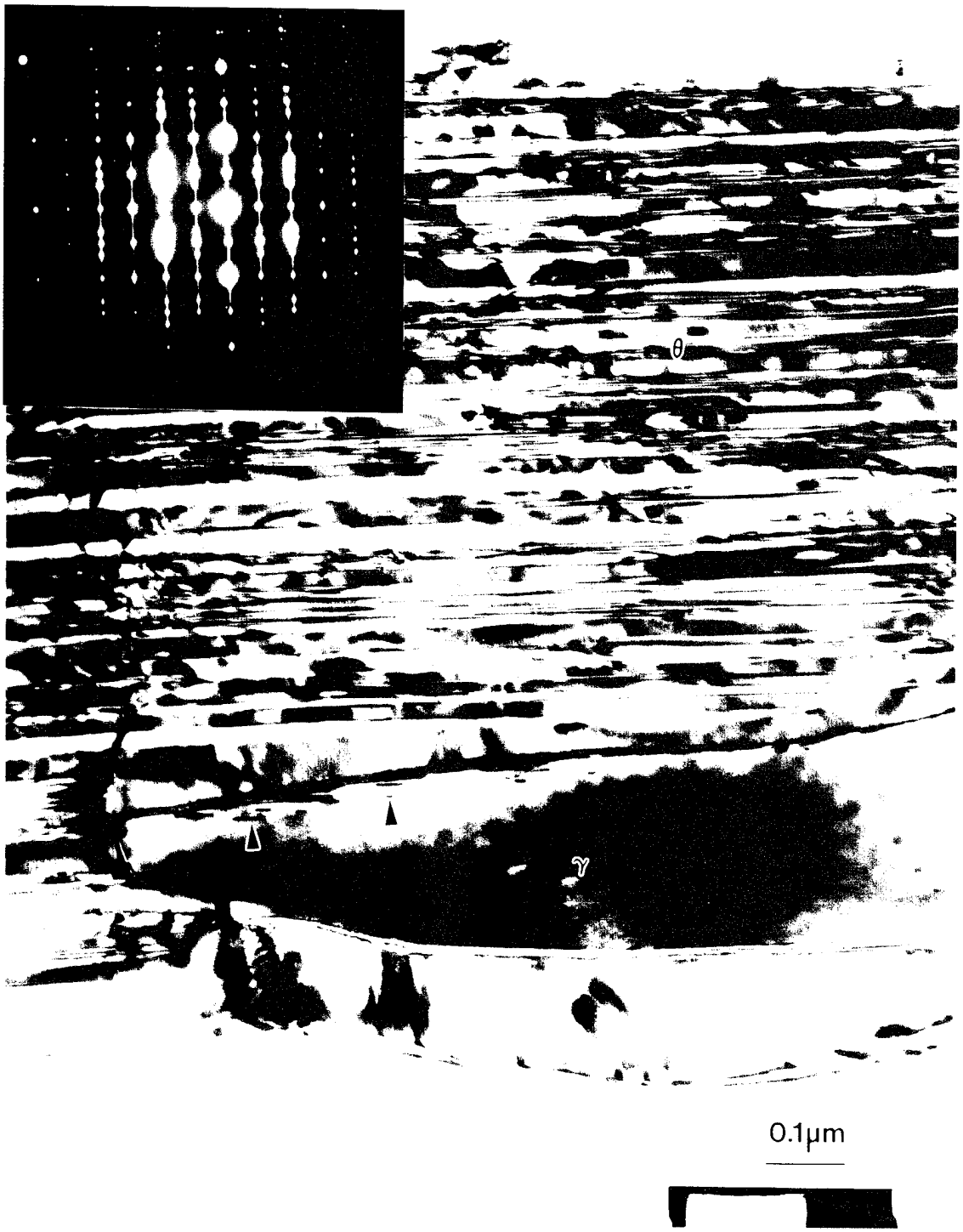

Figure 46 (b)

Figure 47 TEM BF image of surface duplex 48-2-2 charged at 0.1 MPa showing FCC hydrides in the γ phase region.

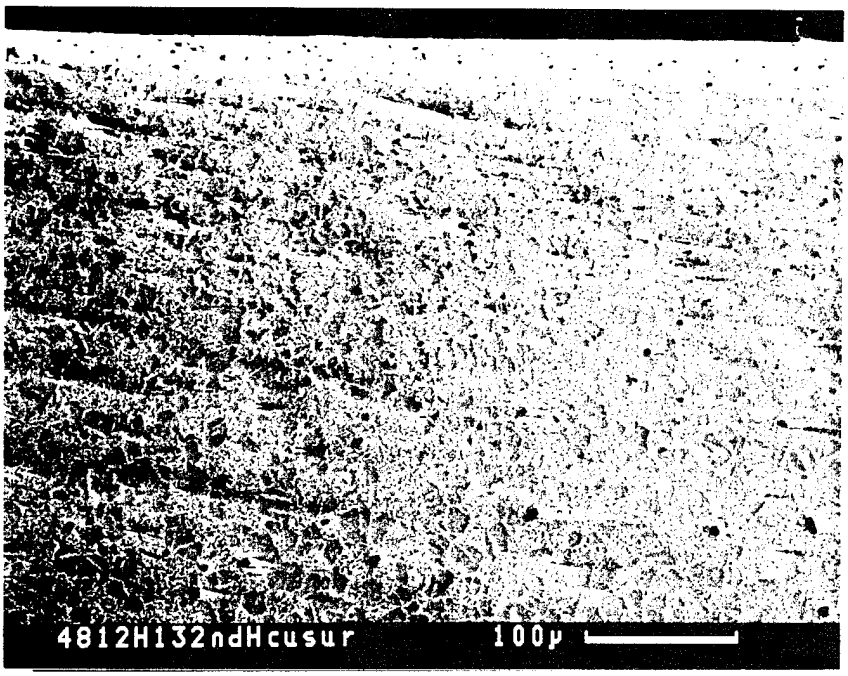

(a)

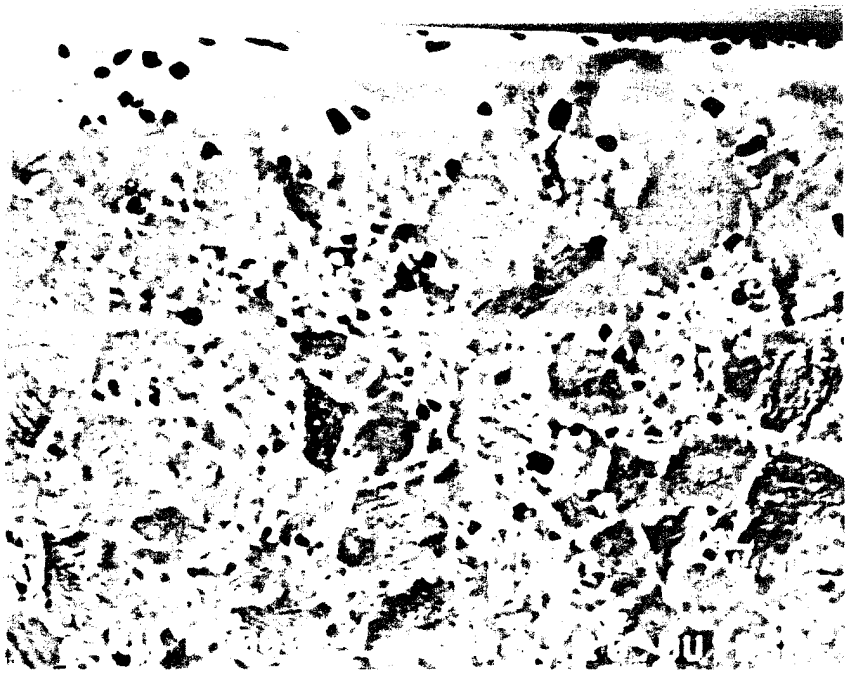

(b)

Figur 48 Cross section view of microstructure following charging at 800°C and 13.8 MPa for duplex 48-2-2 (back scattered image), lower magnification, (a) and higer magnification, (b).

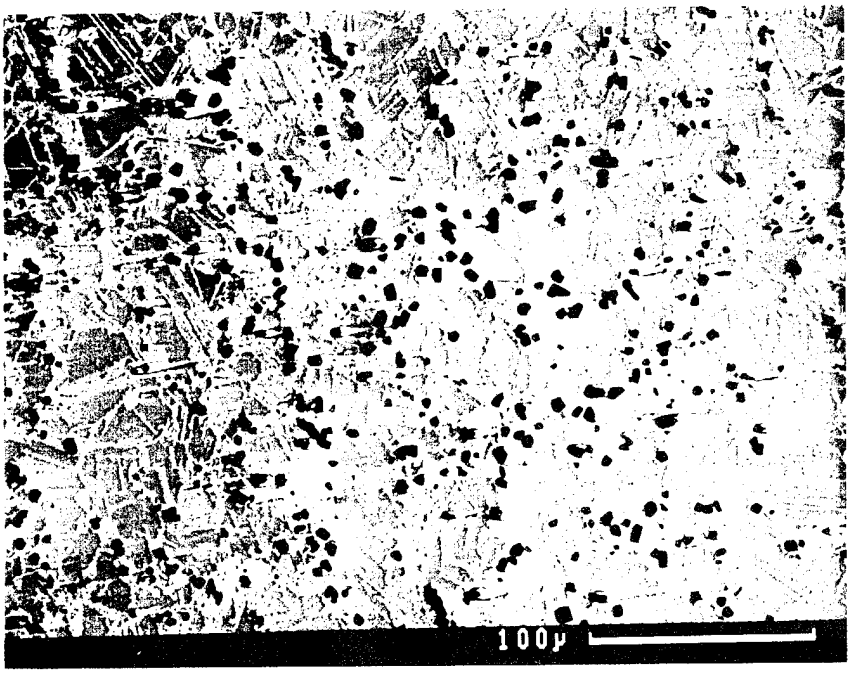

(a)

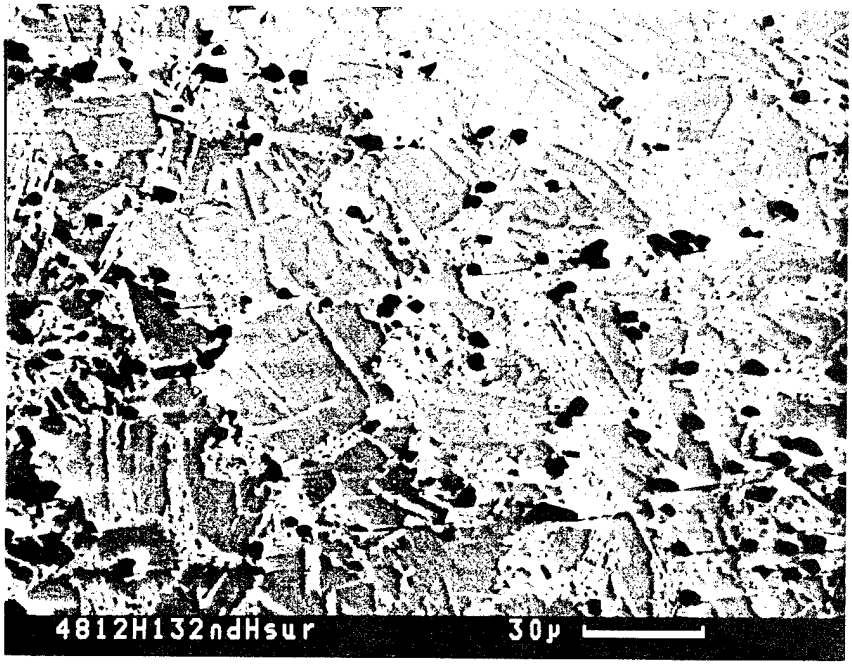

(b)

Figure 49 Surface layer view of microstructure following charging at 800°C and 13.8 MPa for duplex 48-2-2 (back scattered image) showing inhomogeneous distribution of hydride particles and Al_2O_3 particles, lower magnification, (a) and higer magnification, (b).

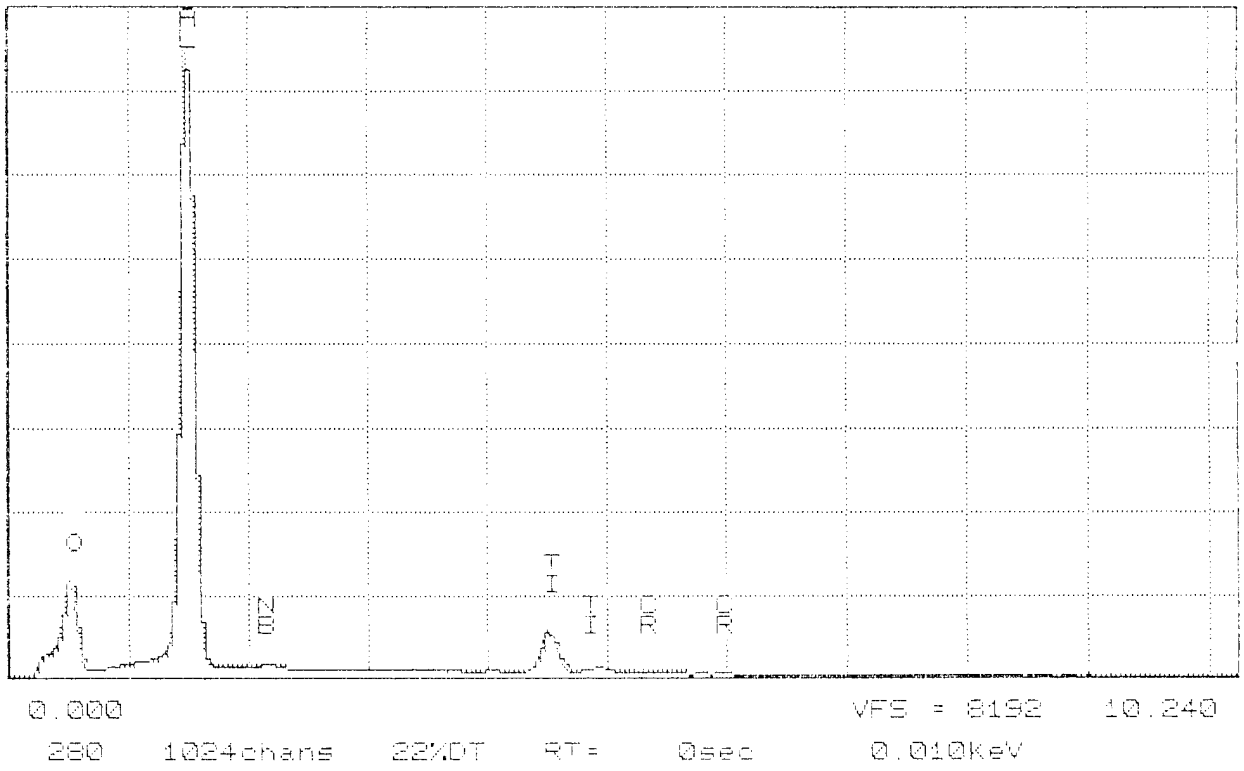

Figure 50 Energy dispersive spectrum of a big particle in the surface of duplex 48-2-2 charged at 13.8MPa and 800°C.

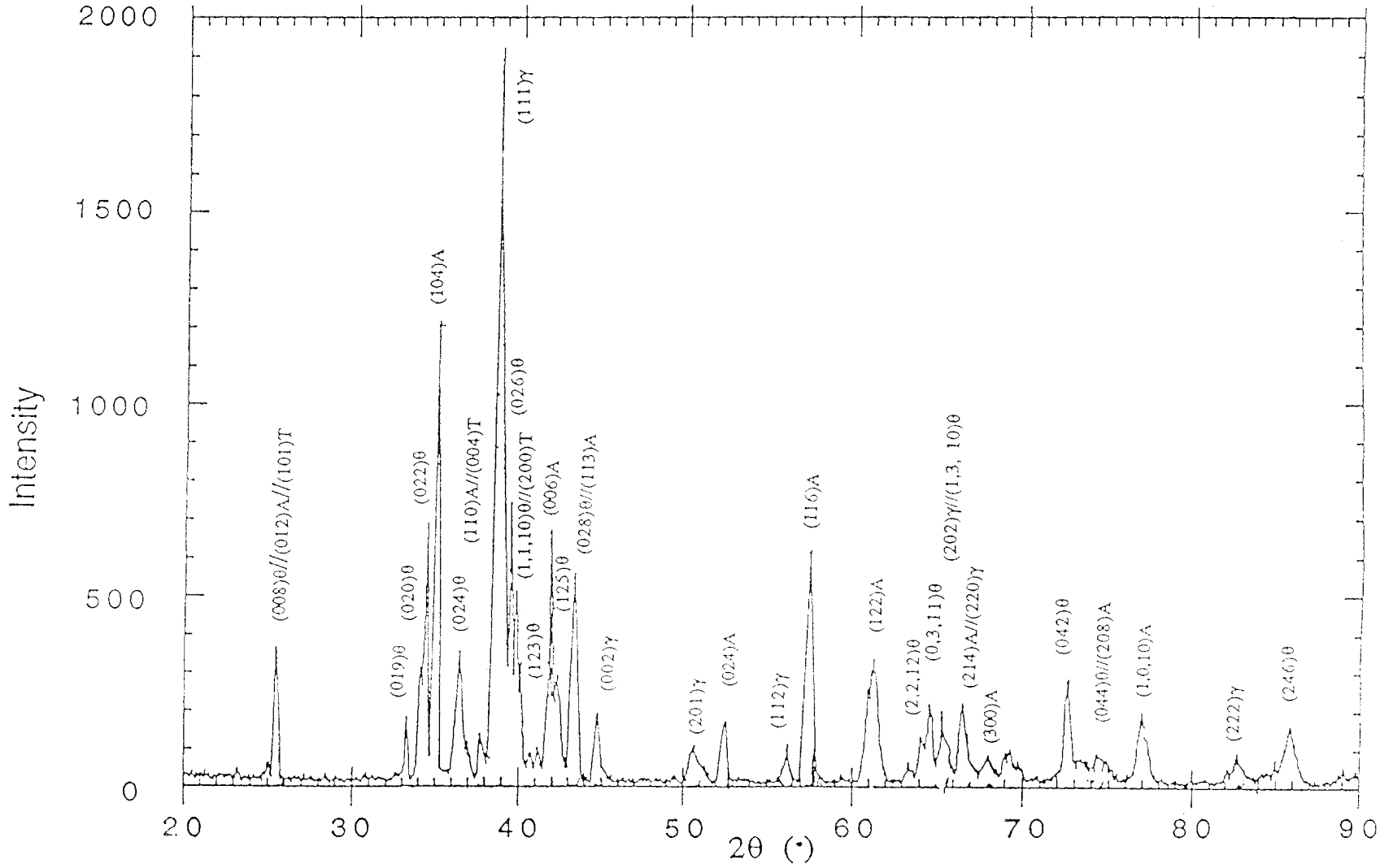

Figure 51 X-ray spectrum of surface duplex 48-2-2 charged at 13.8MPa and 800°C, consisting of four phases: tetragonal hydride (θ), γ phase (γ), Al_2O_3 (A) and TiO_2 (T).

Figure 52 TEM bright field image of surface duplex 48-2-2 charged at 13.8MPa and 800°C, revealing large and dispersed Al_2O_3 (A) particles. θ hydrides (θ) embedded in the γ matrix.

Note by comparison of Figures 51 and 17(b), that at the surface the X-ray intensities of θ phase are higher and γ phase are relatively lower, compared to the bulk material. Surface bright field images also showed that big polygonal shaped particles (marked A) were associated with θ hydrides and embedded in the θ matrix, Figure 52. The volume fraction of the θ phase at the surface is much higher compared to the bulk.

3.4 The Influence of Hydrogen on Mechanical Properties

Deformation experiments were conducted primarily on cast duplex 48-2-2 material. To measure the degree to which ductility is affected by hydrogen, uniaxial tension tests were conducted following gas phase charging at 500°C charging with a pressure of 0.1 MPa. Because of the brittleness of the material charged at 13.8 MPa, only uniaxial compression experiments were possible. Details of both sets of experiments are given below.

For tension tests, the machined cylindrical tensile specimens were electropolished then exposed to 0.1 MPa (1 atm) hydrogen at 500°C in the Sieverts apparatus for 72 hrs. The hydrogen uptake was determined to 315 wppm at this temperature. No visible changes in the electropolished surface were apparent following charging and no hydrides were observed under these charging conditions, so these experiments presumably measure the effect of hydrogen in solution on mechanical properties. To compare the degree of ductility reduction in air vs. hydrogen, some tensile samples were also exposed to an air annealing treatment of 72 hrs at 500°C in a box furnace. Following air exposures, the sample surfaces were gold-tinted in apperance. To evaluate the effect of exposure to elevated temperature only, additional specimens were subjected for 72 hrs to a temperature of 500°C under a dynamic vacuum 2×10^{-7} torr.

The results of these tension tests are summarized below in Table IX. From these results in can be seen that yield strengths are not significantly influenced by the hydrogen or air exposures at 500°C. The vacuum exposures appear to lower the yield strength and increase ductility, but it is unclear whether this is a significant result, given the inherent variability of the cast microstructure. Both the hydrogen and the air exposures result in a reduction in ductility.

Table IX - The Influence of 500°C Exposures on the Tensile Properties

500°C Exposure Environment	0.2 % Y.S. (MPa)	UTS (MPa)	Tensile Elongation (%)
None	360	490	2.7
None	365	450	1.6
Vacuum	320	430	2.2
Vacuum	340	490	3.5
0.1 MPa Hydrogen	350	420	1.0
0.1 MPa Hydrogen	360	395	0.5
Air	360	370	0.6
Air	330	420	1.1

Tensile fracture surfaces of above samples are shown in Figure 53. For the unexposed (as heat-treated) sample, low magnification views of the fracture surface shows translamellar cracking of the lamellar regions and transgranular cracking in the γ regions, Figures 53(a). In this material it was not possible to conclusively locate the fracture origins. Higher magnification views of translamellar cracking, Figure 53(b), is shown. Fracture surfaces

of the vacuum-exposed materials were not significantly different from the non-exposed fracture surfaces shown in Figure 53.

Hydrogen-charged Ti-48Al-2Cr-2Nb reveals mainly translamellar cracking (Figure 54) and also does not differ significantly from the uncharged material. The air-exposed alloy shows also translamellar fracture, but there is an increased incidence of "fluted" or cleavage-like "river patterns" (Figure 55). This may be due to a locally higher proportion of gamma grains. Again, in these samples it is not possible to identify crack initiation sites or the propagation directions of the crack due to the high proportion of the lamellar structure.

Investigations of the polished specimen surfaces just adjacent to the fracture surfaces reveal deformation bands and secondary cracking near the main crack in the unexposed material (Figure 56). These slip or twin bands exist in the γ grains, but extend also across the α_2 lamellae in the $\gamma - \alpha_2$ structure. In the heat treated, the hydrogen-charged and the vacuum-exposed conditions, secondary cracks are formed along α_2 interfaces, either along lamellar interfaces or along grain boundaries. Cracks form perpendicular, parallel or at angles to the test direction depending on the microstructural orientation. The air-exposed condition reveals a very different behavior compared to the unexposed, and vacuum or hydrogen exposed samples, Figures 56(a) - (d). A high density of microcracks are apparent on the surface just below the fracture plane. They appear to be preferentially present in regions containing a higher proportion of α_2, but also extend across gamma grains in some regions.

The influence of the high pressure charging on mechanical properties was far more dramatic, compared to the lower pressures. As mentioned earlier, tension tests were not possible due to the brittle nature of the charged material. However, compression tests were

possible on samples which were machined to shape prior to charging at 7 MPa and 13.8 MPa. Room temperature compressive stress-strain curves for charged and uncharged specimens are shown in Figure 57. The deformation characteristics of the charged and uncharged specimens differed significantly. The 0.2% yield strength in compression increased from 440 MPa for the uncharged specimens to 735 and 740 MPa for the specimens charged at 7 and 13.8 MPa, respectively. Compressive yield strengths are apparently higher than in tension due to the orientation of the compression specimen axis along the short transverse direction of the slab, whereas the tension specimens were oriented longitudinal direction. Work hardening rates at 1 % plastic deformation were 7.3 GPa/unit strain in the uncharged condition, 7.7 GPa/unit strain after charging at 7 MPa and 9.0 GPa/unit strain after charging at 13.8 MPa. For plastic strains up to 2%, work hardening rates decreased with increasing strain for all conditions. For higher strains the hardening rate saturated at 4.5 GPa/unit strain in the uncharged Ti-48Al-2Cr-2Nb, at 4.8 GPa/unit strain after charging at 7 MPa and at 5.0 GPa/unit strain after charging at 13.8 MPa.

To further examine the influence of hydrogen on the rate sensitivity of the material, strain rate change experiments were also conducted. Repeated changes between strain rates of $2x10^{-4}$ s^{-1} and $2x10^{-2}$ s^{-1} demonstrated a pronounced rate sensitivity of both the charged and uncharged materials. The strain rate sensitivity $m = \delta \ln\sigma / \delta \ln\dot{\varepsilon}$ at 1% plastic strain was 0.012 for the uncharged material, 0.009 for the material charged at 7 MPa and 0.007 for the material charged at 13.8 MPa. For all charged and uncharged conditions, there was a similar decrease in the level of the rate sensitivity with increasing stress to values leveling around 0.004 for the highest plastic deformation examined.

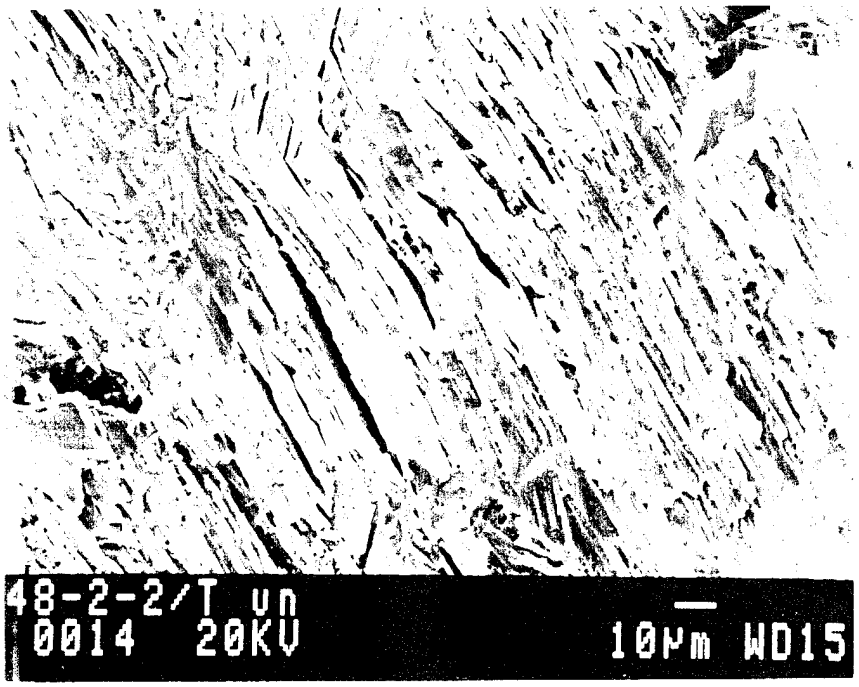

(a)

(b)

Figure 53 - Fracture surfaces of unexposed duplex 48-2-2 following tension testing.

Figure 54 - Fracture surface of tension specimen pre-exposed to hydrogen.

Figure 55 - Fracture surface of tension specimen pre-exposed to air.

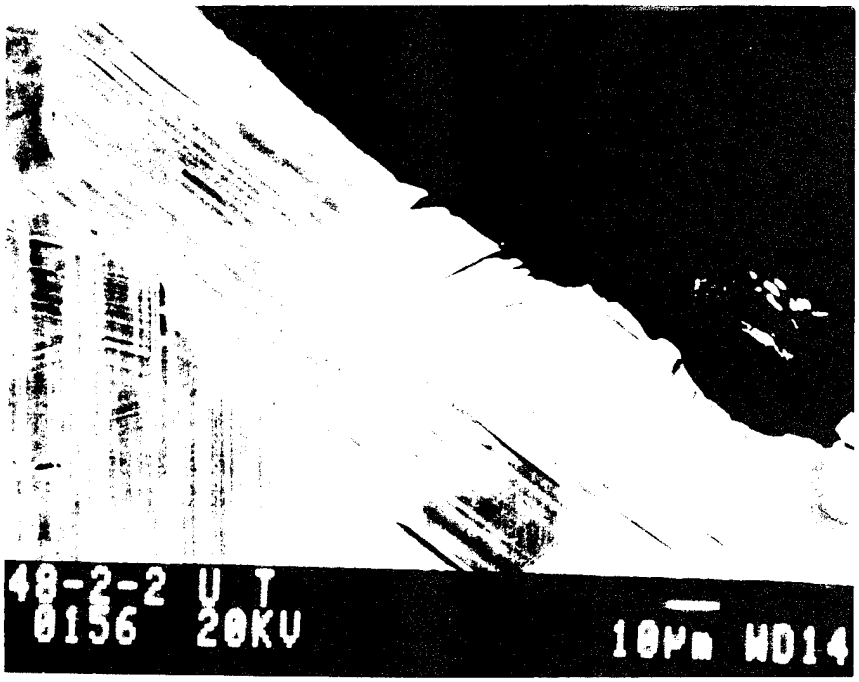

Figure 56(a) - Surface of tension sample, just below fracture plane for unexposed sample.

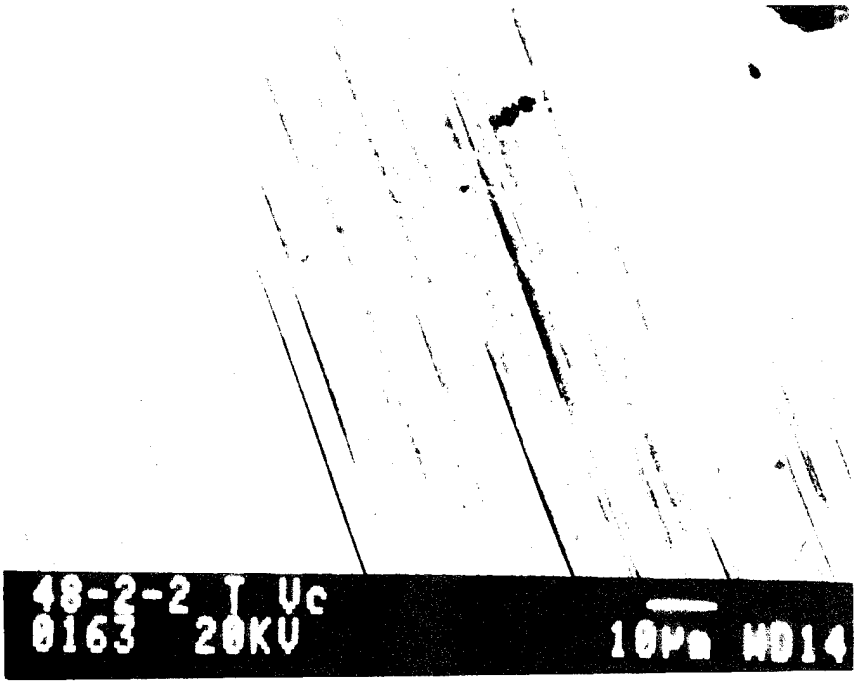

Figure 56(b) - Surface of tension sample, just below fracture plane for vacuum sample.

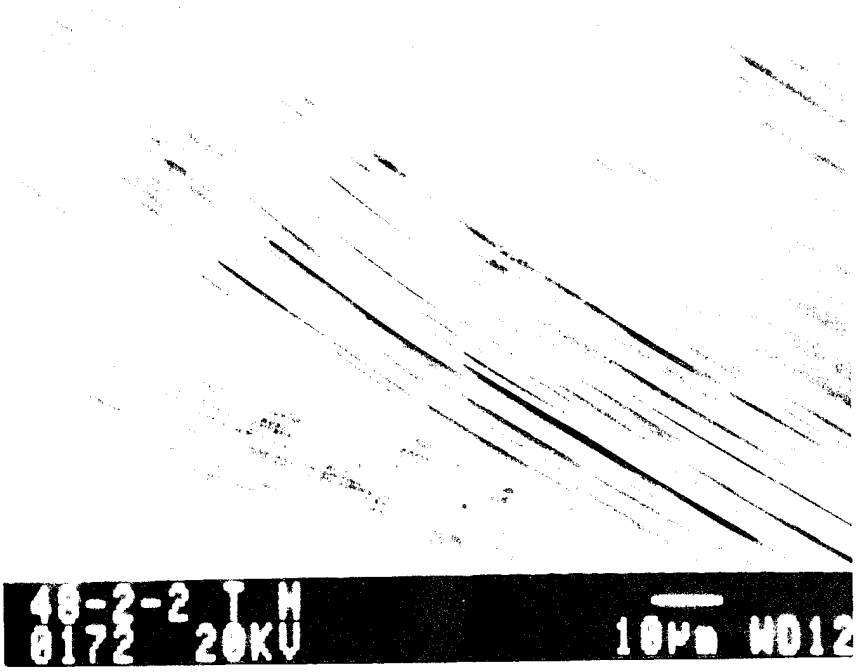

Figure 56(c) - Surface of tension sample just below fracture plane for hydrogen-exposed sample.

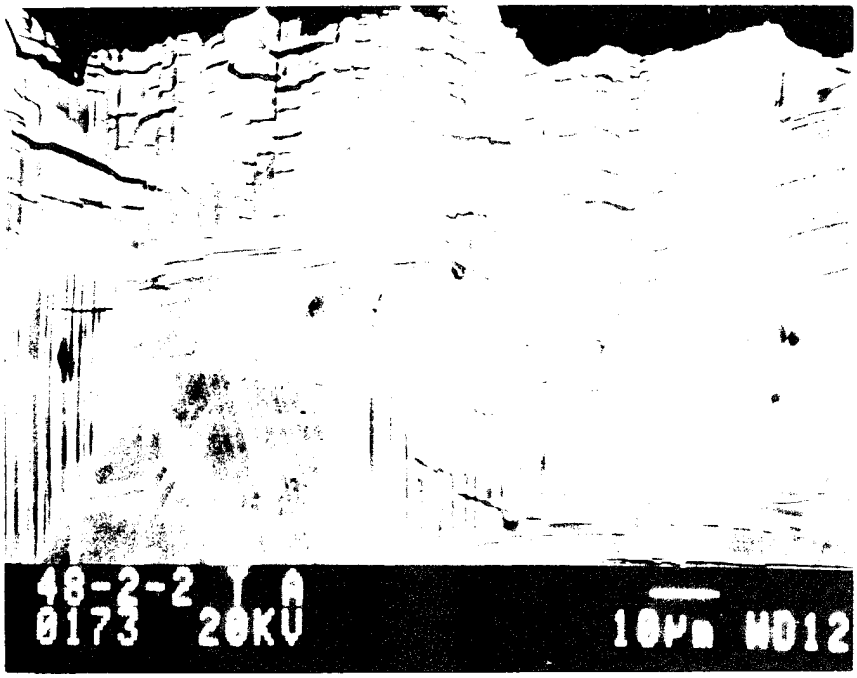

Figure 56 (d) - Surface of tension sample, just below fracture plane for air-exposed sample.

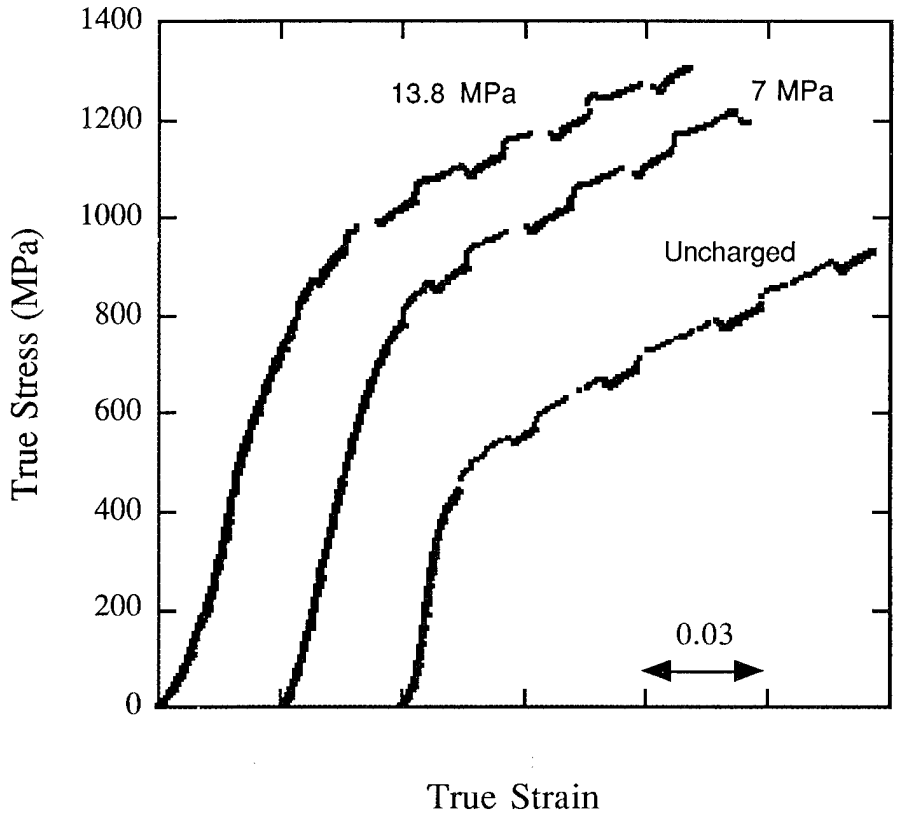

Figure 57 - Results of strain rate change experiments, strain rates 2 x 10^{-4} s^{-1} and 2 x 10^{-2} s^{-1}, sample axis parallel to short transverse of cast slab.

3.5 Discussion

3.5.1 Hydrogen - Microstructure Interactions

Over the range of charging conditions utilized in this study, two phase γ - α_2 alloys had higher hydrogen uptakes compared to the single phase γ alloys. Furthermore, with a charging pressure of 0.1 MPa, the hydrogen uptake was highest at the lowest charging temperature of 500°C. These observations suggest that the α_2 phase dominates the behavior of these materials with regard to hydrogen uptake, and are consistent with the response of a number of other studies on α_2, γ - α_2 and γ alloys [4 - 18]. In two phase γ - α_2 alloys, the hydrogen apparently strongly partitions to the α_2, and this must be

accounted for in the estimation of the hydrogen content of the hydride phases, as will be discussed further below.

Agreement on the microstructural response of gamma-based titanium aluminides to charging at relatively low pressures is beginning to emerge. At pressures of 0.1 MPa, hydrogen is maintained in solution (except in impurity affected near-surface regions) with no hydride formation in either single phase γ alloys or γ - α_2 alloys. Because of the higher solubility of hydrogen in the α_2 phase, the total hydrogen uptake is sensitive to the α_2 proportion, and thus to alloy composition and heat treatment. The only report to the contrary is that of Chu and Thompson [19], who found much higher hydrogen uptakes compared to all other studies and reported the presence of hydrides following 0.1MPa charging. In the Chu study, hydrogen uptake was inferred by measurements of weight gains during charging. In the present study, we have determined that this is an unreliable technique for determining hydrogen content, due to the high affinity of the alloys for trace amounts of oxygen and other interstitials that may be present in a dynamic vacuum environment. The availability of small quantities of these species results in series of complex reactions with oxide formation that apparently enhances hydride formation, but only in the near-surface regions. The results of Chu [19] were affected by these surface phenomena, and the "extra" peaks in their X-ray spectra following charging can be attributed to the presence of alumina.

It is presently unclear to what degree the surface oxide layers inhibit hydrogen permeation into the material. Permeation studies on α_2-base alloys have demonstrated the inhibiting nature of the surface films on hydrogen permeation, particularly at temperatures below 600 °C [20]. The effectiveness of the surface layer as a barrier to hydrogen transport depends on its thickness, since titanium and its alloys have the ability to dissolve species such as C and O. Thus the thickness of the surface layer will depend on a balance between the

competing processes of layer formation and layer dissolution, which in turn will depend on temperature and pressure. The process of dissolution of the impurities species into the alloy is governed by the diffusion characteristics of the alloy for the species O, N and C. Since diffusion is a thermally activated process, it is significantly more effective at higher temperatures. Thus, above some critical temperature the barrier growth rate is presumably slower than the dissolution rate and the layer thickness is reduced. For the α_2-base alloy Ti-24 Al-11 Nb alloy, the critical temperature at which the hydrogen transport mechanism converts from surface to diffusion control is approximately 650 ℃ [20]. No systematic parallel studies have been conducted for γ-TiAl base alloys. However, the surfaces of duplex 48-2-2 charged at 13.8 MPa were clearly composed of a two-layer structure: a TiO_2 outer layer and an Al_2O_3 inner layer. In this situation the θ hydrides were associated with the discontinuous alumina layer. It is thus unlikely that these mixed oxide layers inhibited diffusion of hydrogen into the material in these experiments. At lower pressures there were also no indications of a continuous Al_2O_3 layer. Here, hydrides were also observed in the surface of 48-2-2 charged at 0.1 MPa, but not in the interior of the samples, futher suggesting that mixed oxide layers promote hydride formation. Additionally, in the study by Gao et. al. [17], a sample which was subject to pre-oxidation at 800°C still achieved the equilibrium (higher) concentration of hydrogen upon subsequent charging at 550°C. Further detailed studies of the operative surface transport processes would clearly be useful.

With regard to high pressure charging, to date no consistent observations have emerged regarding hydride formation in single phase γ alloys or γ-base alloys composed of a mixture of the γ and α_2 phases [10 - 17]. Under conditions where FCC hydrides are formed in the two alloys studied here, the γ - α_2 alloy absorbed nearly four times more hydrogen, compared to the single phase γ alloy. The FCC hydrides observed here in the Ti-52Al and lamellar and duplex Ti-48Al-2Cr-2Nb alloys are similar to those observed by

Legzdina et. al. [2] in Ti-52Al and Ti-48.6Al-2Nb-0.2Ta single phase and duplex structures, respectively. Following charging at 650°C and 13.8 MPa they observed hydrogen concentrations of 2600 wppm and 11,000 wppm, respectively, for the single phase and two phase alloys. It is interesting that the hydrogen uptakes at 13.8 MPa for the 48-2-2 and Ti-52Al alloys studied here were lower for the same hydrogen pressure, but at a higher temperature. Presumably a higher volume fraction of FCC hydrides are present at the lower charging temperature utilized by Legzdina et. al. [2].

In addition to the FCC hydrides discussed above, a number of other different ternary hydrides have been reported in γ - α_2 alloys. Following charging at 650°C and 13.8MPa, Matejczyk and Rhodes [12] observed a hexagonal phase with a = 0.517nm and c = 0.518nm in a Ti-48.6Al-2.4Cr alloy. Interestingly, the "a" lattice parameter is similar to that observed here, although a much higher volume fraction of the hydride phase was observed compared to the alloys studied here. Takasaki et al. [16] have observed a different tetragonal hydride in cathodically charged lamellar Ti-42Al; the lattice parameters for this phase have been reported as a = 0.452nm and c = 0.326nm. The general morphology and the presence of faults in the tetragonal hydride observed here is similar to that observed by Schwartz et al. [11] in a duplex Ti-48Al alloy charged at 800°C in 10.5MPa H_2, with an uptake of 2600wppm. Although the crystal structure of the hydride in the Ti-48Al alloy was not determined, the presence of a high density of faults spaced by 4 nm were observed parallel to planes which possessed a d-spacing of 0.7nm. Recent studies of Ti_3Al-base alloys have indicated that hydrogen serves to stabilize the orthorhombic phase [18]. Alternatively, Schwartz, et al. [6] reported $E2_1$ hydrides in a single α_2 phase of Ti_3Al, after charging at 700 °C with a H uptake of 2000 wppm.

Although a number of different hydrides have been reported in other studies on γ-based alloys, the lack of detailed characterization of their structure and composition make it

difficult to speculate on their relationship, if any, with the θ phase observed here. The unit cell of the θ phase is body-centered tetragonal with lattice parameters of a = 5.28 Å, c = 28.48 Å. The θ phase precipitates have both blocky and elongated shapes with sizes ranging from 0.1-0.2 μm in width by a few μm in length, similar to the morphology of the original α_2 present prior to charging. The θ transformed from the α_2 laths takes an elongated shape and the hydrides originating from grain boundary α_2 have blocky shapes. TEM observations confirm that the orientation relationship between the θ phase and α_2 or γ phases, is $(0001)\alpha_2//(111)\gamma//(001)_\theta$, $[11\bar{2}\ 0]\alpha_2//[1\bar{1}\ 0]\gamma//[100]_\theta$. With α_2 and γ volume fractions taken as 10% and 90%, respectively, in duplex 48-2-2, an estimate of the hydride stoichiometries can be obtained. For the duplex 48-2-2 a hydrogen uptake 2000 wppm is considered. Assuming the hydrogen solubility in γ phase of Ti-52 Al and duplex 48-2-2 is identical, at 640 wppm, the total hydrogen partitioned to the α_2 phase would be 1424 wppm. The hydrogen content of the former α_2 phase would then be 14,240 wppm. If the atomic ratio of Ti/Al in the θ hydride is taken as the average of 1.7, the calculated formula of the θ hydride should be $Ti_{1.7}AlH_{1.5}$. This is consistent with the equilibrium Al content of the α_2 phase at 800 °C at about 36 atomic % (Ti/Al = 1.77), based on the Ti-Al binary phase diagram. The exposure time during high-pressure charging is 60 hrs, and microstructural observations suggest that the hydrogen permeated the entire cross section of the samples in this time period. Thus, it is very likely that no long-range diffusion is required for conversion of the α_2 phase into the θ hydride.

The estimation of the stoichiometry for FCC hydrides is more difficult due to the broad range of Ti/Al atomic ratios, which varied from 1.14 to 2.19. The γ phase and FCC hydride have a cube-on-cube orientation relationship. Thus, if the FCC hydride originates from the γ phase with all the tetrahedral interstitial sites filled, its formula would be $TiAlH_4$. However, FCC hydrides were observed both in γ phase and α_2 phase. Additionally, it is

apparent that the formation of FCC hydrides initially took place in α_2 phase, with the evidence that no α_2 phase was observed in lamellar 48-2-2 charged at high pressure. TEM bright field images also revealed a similar microstructural morphology of lamellar 48-2-2 charged at 13.8 and 7 MPa, but a higher volume fraction of FCC hydrides was observed at foils charged at 13.8 MPa compared to 7 MPa. The FCC hydrides were preferentially present in the previous α_2 phase regions, while, in γ lath regions, smaller, cube shaped hydrides and small needle-shape FCC hydrides were present after charging at 13.8 MPa and 7 MPa, respectively. If the hydride has a Ti/Al ratio of 2, Ti atoms will be redundant and some of the Al sites will be vacancies. So, the FCC hydride formula will be Ti_2AlH_x. Under this situation, it appear that long-range diffusion of Ti and Al will be involved in the precipitation process, which appears to be aided by heterogeneous nucleation along boundaries and other defects. A relatively constant Ti/Al ratio (1.5) was measured from duplex 48-2-2, after the second charging at 13.8 MPa and 800 °C. BF images also revealed densely populated FCC hydrides both in equiaxed γ and lamellar regions. The hydride would have a atomic composition as $Ti_{1.5}AlH_x$.

Due to the faulted nature of the θ hydrides observed here, it was not possible to determine the atomic positions of the species that constitute the phase. However, given the diffraction information obtained, it is possible to narrow the possible space groups for the phase; the rationale for this follows. Table XI lists the main zone axes and corresponding reflections of the θ hydride as well as the general reflection conditions for space group $I\bar{4}$ 2d, $I4_1md$ and $I4_1/amd$ [21]. The three possible space groups were generated by comparing the missing spots in the SAD patterns with the International Space Group Tables. General reflection conditions were applied to identify each specific space group, since the atom arrangement in the unit cell is unknown. Comparing the conditions listed in the table to the actual diffraction patterns in general, two reflections were not consistent with the space group requirements, which are $(006)_\theta$ and $(1\bar{1}\ 0)_\theta$. It is not unusual that $(006)_\theta$ spot is

Table XI General Reflection Conditions for Space Group: I 4_1/md, I 4_1/amd and I $\bar{4}$2d.

Zone	Reflecction	hkl: h+k+l=2n	hk0: h+k=2n	0kl: k+l=2n	hhl: 2h+l=4n	00l: l=4n	h00 h=2n	h$\bar{h}$0 h=2n
[100]	(006)							
	(020)		x					
	(011)			x				
[120]	(2$\bar{1}$1)	x						
	(2$\bar{4}$0)		x					
[110]	(004)					x		
	($\bar{1}$12)	x						
[131]	($\bar{1}$01)	x						
	($\bar{1}$1$\bar{2}$)	x						
	(01$\bar{3}$)			x				
[031]	(200)						x	
	($\bar{2}$1$\bar{3}$)	x						
[111]	($\bar{1}$01)	x						
	($\bar{1}$10)							?
	(01$\bar{1}$)			x				
[551]	($\bar{1}$05)	x						
	(01$\bar{5}$)	x						
[001]	(100)						?	

inconsistent with the requirement, since $(006)_\theta$ spot is parallel to $(0001)\alpha_2$, and the $(0001)\alpha_2$ spot was always observed in $[11\bar{2}\,0]\alpha_2$ pattern due to double diffraction. All $(1\bar{1}\,0)_\theta$ should be missing reflections but their visibility could also be induced by double diffraction. Thus it is difficult to make conclusions regarding the three space groups based on conventional SAD patterns, due to the large unit cell in c* direction and the resultant proximity of the diffraction spots as well as high density of faults in various orientations in the hydride precipitate. For this reason a more thorough characterization of the structure of the tetragonal precipitates via conventional convergent beam analysis also has not been possible.

The differences in post-charged surface microstructures in both the low and high pressure charging experiments at the higher end of the temperature range studied (above 740°C), compared to the microstructures in the interior of the samples, are interesting since the volume fractions of the hydrides in surface regions were much higher. It appears that hydride formation is actually enhanced by the availability of oxygen. This may be due to the need for redistribution of Al in order to form the Ti-rich hydrides. From a technological point of view these surface observations are important because they suggest that any prior surface oxidation may enhance the potential embrittling effect of hydrogen for two phase materials and/or single phase alloys with low Al contents, particularly under low pressure conditions.

3.5.2 Hydrogen and Mechanical Behavior

Low temperature exposures at 500°C have clearly been shown to reduce ductility. Interestingly, an air exposure is just as detrimental as a hydrogen exposure. Although both treatments show about the same ductility reduction, it is unlikely that the same mechanism is responsible for this reduction. Tension samples which have been exposed to air exhibit a

high density of surface microcracks following testing, whereas these are not observed following vacuum or hydrogen exposures. The detrimental effect of oxygen exposures have also been noted in several other studies [22 - 24]. With regard to low levels hydrogen, it is unclear by what mechanism ductility reduction occurs. Fracture surface characteristics were not markedly different in the hydrogen-charged material, compared to the uncharged. Additionally, with materials containing a significant proportion of lamellar structure it is difficult to identify fracture origins. Given some of the above surface observations, these exposures may enhance surface crack initiation, but the experiments conducted here can not conclusively confirm this.

Although no tension experiments were conducted on high pressure hydrogen-charged material, there was clearly a strong embrittling effect of hydrogen compared to the low pressure charging; sectioning and preparation of TEM foils was extremely difficult. Considerable room temperature strengthening results from the precipitation of the hydride phases following the high pressure charging experiments. It is interesting that the yield strengths of the materials charged at 7 MPa and 13.8 MPa were similar, in spite of the fact that two different hydride phases were observed. The mechanisms responsible for strengthening in each case require further study. The presence of a significant volume fraction of misfitting, coherent FCC hydrides could result in substantial strengthening due to interactions with gliding dislocations and/or by altering the development of the substructure in regions where the hydrides are preferentially present. The tetragonal hydrogen-induced phase exists as particles which extend across the lamellae. These additional interfaces presumably break up glide in favorably oriented colonies, i. e. colonies inclined to the axis of the applied stress, thereby increasing the strength. Presumably for both charging conditions additional solid solution strengthening occurs, indicated by increased oxygen and nitrogen levels and the lattice distortion shown by the X-ray results. It has been shown that the yield strength increases with oxygen content [25] in

similar alloys, but not to the degree observed in the hydrogen-charged material. Only small differences in strain rate sensitivity between the uncharged Ti-48Al-2Cr-2Nb and the charged modifications have been observed. This indicates that the microstructural changes due to hydrogen charging influence the rate insensitive, i.e. athermal deformation processes to a greater degree than the rate sensitive processes.

4.0 Personnel Supported

In addition to Professors Pollock and Thompson, two additional researchers were supported by this program:

1. Dr. Kezhong Li, Ph.D. candidate, supported 1/93 - 1/96;
   Ph.D. granted December, 1995.
   Current Employment: Edison Welding Institute, Columbus, OH.
2. Dr. Ulrike Habel, postdoctoral researcher, supported 2/94 - 10/94;
   Current Employment: Crucible Research, Inc., Pittsburgh, PA

5.0 Publications

1. "A New Phase in Hydrogen-Charged Ti-48Al-2Cr-2Nb", K. Li, T.M. Pollock, A.W. Thompson and M. De Graef, Scripta Metall. Mater. **32**, (1995), 1009.

2. "Hydrides in High Pressure Hydrogen-Charged TiAl Alloys", K. Li, M. De Graef, T.M. Pollock, D.B. Allen and A.W. Thompson, "Hydrogen Effects in Materials", TMS, Warrendale, PA, (1996), 809.

3. "The Effect of High Pressure Hydrogen Charging on Microstructure and Mechanical Behavior of a Cast $\gamma+\alpha_2$ Titanium Aluminide", U. Habel, T.M. Pollock and A.W.

Thompson, Proc. 5th Intl. Conf. on " Hydrogen Effects in Materials ", TMS, Warrendale, PA, (1996), 787.

4. "The Effect of Hydrogen Exposure on the Mechanical Properties of Ti-48Al-2Cr-2Nb", U. Habel, T.M. Pollock and A.W. Thompson, manuscript to be submitted to Metall. Mater. Trans.

5. "Characterization of a New Hydride Phase in Gas Phase Charged Gamma Titanium Alumindes" K. Li, T.M. Pollock, M. DeGraef and A.W. Thompson, to be submitted to Acta Metall Mater.

6. "Hydrogen-Induced Microstructural Changes in Gamma Titanium Aluminide Alloys", K. Li, A.W. Thompson, T. M. Pollock and M. DeGraef, to be submitted to Metall. Mater. Trans.

7. "Surface Hydrides in High and Low Pressure Charged Ti-48Al-2Cr-2Nb", K. Li, T.M. Pollock, and A.W. Thompson, to be submitted to Metall. Mater. Trans.

6.0 Interactions/Transitions

a. Presentations at Conferences:

1. "Hydrides in High Pressure Hydrogen-Charged TiAl Alloys", K. Li, M. De Graef, T.M. Pollock, D.B. Allen and A.W. Thompson, Poster Presentation, Proc. 5th Intl. Conf. on "The Effects of Hydrogen on Material Behavior".

2. "The Effect of High Pressure Hydrogen Charging on Microstructure and Mechanical Behavior of a Cast $\gamma+\alpha_2$ Titanium Aluminide", U. Habel, T.M. Pollock and A.W.

Thompson, Oral Presentation, Proc. 5th Intl. Conf. on "The Effects of Hydrogen on Material Behavior".

3. "Hydride Phases in Ti-48Al-2Cr-2Nb and Ti-52Al Alloys", K. Li, T.M. Pollock, A.W. Thompson and M. DeGraef, TMS Annual Meeting, Las Vegas, NV, February, 1995.

b. Industrial Interactions

Results of Research having been the subject of invited presentations at General Electric Aircraft Engines (8/94) and Rockwell Science Center (8/95).

7.0 Inventions and Patent Disclosures

None

8.0 References

1. M. De Graef, *Introduction to Transmission Electron Microscopy*, unpublished notes.
2. D. Legzdina, I.M. Robertson and H.K. Birnbaum, *J. Mater. Res.* Vol.6, (1991), 1230.
3. M. Saqib, L.S. Apgar, D. Eylon and I. Weiss, *Proc. 7th Intl. Ti Conf.*, TMS Warrendale, PA, (1994).
4. D. Banerjee, A.K. Gogia and T. K. Nandy, *Metall. Trans.*, Vol. 21A, (1990), 627.
5. A.W. Thompson, X. Pierron, D.B. Allen, *Proc. 10th ICSMA*, Sendai, Japan, in press.
6. D.S. Schwartz, W.B. Yelon, R.R. Berliner, R.J. Lederich and S.M.L. Sastry, *Acta. Metall.*, Vol.39, (1991), 2799.
7. F.S. Rudman, J.J. Reilly and R.H. Wiswall, *J. Less-Common Metals*, Vol. 58,(1989), 231.
8. D.S. Shih, G.K. Scarr and G.E. Wasielewski, *Scripta Metall. Mater.* Vol. 23, (1988), 973.
9. M.R. Shanabarger, *Hydrogen Effects on Materials Behavior,* eds., N.R. Moody and A.W. Thompson, TMS, Warrendale, PA, (1990), 507.
10. M. Gao, J.B. Boodey and R.P. Wei, *Scripta Metall.*, Vol. 24, (1990), 2135.

11. D.S. Schwartz, R.J. Lederich, W.B. Yelon, Y.Y. Tang and S.M.L. Sastry, *Mater. Res. Soc. Symp. Proc.*, Vol. 288, MRS, Pittsburgh, PA, (1993), 99
12. D.E. Matejczyk and C.G. Rhodes, *Scripta Metall. Mater.*, Vol. 24, (1990), 1369.
13. W.Y. Chu and A.W. Thompson, *Scripta Metall. Mater.*, Vol. 25, (1991), 2133.
14. J. Gao, Y.B. Wang, W.Y. Chu and C.M. Hsiao, *Scripta Metall. Mater.*, Vol. 27, (1992), 1219.
15. J. B. Boodey, M. Gao and R.P. Wei, in *Environmental Effects on Advanced Materials*, eds., R.H. Jones and R.E. Ricker, TMS, Warrendale, PA, (1991), 57.
16. A. Takasaki, K. Ojima and Y.Taneda, *Scripta Metall. Mater.* 28, (1993), 1483.
17. M. Gao, J.B. Boodey, R.P. Wei and W. Wei, *Scripta Metall. Mater.* 27, (1992), 1419.
18. D.B. Allen, A.W. Thompson and M. DeGraef, in *Hydrogen Effects in Materials*, TMS, Warrendale, PA, 831, (1996).
19. A.W. Thompson and W-Y. Chu, *Microstructure-Property Relationships in Titanium Aluminides and Alloys*", Y-W. Kim and R.R. Boyer, eds., TMS, Warrendale, PA, (1990).
20. S.N. Sankaran, R.K. Herrmann, R.A. Outlaw and R.K. Clark, *Metall. Trans.*, A 25, (1994), 89.
21. *International Tables for Crystallography*, Vol. A., T.Hahn ed, Kulwer Academic Publishers, (1995).
22. W.E. Dowling, Jr. and W.T. Donlon, *Scripta. Met. Mater.*, 27, (1992), 1663.
23. T.J. Kelly, C.M. Austin, P.J. Fink, and J. Schaeffer, *Scripta. Met. Mater.* 30, (1994), 1105.
24. D.S. Lee, M.A. Stucke and D.M. Dimiduk, *Mater. Sci. Eng.* A92/193, (1995), 824.
25. C. Toennes, J. Roesler, R. Baumann and M. Thumann, *Proc. 1st International Symposium on Structural Intermetallics*, eds. R. Darolia et al (TMS, Warrendale, PA, 1993), 241.